1992

Growth of an angled crack with overshoot and/or overload

Eric Baisch
Lehigh University

GROWTH OF AN ANGLED CRACK WITH OVERSHOOT AND/OR OVERLOAD

by

Eric Baisch

A Thesis

Presented to the Graduate Committee

of Lehigh University

in Candidacy for the Degree of

Master of Science

in

Applied Mechanics

Lehigh University

1991

This thesis is accepted and approved in partial fulfillment of the requirements for the degree of Master of Science.

December 3, 1991
(date)

Professor in Charge

Chairman of Department

ACKNOWLEDGEMENTS

I would like to thank my advisor, Dr. George C. Sih for all his guidance in the course of my graduate program. Special thanks are due for his help in putting together this thesis. Thanks are also due to Mr. Ji-Wei Ho, Mr. Yi-Der Li and Mr. Chitang Li for time spent discussing aspects of this work as well as to Mrs. Barbara DeLazaro for her time spent typing this thesis.

TABLE OF CONTENTS

TABLE OF CONTENTS - (CONTINUED)

LIST OF TABLES

LIST OF FIGURES

LIST OF FIGURES - (CONTINUED)

LIST OF FIGURES - (CONTINUED)

ABSTRACT

This investigation examines the fracture patterns which result when an angled crack in PMMA is subjected to a uniform remote loading. The main objective is not to determine the trajectory of crack growth but rather to examine the size of the crack growth increments. The acquisition of such results requires a consistent approach to crack growth, with the analysis based on a failure criterion and applied repeatedly to the unfractured material in front of the crack tip. Proposed also is a methodology for estimating the overload associated with stiffness change as the crack angle is altered with the direction of loading.

Results were obtained using the strain energy density fracture criterion which states that crack initiation will take place at a site where the local minimum strain energy density reaches some critical value. Each *finite* segment of subcritical crack growth is determined by assuming that the material elements fracture at the same value, with an oversupply of energy that increases with decreasing distance to the crack tip. The additional growth corresponding to this excess of energy is referred to as "overshoot". It was found that crack growth corrected for overshoot due to a constant effective loading is greater for a crack aligned nearly along the axis of loading than for one aligned nearly perpendicular to the loading direction. Also determined was that overload could be used to explain scatter in experimental results when the angle the crack axis makes with the direction of loading becomes small. Particular attention was also given to accuracy of the finite element results as affected by changes in grid patterns and mesh sizes.

I. INTRODUCTION

It is now close to three decades since the fracture characteristics of an angle crack or elliptical notch were first examined [1]. Instead of applying the energy release rate concept, the maximum local hoop stress around the ellipse were used. This cannot be realized for a sharp crack because the local stresses become infinite at the tip. A small radial distance away from the singular point must, therefore, be observed outside of which the maximum local circumferential stress could be assumed to govern failure initiation [2]. Experimental data on pre-cracked PMMA plates were obtained as the orientation between the applied load and crack plane were varied. Although the direction of crack initiation agreed well with experiment, the local critical stress in itself is not sufficient for predicting the failure load. Additional criterion would have to be introduced. Moreover, the maximum local stress criterion were problematic in two respects:

- Under symmetrical load, the principal stresses on a local crack tip are both in tension and have the same magnitude.

- When a crack runs, the maximum local dynamic normal stress is parallel to the crack rather than normal to it. This contradicts the original assumption.

Despite these shortcomings, the local stress criterion were emphatically renumerated by a number of latter investigators [3-12].

In an attempt to provide a consistent description of crack initiation, slow growth and final termination, the strain energy density criterion was proposed in 1972 [13]. It was assumed that crack would initiate in the direction where the volume energy density acquires a relative minimum. The idea of associating the minimum of a function with failure were met with scepticism [14-16] mainly because unfamiliarity with the concept that the same function could predict the location of failure and critical load. In fact, the results in [17] showed that the brittle fracture path in PMMA specimens coincided closely with the path along which the volume energy density function were minimum. Much of the misunderstood discussions were later clarified in [18,19] although not completely [20]. In retrospect, it should be kept in mind that the stationary values of a function in two variables cannot, in general, be found simply by holding one of them constant. This would lead to false conclusions [20]. The early work in [17] clearly showed that the energy density function possessed many minima, the loci of which were assumed to coincide with the fracture path. Obviously, failure would initiate at the site of the maximum of the many minima. Alternate versions of the energy density criterion have also been proposed [21,22] and have found to contain contradictions and/or unwieldy results [23,24]. Potential pitfalls arising from energy related criteria when proposed at will can be found in [25].

The angle crack configuration was used exclusively in the stress and failure analysis of the previously mentioned works. Validity of criteria were argued on the basis of how closely the data would match

with the analytical results even when data scatter were clearly present in a number of cases. Emphasized in [19] is that the specimen stiffness tends to increase as the crack is rotated towards the direction of applied load. This would result in more overload for the stiffer specimen, a condition well known in fracture tests. Such a discrepancy in computing for the failure load has never been assessed quantitatively or explained qualitatively. Therefore, many of the arguments involving the comparison of analytical and test data are far from conclusive. Explored in this thesis is how the specimen stiffness or compliance could contribute to the amount of overload and the possible means of correcting for the scatter on crack initiation data. Modelling of the crack growth process involves additional discrepancy due to inherent discreteness of the numerical analysis. As the crack is assumed to grow in finite segments at some threshold level, the elements nearest to the crack front would be strained more than those further away because of the rapid elevation of the local stress and/or energy. When referred to a constant energy density, there would be an excess of energy above and beyond the critical value. In theory, this would overdrive the crack resulting in "overshoot". The effect can be minimized by taking smaller crack growth segments but cannot be completely removed because of the finiteness of numerical analysis. This is consistent with the experimental procedure where the load increments are also finite that would give rise to overshoot. It could be evidenced as markings on the fracture surface. Overshoot in crack growth and overload in crack initiation are two separate effects although they

could both prevail in practice. Their presence will no doubt alter the test data depending on the combined interaction of loading rate, specimen size and geometry and material type. Unless they are properly accounted for in the analysis, the correlation between theory and experiment remains unexplained.

II. FAILURE CRITERION

Classical continuum mechanics is able to provide information on the magnitude and distribution of stress, strain or strain energy in a given body, but does not address the process of material damage*. While the theory of plasticity recognizes permanent deformation caused by excessive shaped change, it is not able to account for failure by fracture. Many different failure criteria have thus been proposed with each catered to a specific situation. The choice of how the stress and failure analysis should be combined for a given problem has been the subject of many past discussions. The fracture behavior of the angle crack is further examined in this work with reference to overload and overshoot.

2.1 Continuum Limiting Length

One assumption that should be made in examining the state of affairs near a crack tip is that of a core region. Macrocrack propagation is assumed to originate from a critical site such as a crack tip. Surrounding this critical site will be a zone, say of radius r_o, inside which the behavior is associated with phenomenon which take place at a scale level below that of the remainder of the object being examined. This critical zone is known as the core region as shown in Figure 2.1. The size of r_o is comparable to that of the continuum element $\Delta x \Delta y$ in two dimensions. The lineal dimension Δx or Δy defines the resolution

*Up to this date, only the isoenergy density theory [26] is capable of providing a complete description of the material damage process that includes energy loss by heat dissipation.

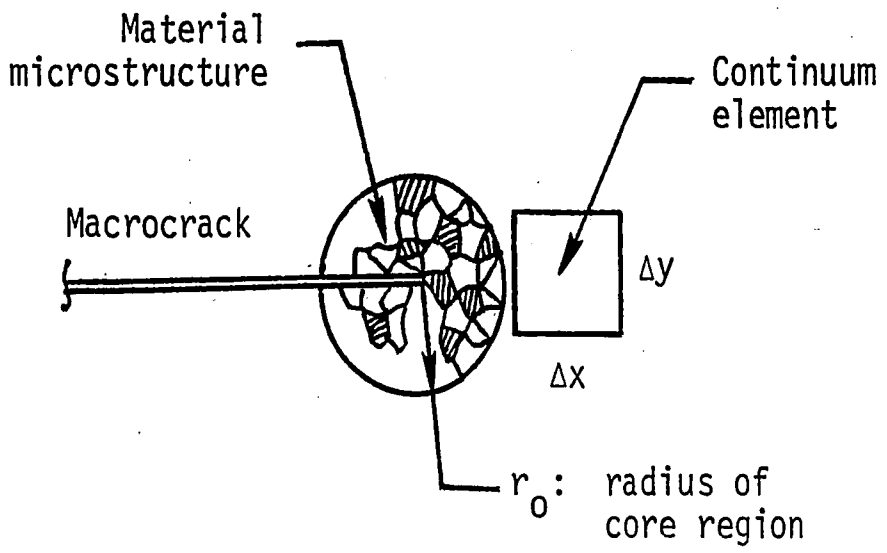

Figure 2.1. Schematic of core region.

of the continuum mechanics analysis and is by definition several orders of magnitude larger than the microscopic size. No fixed value of r_o should be assigned as a priori because it would depend on the microscopic character of the material. The grain size in polycrystals could vary by an order of magnitude. Nevertheless, it is necessary to observe a limiting length in any analysis, particularly when the classical continuum mechanics theories leave out the size effect. A case in point is the theory of elasticity that has been used for analyzing the behavior of structures several meters in dimensions and for examining events at the atomic level where the dislocations are of the order of 10^{-6} centimeters.

For the convenience of numerical calculation, r_o has been taken as 10^{-2} times the half crack length, a, for a finite through crack configuration. It would then be well inside the region where the asymptotic solution having the $1/\sqrt{r}$ singular character coincides with the exact

solution at r/a = 10^{-1} location as illustrated in Figure 2.2. It so

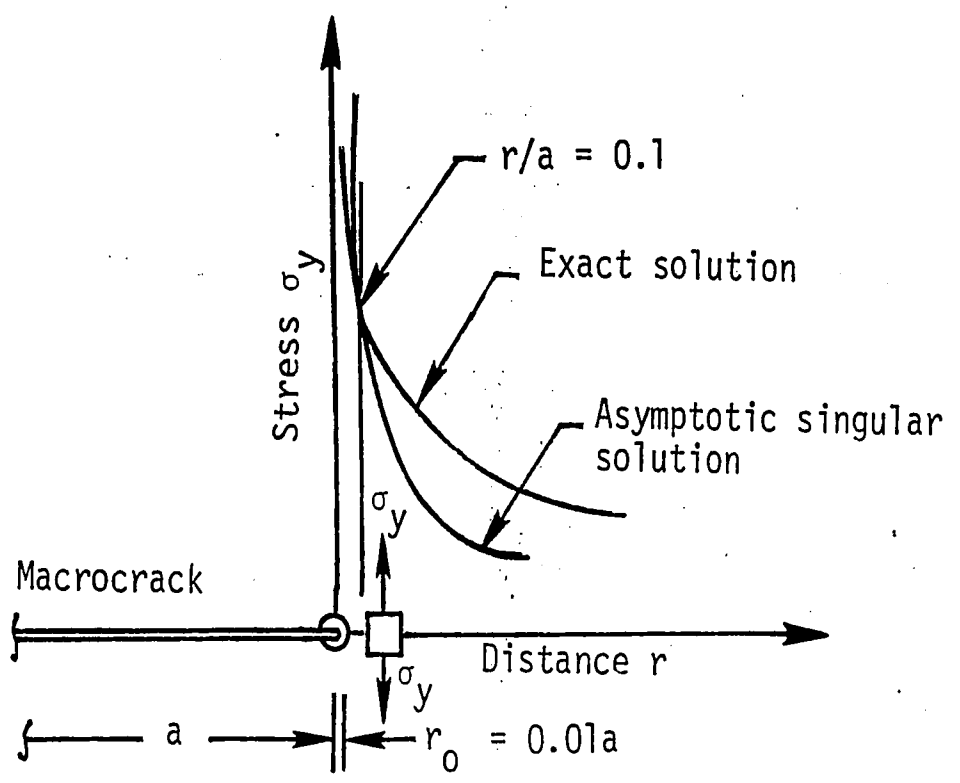

Figure 2.2. Near field stress decay for a finite crack: comparison of exact and asymptotic solution.

happens that the $1/\sqrt{r}$ singular character could be enforced along a line ahead of the crack in the finite element analysis when using the twelve (12)-node isoparametric element. This is accomplished by a shift of the side nodes [28,29] x_2 to 1/9 and x_3 to 4/9 as shown in Figure 2.3.

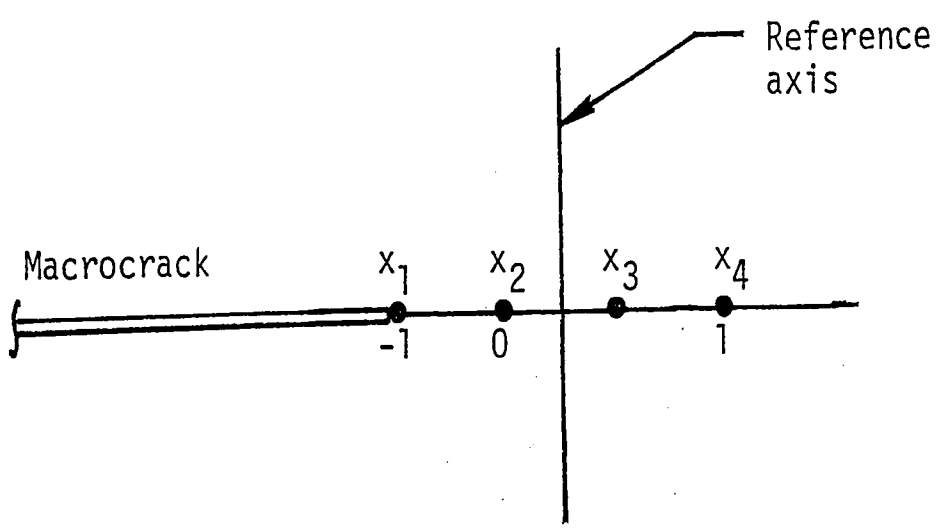

Figure 2.3. Crack tip with reference to the side of a twelve (12)-node isoparametric element.

In this way, r_o serves the dual purpose of a continuum limiting distance and expediency in numerical calculation.

2.2 Strain Energy Density Criterion

The strain energy density fracture criterion of Sih [27] predicts fracture based on the energy density distribution in the object being examined. A strength of this fracture theory is its ability to predict both the direction and extent of crack growth. The strain energy density is commonly written as dW/dV and can be determined in terms of the stresses σ_{ij} and strains ε_{ij} as

$$\frac{dW}{dV} = \frac{1}{2}\,\sigma_{ij}\varepsilon_{ij} \tag{2.1}$$

for a linear elastic material. Under the condition of plane strain with i,j = x,y,z where

$$\varepsilon_z = 0,\ \sigma_{xz} = \sigma_{yz} = 0 \tag{2.2}$$

and

$$\sigma_z = \nu(\sigma_x+\sigma_y) \tag{2.3}$$

equation (2.1) may be written as

$$\frac{dW}{dV} = \frac{1+\nu}{2E}\left[(1-\nu)(\sigma_x^2+\sigma_y^2) - 2\nu\sigma_x\sigma_y + 2\sigma_{xy}^2\right] \tag{2.4}$$

The Poisson's ratio is ν and Young's modulus is E.

It is well known that the material around a crack tip undergoes shape and volume change. The former takes place in a direction away from the crack plane while the latter occurs along the path of prospective crack extension. These effects can be quantified in terms of the proportion of the distortional (shape change) and dilatational (volume change) strain energy density, namely $(dW/dV)_d$ and $(dW/dV)_v$ in linear elasticity. That is, equation (2.1) or (2.4) may be regarded as the linear sum of $(dW/dV)_d$ and $(dW/dV)_v$:

$$\frac{dW}{dV} = \left(\frac{dW}{dV}\right)_d + \left(\frac{dW}{dV}\right)_v \tag{2.5}$$

Depending on the state of stress and strain and location in the body, both situations

$$\left(\frac{dW}{dV}\right)_d > \left(\frac{dW}{dV}\right)_v \quad \text{or} \quad \left(\frac{dW}{dV}\right)_v > \left(\frac{dW}{dV}\right)_d \tag{2.6}$$

could prevail. The first condition in equations (2.6) corresponds to distortion being the controlling factor and the likelihood of yield initiation while the second condition corresponds to dilatation being dominant that could lead to fracture initiation. In regions where dilatation is greatest, dW/dV will be a relative minimum. The strain energy density criterion proposes that the direction of crack growth will correspond with $(dW/dV)_{min}$. In general, there might be many minima in the body. The strain energy density criterion proposes that failure

initiation will take place at the site of $(dW/dV)^{max}_{min}$. The critical strain energy density, $(dW/dV)_c$, is material specific and corresponds to the area under the true stress strain curve. As the state of stress in the body is increased, it is $(dW/dV)^{max}_{min}$ that will first reach the critical parameter $(dW/dV)_c$. Figure 2.4 shows a sample local strain

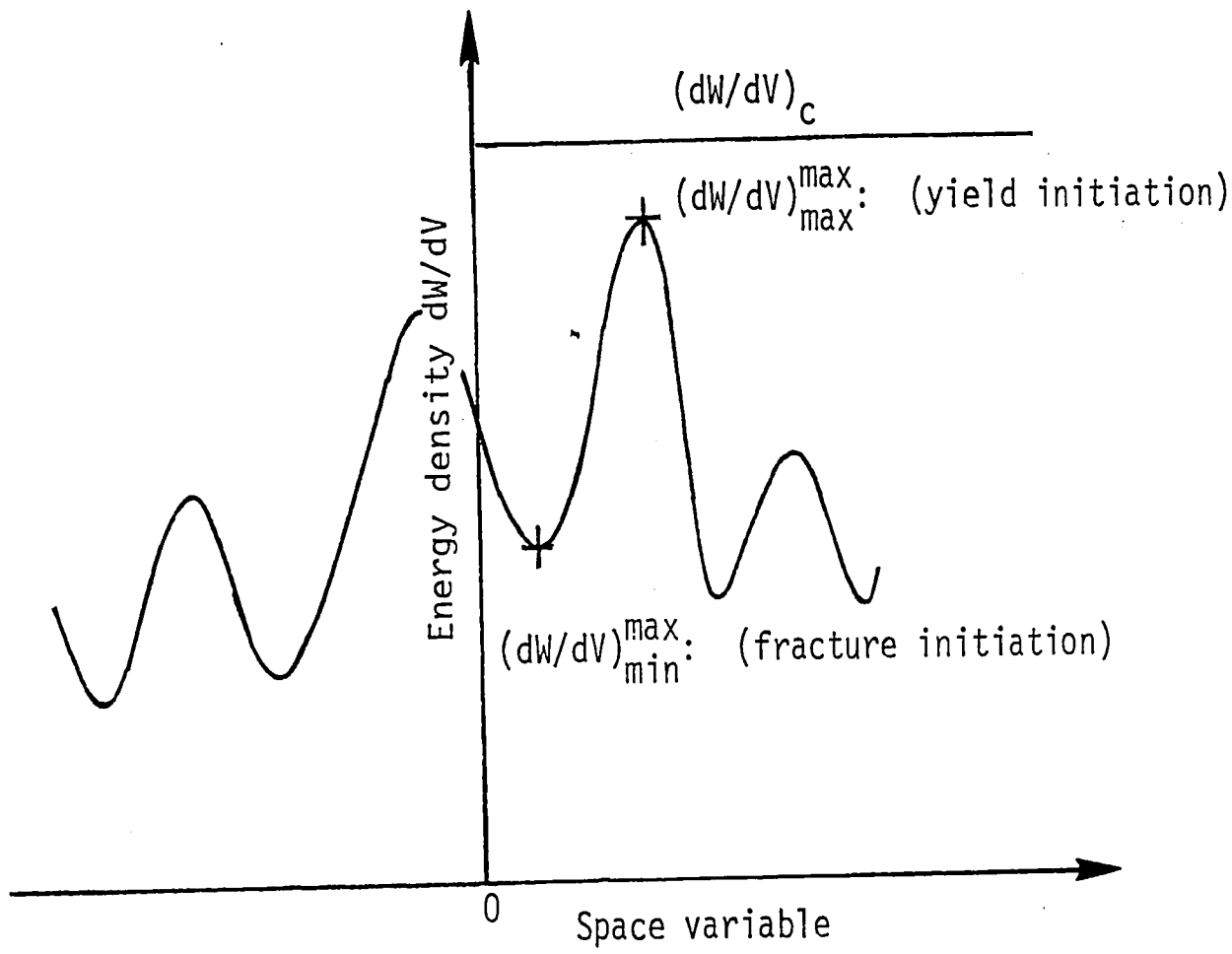

Figure 2.4. Variation of energy density with space variable.

energy distribution with the local $(dW/dV)^{max}_{max}$ and $(dW/dV)^{max}_{min}$ indicated. It becomes obvious that it is the maximum minimum which will reach the critical strain energy density first when the site of potential failure is subjected to a rising energy distribution. The yield initiation is assumed to occur when $(dW/dV)^{max}_{max}$ reaches $(dW/dV)_y$ which is the area under the true stress and strain curve up to the yield point. Since

$(dW/dV)_y < (dW/dV)_c$, yield initiation always precedes fracture initiation.

2.3 Local and Global Stationary Values

One distinct feature of the strain energy density criterion [27] is that the stationary values of dW/dV automatically determines the proportion of distortional and dilatational effects or the conditions in equations (2.6) which apply only for the elastic material. The discussion with reference to Figure 2.4 applies to any nonlinear dissipative material where equations (2.5) and (2.6) are no longer valid.

General Consideration. For a two-dimensional body, dW/dV would depend on two space variables (X,Y). In a plot of dW/dV versus X and Y, there would be peaks and valleys as indicated in Figure 2.5. The val-

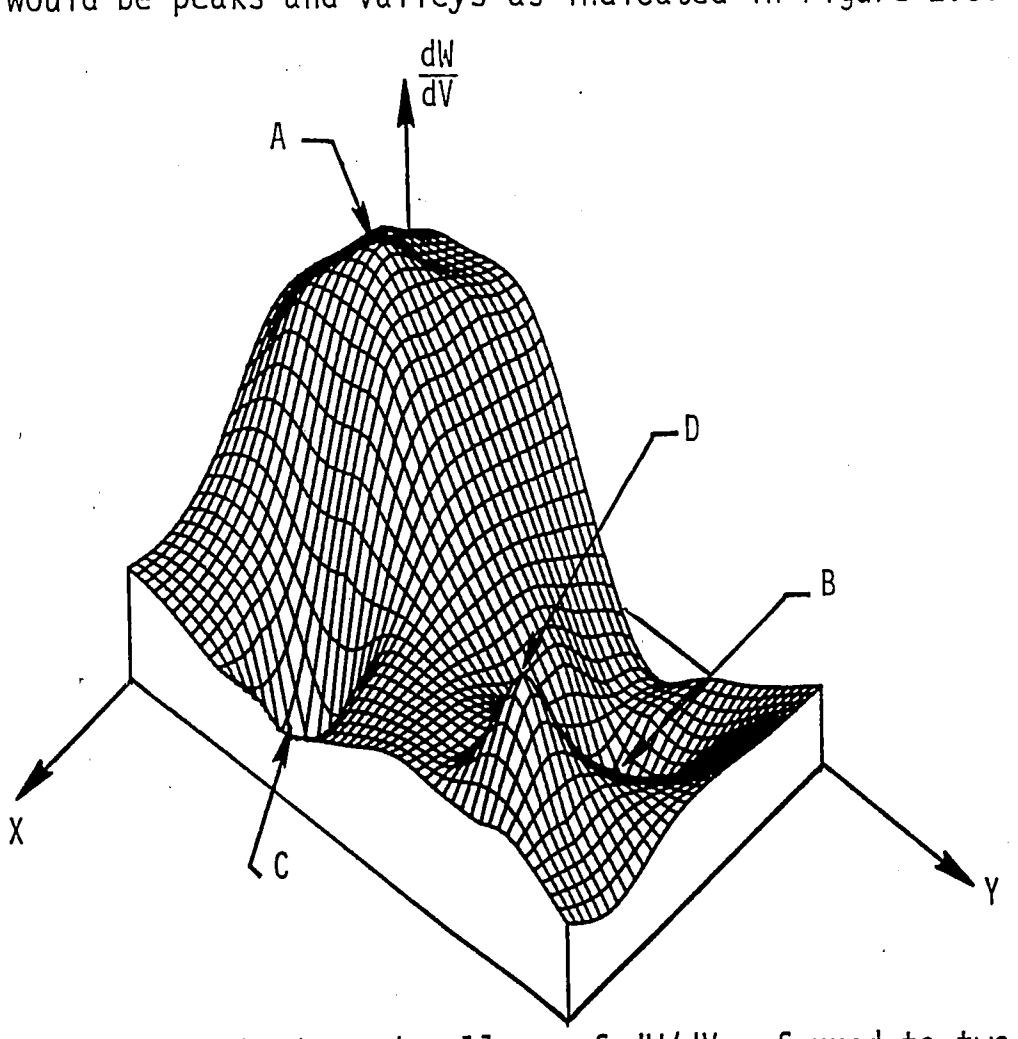

Figure 2.5. Peaks and valleys of dW/dV referred to two space variables.

ues of $(dW/dV)^{max}_{max}$ and $(dW/dV)^{max}_{min}$ can thus be located by inspection. More specifically, Figure 2.6 gives a typical computer plot of constant

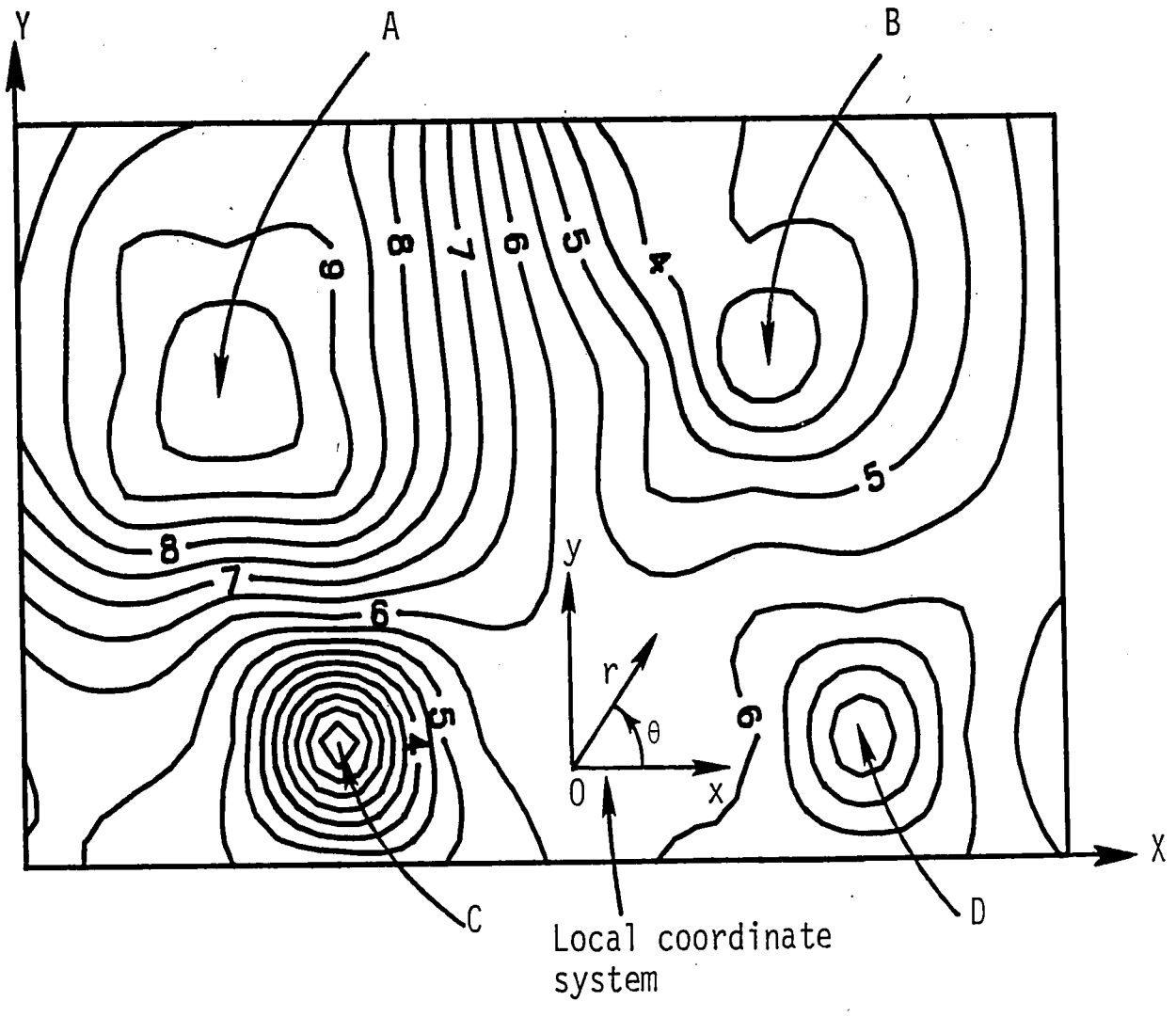

Figure 2.6. Contour of constant dW/dV referred to two space variables.

dW/dV contours where two maxima are located at A and D and two minima at B and C. Since $(dW/dV)_{max}$ at A is greater than that at D and $(dW/dV)_{min}$ at B is greater than that at C, the pair $(dW/dV)^{max}_{max}$ and $(dW/dV)^{max}_{min}$ would be unique in any given problem. They are known as the *global* stationary values distinguished by the subscript G because they refer to the same fixed coordinate system (OXY) as given in Figure 2.6. The designation is $[(dW/dV)^{max}_{max}]_G$ and $[(dW/dV)^{max}_{min}]_G$.

Suppose that dW/dV is now referred to a system of local coordinates (x,y) or (r,θ) as shown in the midst of the contours in Figure 2.6. It is guaranteed that for each location of (oxy) there would prevail a pair of $(dW/dV)_{max}$ and $(dW/dV)_{min}$. They are the local stationary values denoted by the subscript L, i.e., $[(dW/dV)_{max}]_L$ and $[(dW/dV)_{min}]_L$. Among the many local maxima and minima, there exists a pair that would have the largest values written as $[(dW/dV)^{max}_{max}]_L$ and $[(dW/dV)^{max}_{min}]_L$. The distance between $[(dW/dV)^{max}_{min}]_L$ and $[(dW/dV)^{max}_{min}]_G$, say ℓ, is indicative of failure instability by fracture [30,31] and between $[(dW/dV)^{max}_{max}]_L$ and $[(dW/dV)^{max}_{max}]_G$ by plastic collapse [32]. This idea could be best illustrated by the failure behavior of a crack.

Fracture Instability. Consider the problem of a through crack of length 2a in a plate subjected to uniform stress σ_0 as shown in Figures 2.7(a) and 2.7(b). The dimensions of the plate in both cases are the same. Only the crack length is different. It was found in [33] that ℓ extended to the plate edge when the crack is small. This implies that once crack initiates, the entire ligament from L to G breaks, Figure 2.7(a). If the initial crack is sufficiently long, less energy is stored in the uncracked ligament and G no longer extends to the plate edge. A smaller value of ℓ corresponds to a more stable fracture as the energy concentration is more localized. The relative size of ℓ provides information on crack growth stability.

2.4 Subcritical Crack Growth

Crack growth initiation is assumed to occur when dW/dV in the near-

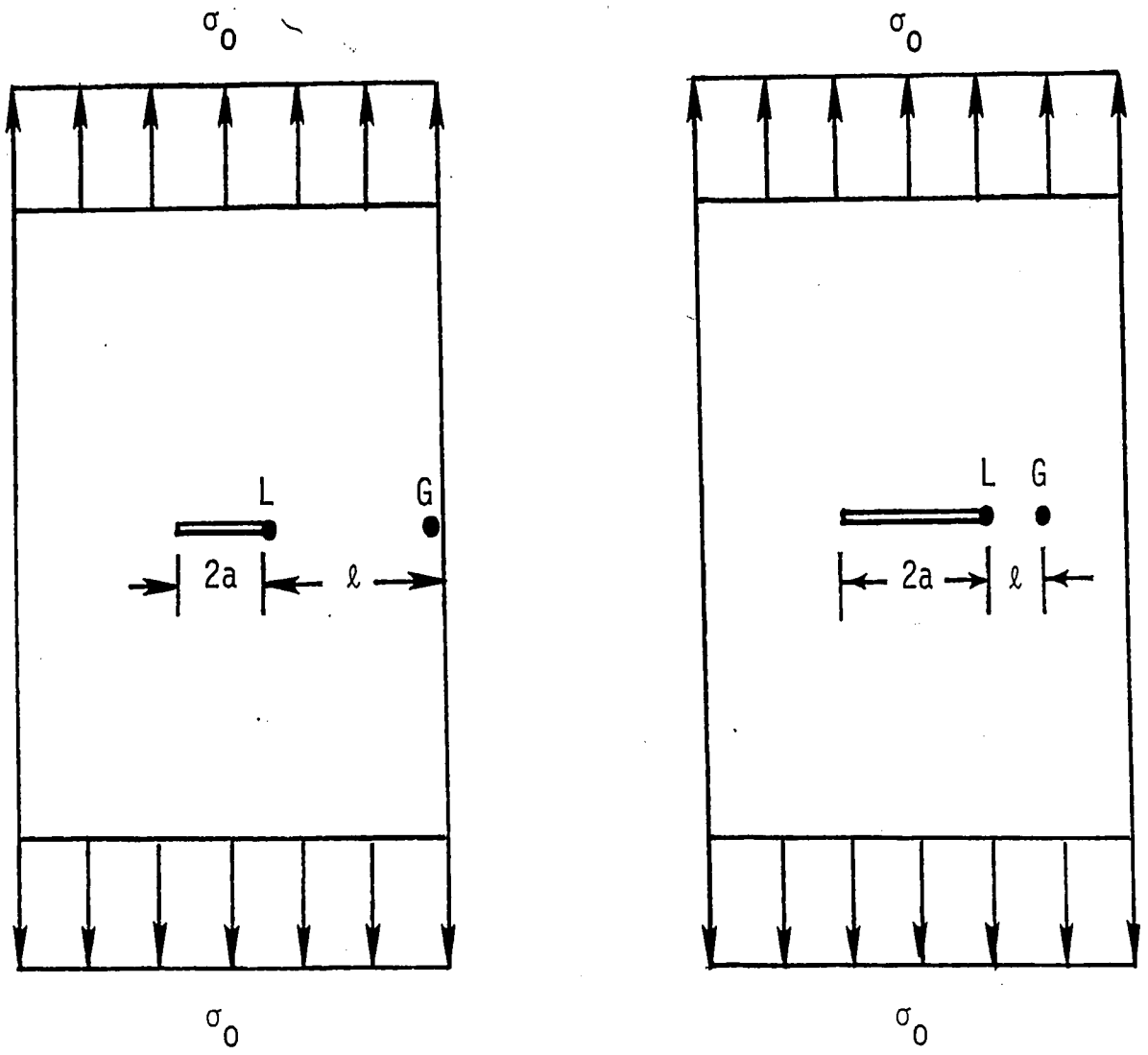

(a) Small crack (b) Large crack

Figure 2.7. Fracture instability as affected by initial crack length.

est element to the crack tip reaches some critical value $(dW/dV)_c$ as mentioned earlier with reference to the strain energy density criterion [27]. The segment of crack growth, say r_1, r_2, etc., can be estimated by assuming that

$$\left(\frac{dW}{dV}\right)_c = \frac{S_1}{r_1} = \frac{S_2}{r_2} = \ldots = \frac{S_j}{r_j} = \ldots = \frac{S_c}{r_c} \qquad (2.7)$$

The last ligament of material r_c that triggers the onset of rapid fracture can be computed if S_c is known for a given material because

$$\left(\frac{dW}{dV}\right)_c = \int_0^{\varepsilon_c} \sigma d\varepsilon \tag{2.8}$$

with ε_c being the final critical strain. In equation (2.7), S_c is related to the ASTM valid K_{1c} fracture toughness value as

$$S_c = \frac{(1+\nu)(1-2\nu)K_{1c}^2}{2\pi E} \tag{2.9}$$

Refer to [34] for more details.

III. CONCEPT OF OVERLOAD AND OVERSHOOT

The failure envelop in engineering practice is an idealized concept that serves as a reference for monitoring the deviations of experimental data. Failure by fracture is a gradual process that involves the nucleation of microscopic damage and eventual material separation, an event that is visible to the naked eye and hence referred to as macroscopic fracture. Illustrated schematically in Figure 3.1 is a typical

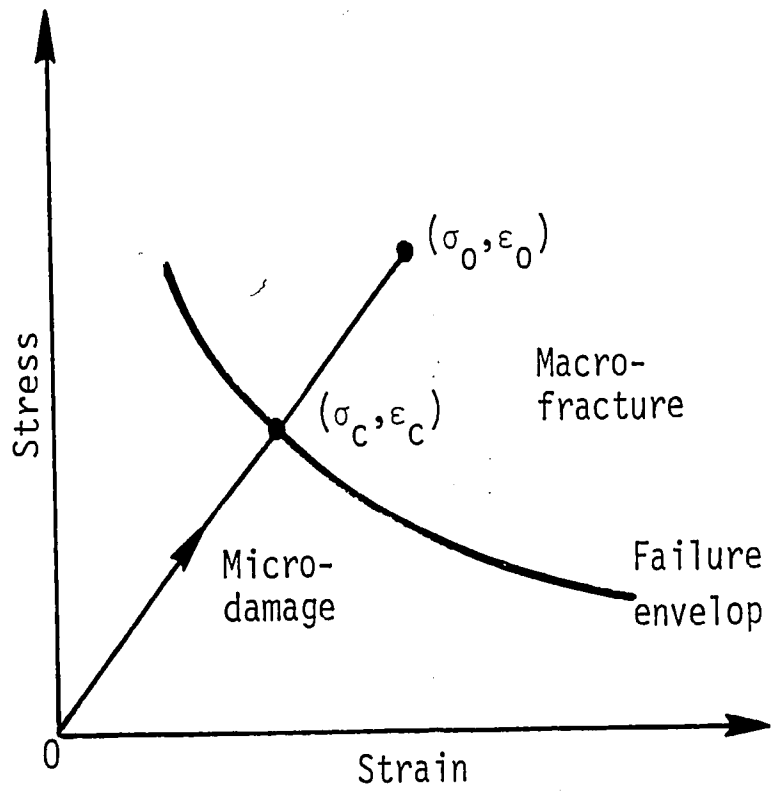

Figure 3.1. Failure envelop in a plot of stress versus strain.

description of the stress and strain states in a structural component. The failure envelop assumes that the change in material damage from the microscopic to the macroscopic scale level is a sudden process. The metastable states (σ_c,ε_c) is representative of the commitment made on the failure criterion. Fracture data (σ_0,ε_0) must necessarily fall outside the envelop (σ_c,ε_c). The deviations would depend on the com-

bined interaction of loading, specimen geometry and material type; they are often referred to simply as scatter without explanations.

3.1 Single Macrocrack Model

The single crack configuration has been used frequently as the best test model to examine the fracture behavior of metals. Regardless of the scale level at which material damage would be quantified, it is necessary to understand the physics underlying the material damage process. In the average polycrystalline specimen, crack growth is *discontinuous*, meaning that fracture is not just the movement of a single crack front. Individual grains do not fracture at the same time as their strength, shape and size vary by wide margins. The cracked grains, however, may join in segments to form an irregular surface along a path of greatest load transmission. These factors would affect the difference between (σ_0,ε_0) and (σ_c,ε_c) as shown in Figure 3.1. Their influence in a continuum mechanics analysis for the single crack model can be summarized as follows:

- *Loading*. The hierarchy of the material damage process is dictated by the time history of the energy transfer process. For the same material and specimen, failure would initiate at the specimen center for slowly rising load in contrast to failure starting from the specimen surface in fatigue.

- *Size and Geometry*. Specimen size and geometry could be altered to change brittle fracture to ductile fracture even if the load and material are the same.

Material Type. Microstructure of the material would affect the crack initiation and growth characteristics. Incubation time of the crack tip in the core region (Figure 2.1) depends on the inhomogeneity of the grains.

It would, therefore, be useful to observe how loading rate, specimen size and material microstructure would affect the deviations between (σ_o,ε_o) and (σ_c,ε_c). A ranking system such as that outlined in Table 3.1 may be used. Large and small deviations may be shown to correspond to the combinations of $L_1\Lambda_1M_1$ and $L_3\Lambda_3M_3$, respectively.

Table 3.1. Ranking order for loading, specimen size and material type.

Loading Rate	Specimen Size	Microstructure Inhomogeneity
L_1: High	Λ_1: Large	M_1: High
L_2: Medium	Λ_2: Medium	M_2: Medium
L_3: Slow	Λ_3: Small	M_3: Low

3.2 Overload of Cracked Specimen

To be more specific, the concept of an "overload" or the difference between σ_o and σ_c in Figure 3.1 can be illustrated by referring to the configuration of a center cracked body in Figure 3.2. The applied uniform stress σ is increased slowly until the crack would reach the critical condition at σ_c. Fracture occurs only when $\sigma \to \sigma_o$ being always larger than σ_c. According to the earlier works in [35], the total energy W in a cracked body can be regarded as the sum of that for the un-

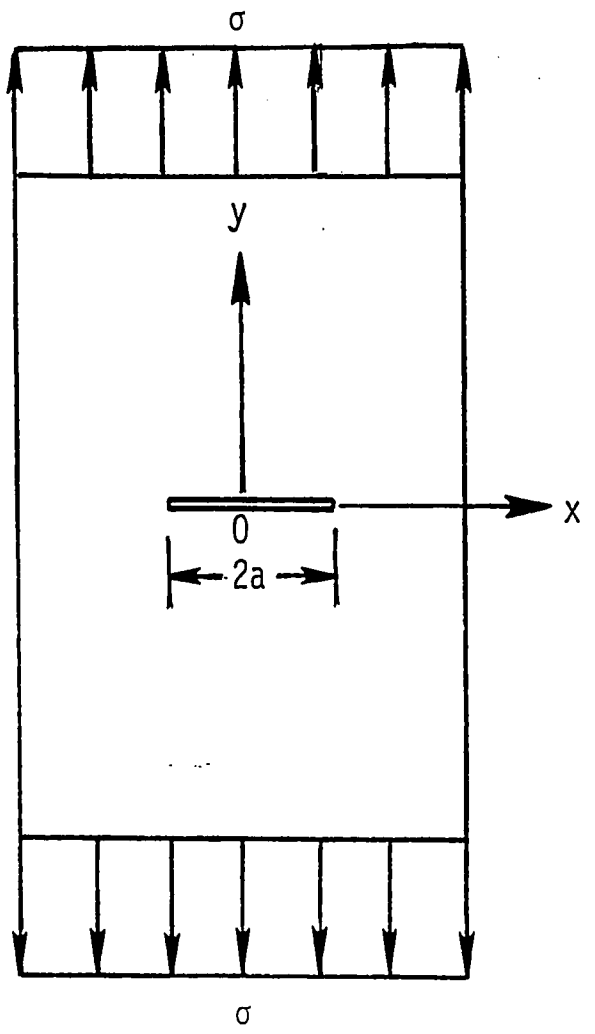

Figure 3.2. Center cracked body under uniform stress.

cracked body and that due to the presence of the crack. For the case of plane strain, W takes the form

$$W = \frac{1}{2}\frac{(1-\nu^2)}{E}\sigma^2 A + \frac{\pi(1-\nu^2)}{E}\sigma^2 a^2$$

$$= \frac{1}{2}\sigma\left[\frac{1-\nu^2}{E}\sigma + \frac{2\pi(1-\nu^2)\sigma a^2}{AE}\right]A \qquad (3.1)$$

where A is the area of the body having a unit dimension in the z-direction. An equivalent uniaxial strain ε can thus be extracted from equation (3.1) as

$$\varepsilon = \frac{1-\nu^2}{E}\left(1 + \frac{2\pi a^2}{A}\right)\sigma \tag{3.2}$$

The quantity E^* or

$$E^* = \frac{E}{(1-\nu^2)\left(1 + \frac{2\pi a^2}{A}\right)} \tag{3.3}$$

might be viewed as an equivalent elastic modulus of the cracked body such that E^* would decrease with increasing crack length.

Application of the strain energy density criterion described in Section 2.2, the critical strain energy density factor S_c in equation (2.7) can be applied. It may be regarded as the crack driving force, Figure 3.3. The critical distance r_c is the material ligament that

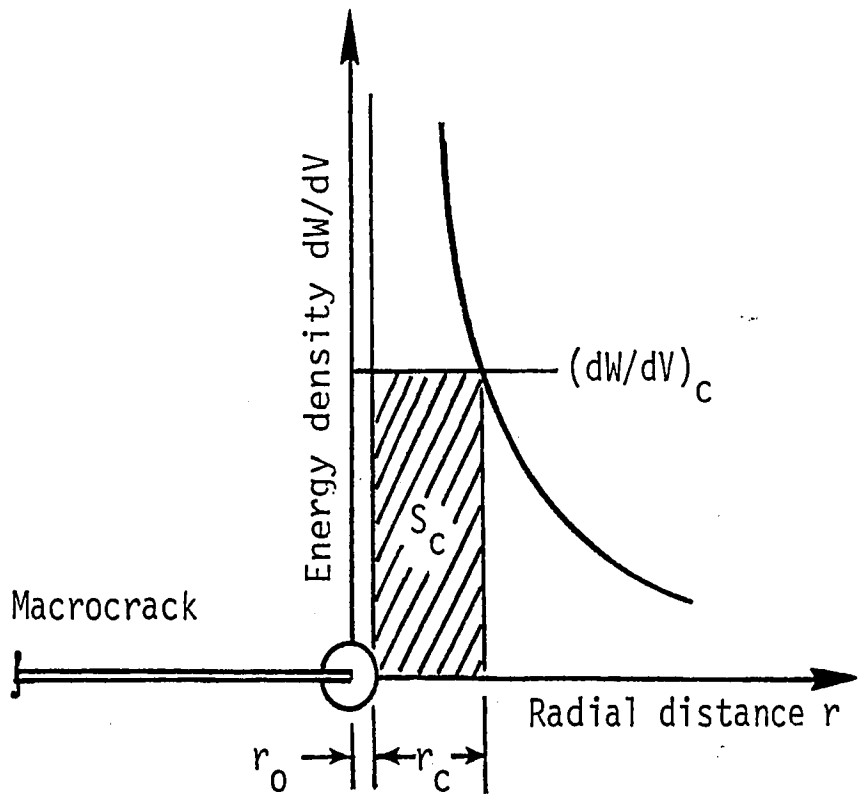

Figure 3.3. Critical strain energy density factor.

triggers the onset of rapid fracture. Knowing that $K_{1c} = \sigma_c\sqrt{\pi a}$, equation (2.9) gives

$$S_c = \frac{(1+\nu)(1-2\nu)\sigma_c^2 a}{2E} \tag{3.4}$$

The quantity a^2 in equation (3.2) can be eliminated at the critical state as $(\sigma,\varepsilon) \to (\sigma_c,\varepsilon_c)$:

$$\varepsilon_c = \frac{1-\nu^2}{E}\sigma_c + \frac{8\pi(1-\nu)ES_c^2}{(1+\nu)(1-2\nu)^2 A\sigma_c^3} \tag{3.5}$$

Equation (3.5) gives the failure envelop for the problem of a cracked body under uniform stress. A plot of σ_c versus ε_c can be found in Figure 3.4. The point c that determines when the slope of the failure envelop changes sign can be determined from the condition

$$\frac{d\varepsilon_c}{d\sigma_c} = 0 \tag{3.6}$$

Equation (3.5) can be put into equation (3.6) to yield

$$\sigma_c^4 = \frac{24\pi E^2 S_c^2 a^2}{(1+\nu)^2(1-2\nu)^2 A} \tag{3.7}$$

Making use of equation (3.4), it can be deduced that

$$m = \frac{A}{\pi a^2} = 6 \tag{3.8}$$

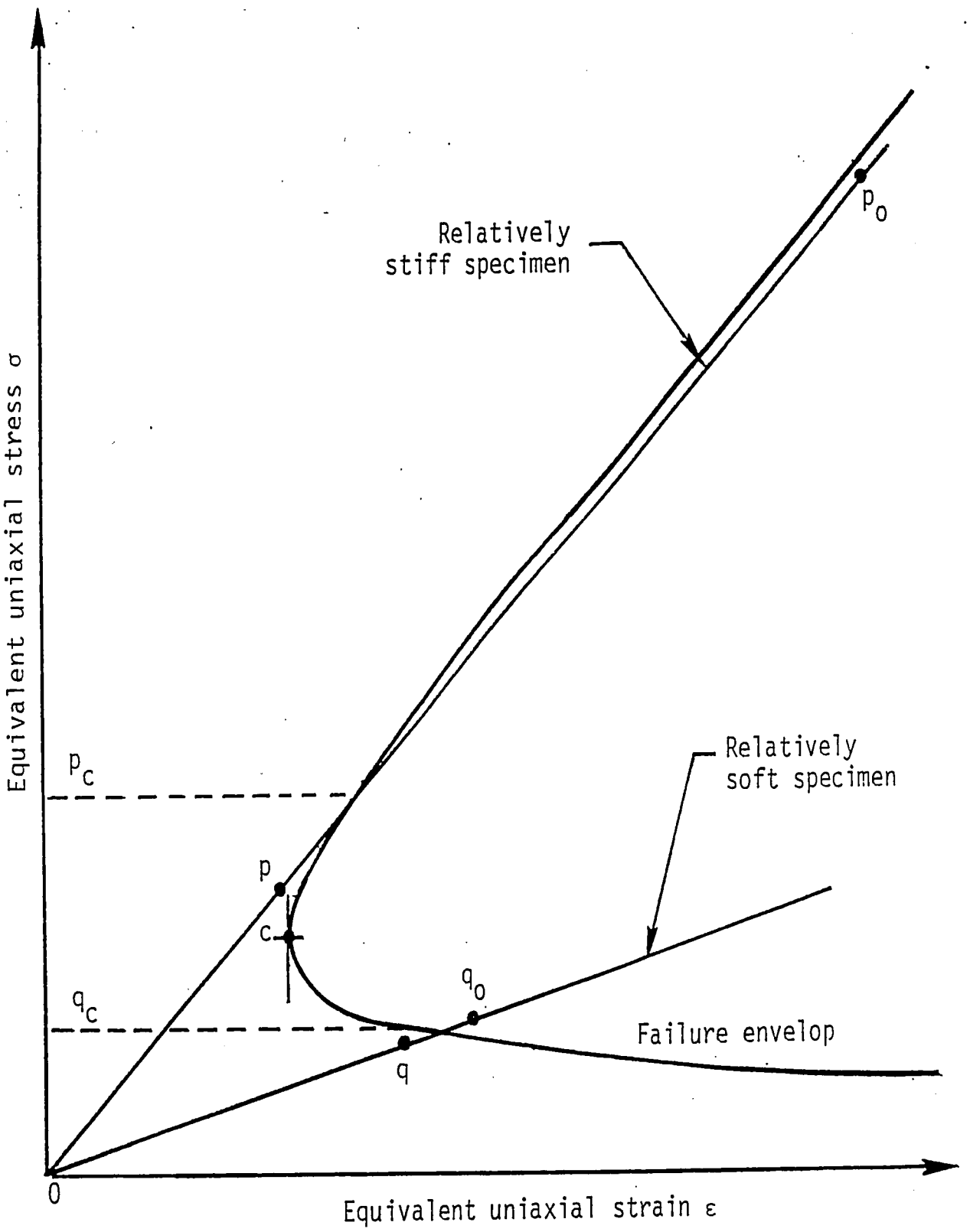

Figure 3.4. Failure envelop for a cracked body under uniform applied stress.

determines the point c. Hence, $m > 6$ and $m < 6$ would correspond, respectively, to the portions of the failure envelop with positive and negative slope. Equation (3.8) can be further inserted into equation (3.3) to obtain

$$E^* = \frac{mE}{(1-\nu^2)(2+m)} \tag{3.9}$$

This gives $E^* = (27/32)E$ for $\nu = 1/3$ and $m = 6$ at c.

For $m < 6$ where

$$E^* < \frac{3}{4}\frac{E}{1-\nu^2} \tag{3.10}$$

the specimen is relatively *soft* and the line qq_o with slope E^* in equation (3.10) would cross the failure envelop with negative $d\sigma/d\varepsilon$. The locations of q and q_o can be clearly distinguished from the points (σ_c,ε_c) on the failure envelop thus making the distance between q and q_o relatively small. When $m > 6$ with

$$E^* > \frac{3}{4}\frac{E}{1-\nu^2} \tag{3.11}$$

the specimen is relatively *stiff* and the line pp_o now crosses the failure envelop with positive $d\sigma/d\varepsilon$. Even though p and p_o are in the neighborhood of (σ_c,ε_c), they are now separated by a wide margin.

The difference of the stress levels between p_o and p_c or q_o and q_c is known as the "overload" where p_c and q_c are located on the failure envelop. It can thus be summarized that

More overload would likely be associated with a relatively stiff specimen than a relatively soft specimen.

Additional discussion on this will be given later on for the angled crack problem.

3.3 Overshoot Associated with Crack Growth

Aside from overload, there is discrepancy between theory and experiment could arise from the discrete nature of the numerical modelling process as assumed in equation (2.7). Because of the inability to address instantaneous and continuous crack growth in the finite element analysis, it is necessary to consider finite segments of crack extension r_1, r_2, etc., at some preassigned critical energy level. The elements closer to the crack front would therefore experience a high level of energy above and beyond that at incipient crack initiation. This is illustrated in Figure 3.5 for the jth segment of subcritical crack growth. The predicted segment of growth r_j from equation (2.7) is determined from the intersection of the dW/dV curve and the line $(dW/dV)_c$ at c. The elements along the segment $r_o < r < (r_o+r_j)$ are stressed beyond the critical level. An excess amount of energy proportional to the shaded area Σ_j^o would be available to overdrive the crack. The two shaded areas Σ_j^o and S_j^o could be equated to yield the so-called over-

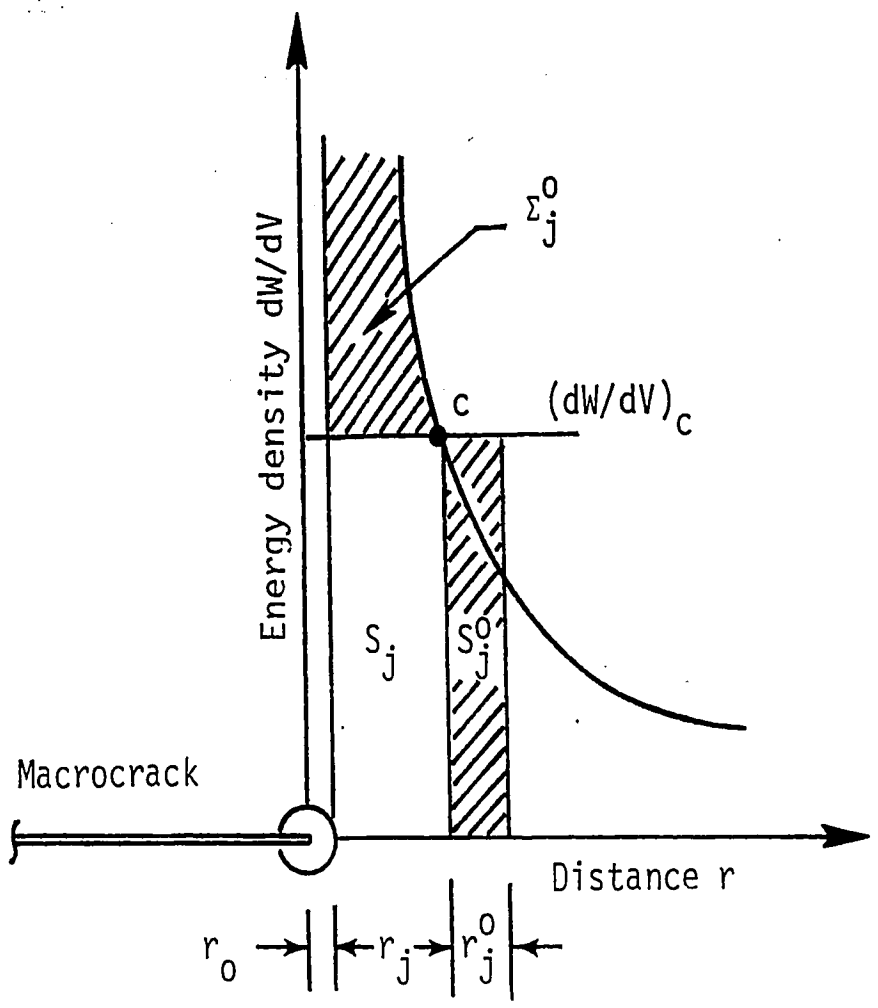

Figure 3.5. Correction on crack growth due to overshoot.

shoot r_j^o such that the total advancement of the crack would be

$$r_j^* = r_o + r_j + r_j^o, \quad j = 1,2, \text{ etc.} \tag{3.12}$$

with the corrected crack driving force as

$$S_j^* = S_j + S_j^o, \quad j = 1,2, \text{ etc.} \tag{3.13}$$

Equation (2.7) can thus be modified into the form

$$\left(\frac{dW}{dV}\right)_c = \frac{S_1^*}{r_1^*} = \frac{S_2^*}{r_2^*} = \ldots = \frac{S_j^*}{r_j^*} = \ldots = \frac{S_c^*}{r_c^*} \tag{3.14}$$

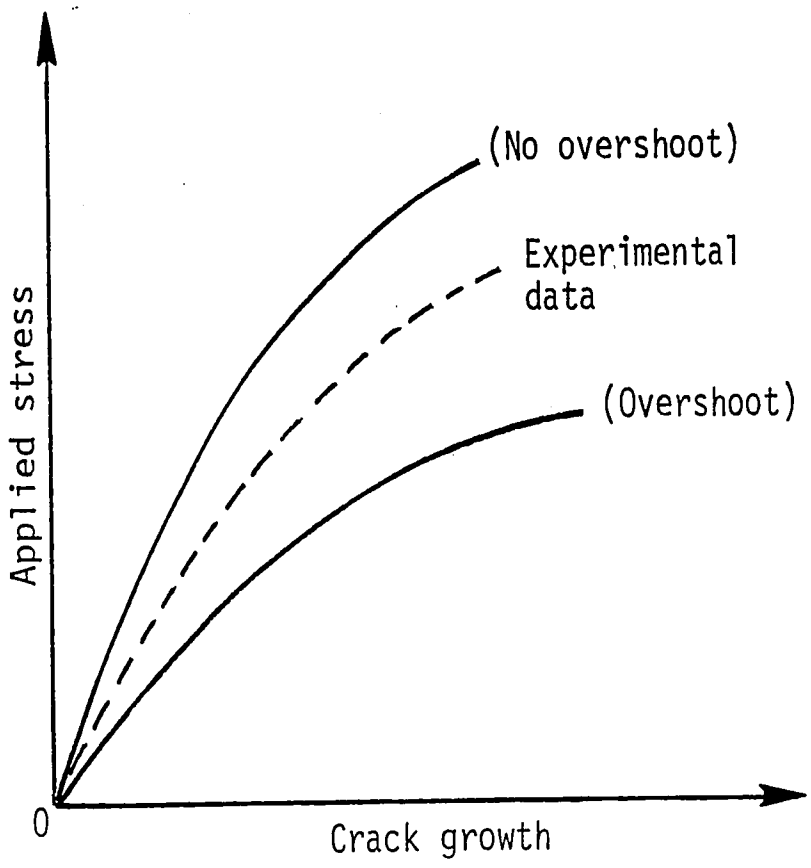

Figure 3.6. Influence of overshoot on applied load to crack growth relation.

On physical grounds, of course, not all of the excess energy Σ_j^o would contribute to overshoot. There would be some loss by inelastic deformation and acoustics. The two idealized situations stated in equation (2.7) without overshoot and equation (3.14) with overshoot would serve as an upper and lower bound solution for the relation between load and crack growth as shown in Figure 3.6. The experimental data should fall in between.

IV. DESCRIPTION OF CRACK MODEL AND COMPUTATIONAL SCHEME

In order to provide an estimate of the applied load as a function of crack growth with overshoot, the angled crack configuration will be examined for different initial crack angles with respect to the load. Displacements, strains, stresses and energy densities are obtained by application of the finite element method described in the Appendix, Section VII. For the situation of self-similar crack growth where the failure path is known before finite element meshes are generated, element boundaries can be placed along the crack growth direction preserving the $1/\sqrt{r}$ crack tip singularity. When the crack plane and load direction are not collinear, there is no a priori knowledge of the growth direction, which may not necessarily coincide with the element boundary.

Some improvement could be made by increasing the number of elements at the crack tip and thus increasing the probability of crack growth along or close to an element boundary, but for the cases being analyzed in this work, the added time required would not justify the added accuracy; as in most cases, crack growth is indeed nearly along the element boundary.

4.1 Specimen and Material

Depicted in Figure 4.1 is the configuration of an angled crack of length $2a = 5.08$ cm that is tilted away from the y-axis by the angle β. Unity is assumed for the plate thickness while β varies from 15° to 75°

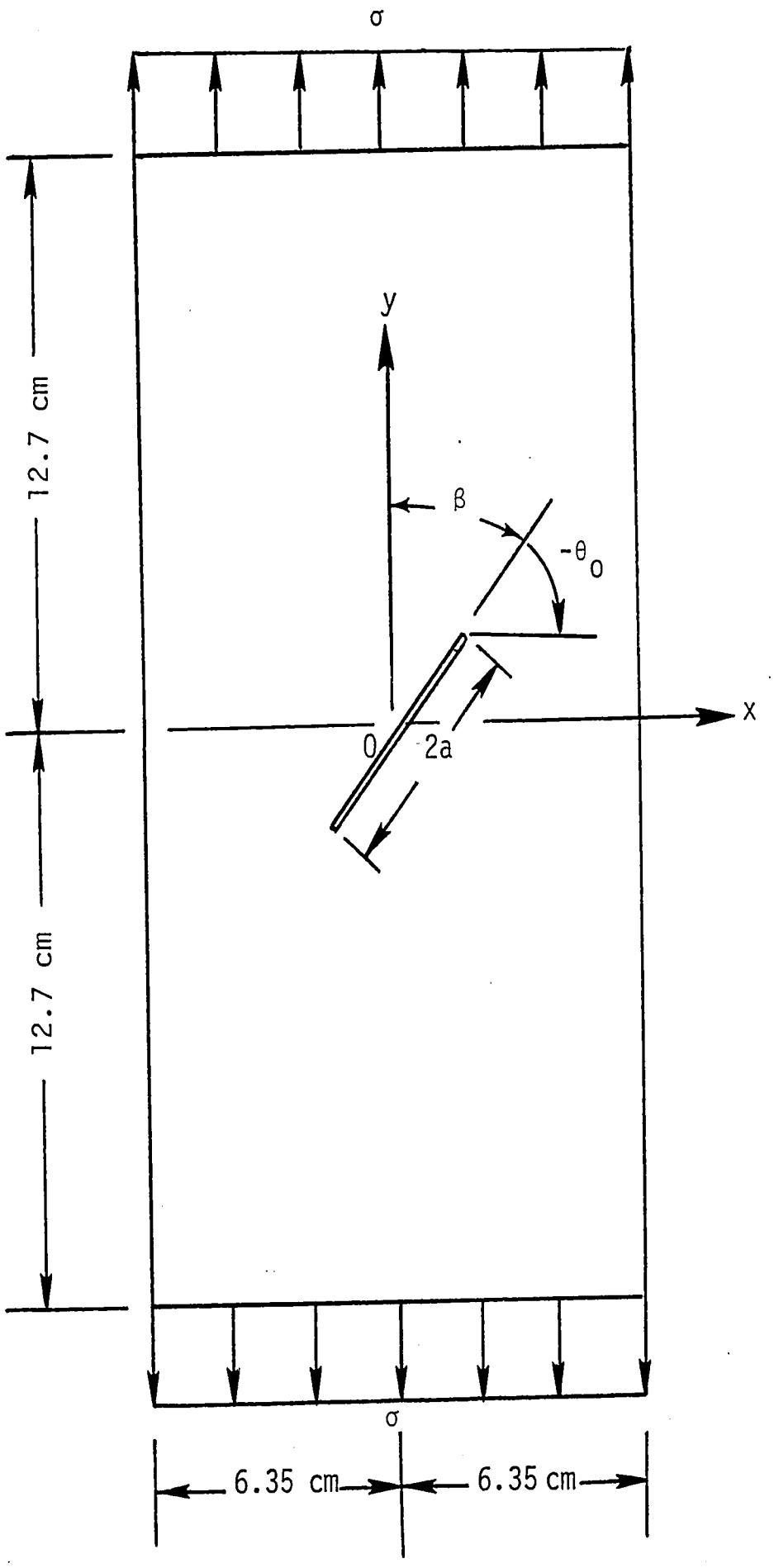

Figure 4.1. Schematic of an angled crack under uniform stress.

in increments of 15°. A distributed load is applied to the plate for all cases. The magnitude of the loading was chosen so that over the entire range of crack angles the resulting lengths of crack growth segments were such that the number of remeshings to cause failure for small β was not excessive, yet there were enough growth segments for large β to examine trends of the growth prior to global instability. The value of the remote stress determined by trial and error was 35 MPa.

The material properties of the plate were taken to be those of PMMA as experimental results are available [36]. Mechanical and fracture properties are given in Table 4.1. The value of $(dW/dV)_c$ is obtained

Table 4.1. Mechanical and fracture properties of PMMA [36].

Young's Modulus $E \times 10^8$ (Pa)	Poisson's Ratio ν	Fracture Toughness K_{Ic} MPa$\sqrt{m}$	Critical Energy Density $(dW/dV)_c$ (MPa)
23.63	0.333	0.7 to 1.6	2.084

from the area under the true stress and true strain curve in [36]. Crack growth will be assumed to occur when the strain energy density in the material exceeds this critical value in the direction corresponding to $(dW/dV)_{min}^{max}$ as described in Section 2.2 on the strain energy density criterion.

4.2 Finite Element Discretization

Modelling of crack growth is a process of repeatedly forming a fi-

nite element mesh which corresponds to the current geometry of the specimen, executing the finite element code to generate strain energy density values, and finally analyzing the strain energy density distribution based on the fracture criterion. These steps should be performed with consistency to achieve accurate results. The methodology of crack growth modelling used was determined by becoming familiar with the accepted behavior of crack growth of some known geometries, and then experimenting with many different modelling procedures in order to eliminate those yielding inconsistent results, ultimately coming up with the procedure applied here.

As explained in Section VII on the finite element method, special care must be made in constructing the finite element meshes with which any given crack configuration is modelled. Figure 4.2 shows the finite element mesh used to obtain dW/dV values for the initial growth segment when $\beta = 15°$. It is made up of 76 twelve-noded isoparametric elements which are composed of 440 nodal points. The grid pattern for $\beta = 75°$ is displayed in Figure 4.3. Output values of strain energy density are obtained from the finite element code APES [37] at numerical integration or Gaussian points rather than at the more traditional nodal points. A special program uses the isoparametric elements shape function to extract values at these Gaussian points. This is because values at the nodal points are obtained from those at the Gaussian points by applying a smoothing technique. If values at the Gaussian points are used, more control over the smoothing of values is obtained.

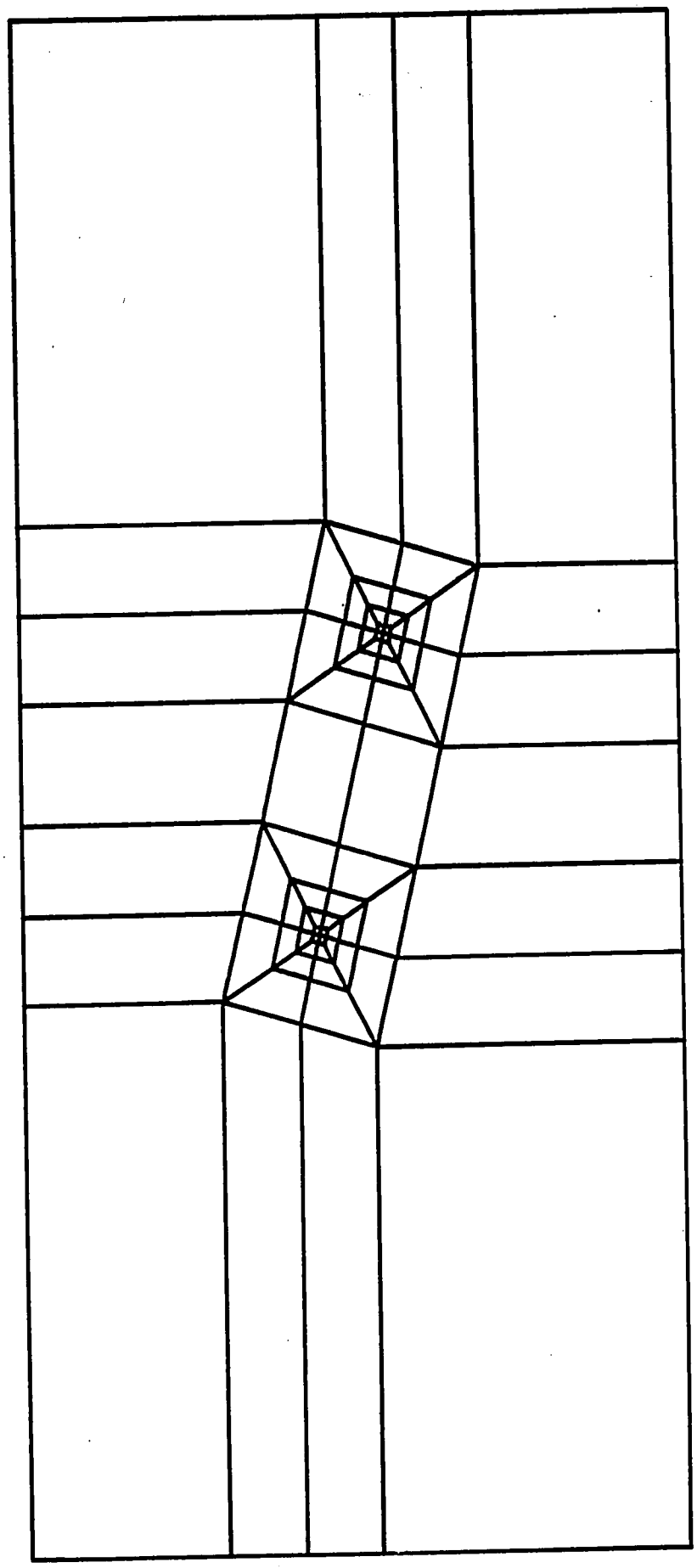

Figure 4.2. Grid pattern for crack tilted at $\beta = 15°$ with load axis being vertical.

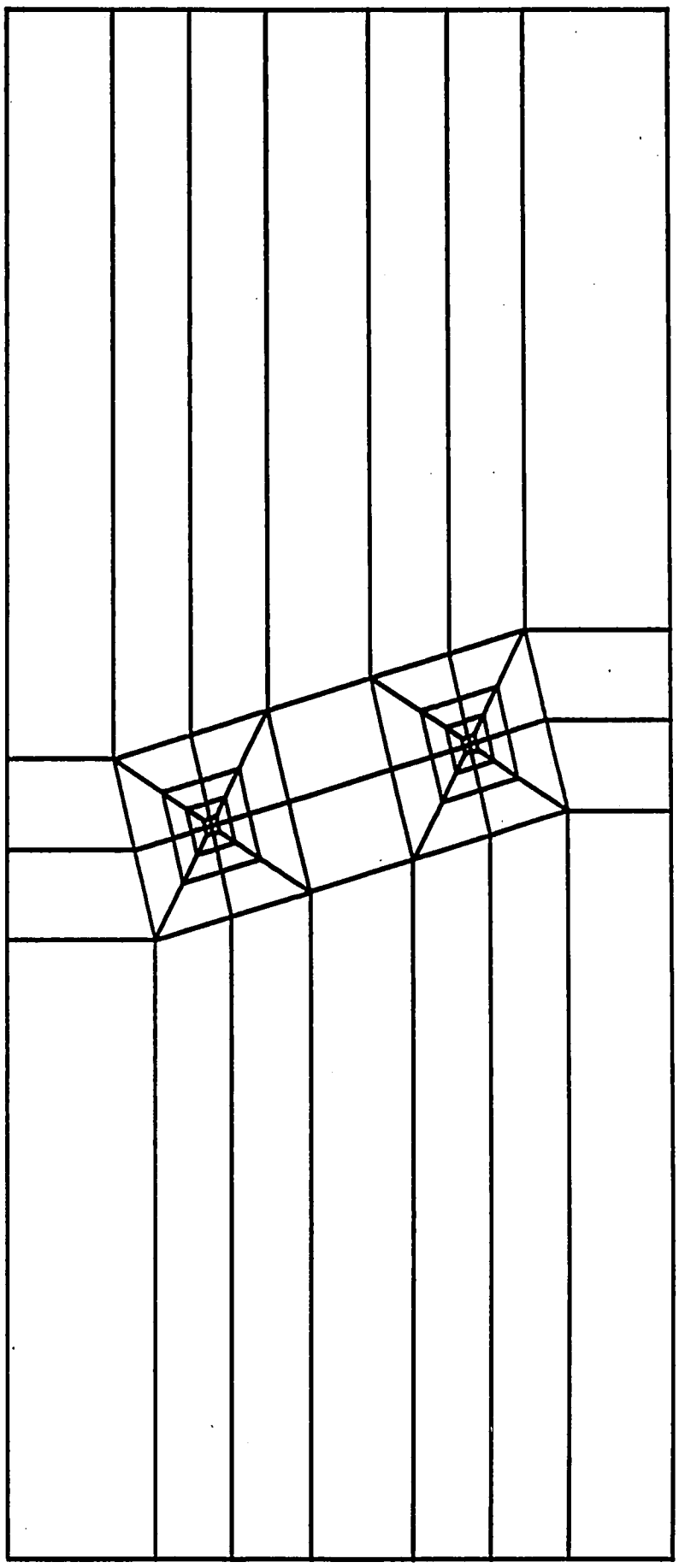

Figure 4.3. Grid pattern for crack tilted at $\beta = 75°$ with load axis being vertical.

4.3 Direction of Crack Initiation

Ultimately, the data used for the analysis of crack growth includes only the coordinates of Gaussian points and the strain energy density values for these points. Smoothing of data and plotting of strain energy density is performed by two software packages, Surfer and Grapher [38], produced by Golden Software, Inc. Both the crack growth direction and magnitude are determined by the distribution of strain energy density. The software package Surfer will plot constant dW/dV contours from a mesh of evenly spaced data points. Because strain energy density values come from Gaussian points of elements with a large range of sizes, the data points output from APES must be interpolated into a regular spacing, with values determined at the intersection points of a mesh laid over the specimen. Various interpolation methods are available and the density of the interpolated mesh is limited only by computer time and memory. For a typical plot, it was found that a good balance of contour smoothness and accuracy with calculation time results in a grid composed of 100 grid elements per side. Two different interpolation techniques were used, depending if the priority was on keeping Gaussian point values fixed, and sacrificing smoothness of contours, or having smooth contours for which exact values at Gaussian points have been sacrificed.

The MinCurv interpolation method was used to generate the grid used to determine the direction of crack growth because, although exact values at Gaussian points are not preserved, the resulting contours are

smooth, lending themselves to the determination of the direction of crack growth. The MinCurv algorithm fixes grid values at points containing input data and attempts to smooth remaining grid points using an iterative technique. Its strength is in projecting trends, so the magnitude of results may be unpredictable. Once an area has been gridded, contours of constant strain energy density are plotted with element boundaries overlaid. The direction of crack growth is determined by the location of $(dW/dV)_{min}^{max}$ at r/a = 0.1 as explained in Section 2.1 with reference to the core region. The location of this point is facilitated by drawing a circle of radius .1a about the crack tip. Once a line is drawn from the crack tip in the direction of crack growth, a protractor can be used to measure the fracture angle $-\theta_o$ indicated in Figure 4.1 with accuracy exceeding that of the data used to generate the energy density contours. Figure 4.4 shows such a plot for the initial crack growth segment for $\beta = 15°$. The corresponding three-dimensional plot showing the valley of $(dW/dV)_{min}$ can be found in Figure 4.5.

4.4 Crack Growth Segment

Once the fracture angle is known, there remains the determination of the crack growth segment. Because the amount of crack growth is more sensitive to the magnitude of dW/dV than its smoothness, the InvDist interpolation method was used to generate the grid used to plot the values of strain energy density in the direction of proposed crack growth. The InvDist interpolation method determines values at grid

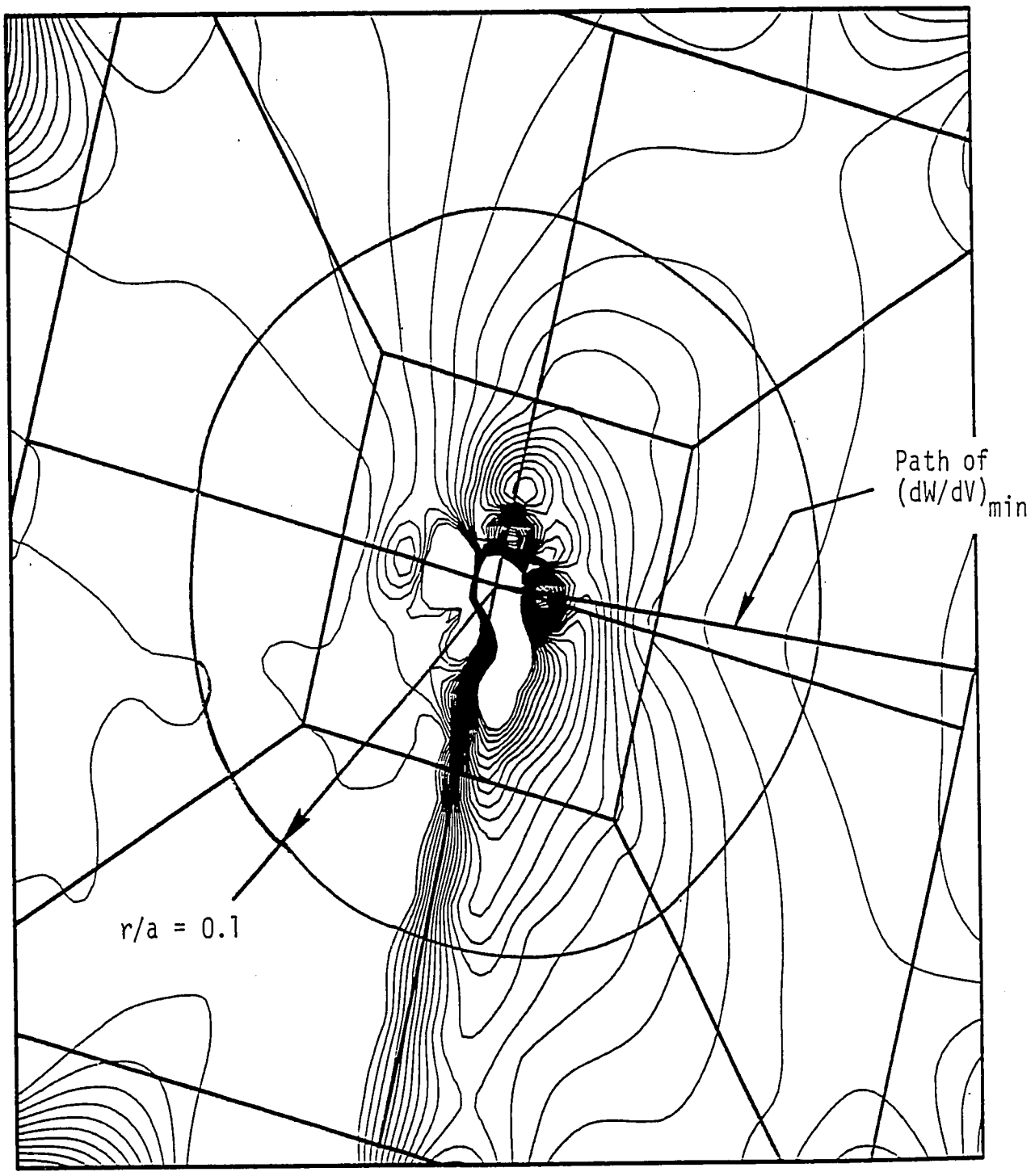

Figure 4.4. Constant contours of strain energy density and location of $(dW/dV)_{min}$ for $\beta = 15°$.

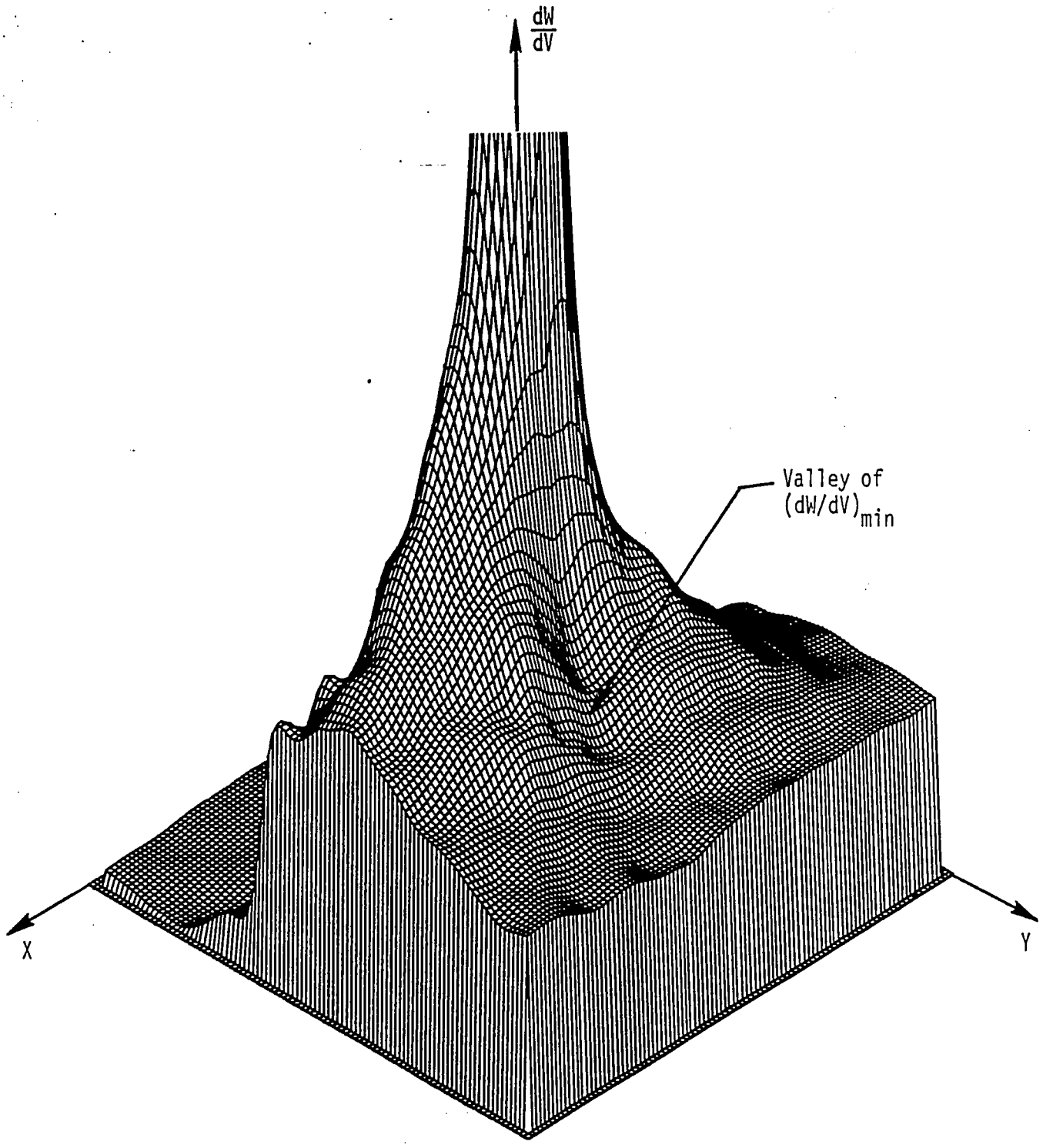

Figure 4.5. Variations of energy density dW/dV near crack for $\beta = 15°$ in two dimensions.

points, say Z_i, in a manner such that the influence of data at a point declines with the distance from the point d_i at which a value is being determined, i.e.,

$$Z = \sum_{i=1}^{n} \frac{Z_j}{(d_i)^2} \Big/ \sum_{i=1}^{n} \frac{1}{(d_i)^2} \qquad (4.1)$$

with n being the number of Z elements. The rate at which influence declines can be varied by adjusting the distance weighing power, but for this analysis, it is kept at its default value of two. In some cases, the smoothness of data is not adequate, so a smoothing technique is employed, which has the effect of smoothing out any local fluctuations in the data. Once a regularly spaced grid is created with satisfactory smoothness, a Surfer utility is used which takes a two-dimensional cross section from a three-dimensional Surfer plot. This cross section is imported into the package Grapher, where strain energy density is plotted versus the distance from the crack tip in the direction of crack growth. The critical value of strain energy density as well as a grid are superimposed over the plot, allowing the magnitude of crack growth to be determined in the manner already discussed. Shown in Figure 4.6 is a plot of dW/dV versus the radial distance from the crack tip in the direction of crack growth from which the amount of crack growth with overshoot was calculated for the first crack growth segment when $\beta = 15°$. The critical value of strain energy density, $(dW/dV)_c$, is plotted to facilitate the calculation of the growth attributed to both $(dW/dV)_c$ and overshoot energy. According to the data in Figure

4.6, the values of r_o+r_1 and r_1^o are 0.0584 cm and 0.0381 cm, respectively with r_o = 0.0254 cm. For added accuracy, the plot was sometimes

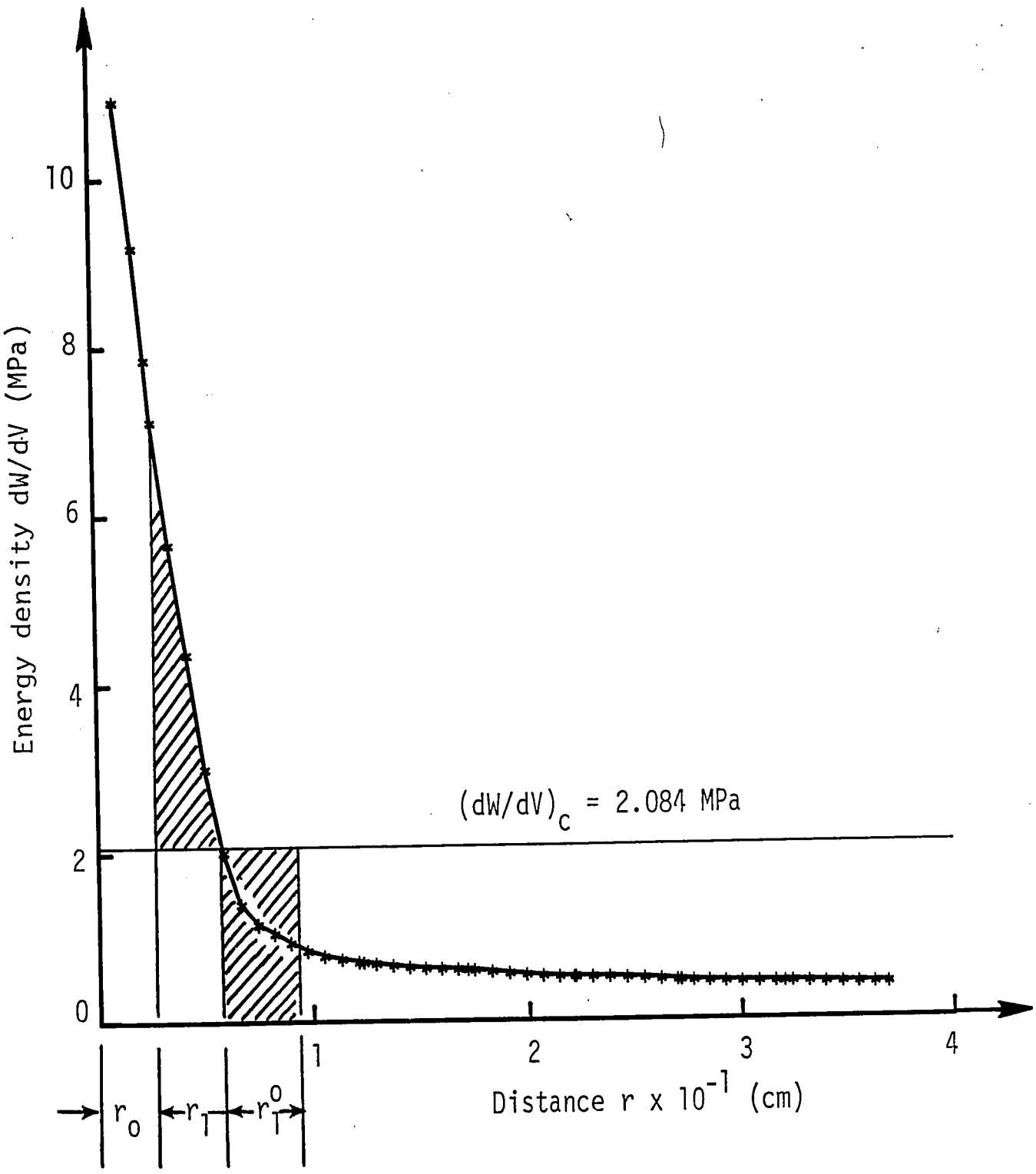

Figure 4.6. First segment crack growth with overshoot for β = 15°.

broken up into several areas, but it was found that results did not differ significantly. The size of the grids were made as small as possible to increase accuracy.

Once the crack growth direction and magnitude was determined, the crack geometry was remeshed and the process repeated until the ligament of unfractured material became smaller than the proceeding growth segment. More details on this will follow subsequently.

V. DISCUSSION OF RESULTS

Repeated remeshing of the finite element grid pattern of each segment of crack growth has yielded information on the stress, strain and energy distribution in the cracked plate as well as the crack trajectories. Considered are five different cases where β is increased from 15° to 75° in even increments. The method of solution correcting for overshoots has already been discussed in Section IV. Critical stresses corresponding to crack initiation are determined. This would provide the means to correlate fracture data for the angled crack specimen. Data scatter caused by overload is also discussed to better the interpretation of analytical results.

5.1 Crack Trajectories

As mentioned earlier as well as in Section VII of the Appendix, the formation of the finite element grid that models the crack geometry is a very crucial part of the numerical stress analysis. Any inaccuracies or approximations would be reflected in the failure prediction. Two different meshes modelling the same geometry could yield very different results. Special care was taken in modelling the crack tip zone with consistent element meshing in the area of predicted crack growth being the major priority. Changing element sides by only five to ten percent in the vicinity of the crack tip was found to have marked effects on the strain energy density. Because of this, the crack tip zone was modelled consistently for every case. Accuracy is lost when the angle formed by adjacent element sides gets very small or very large; there-

fore, elements were kept rectangular when possible.

By application of the strain energy density criterion [27] or more specifically equation (3.14), r_1^*, r_2^*, etc., for each β could be computed. The crack trajectories for the five different crack angles are displayed in Figures 5.1(a) to 5.1(e) inclusive. The number of crack

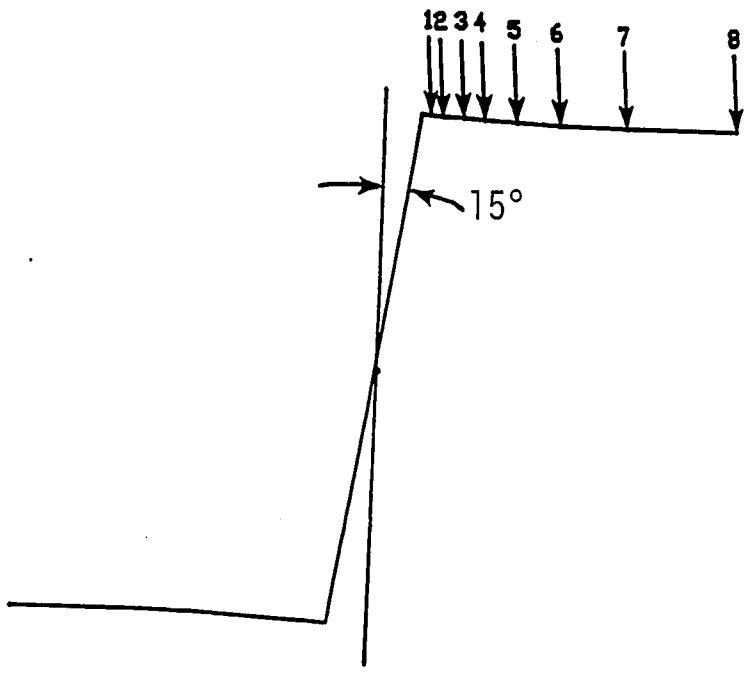

(a) Crack angle β = 15°

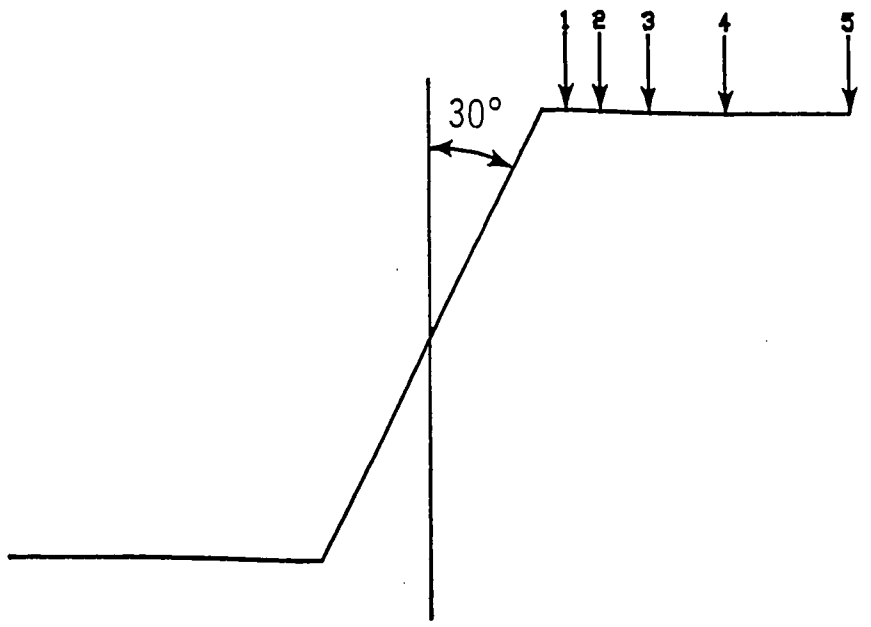

(b) Crack angle β = 30°

Figure 5.1. Crack trajectories following $(dW/dV)_{min}$ path for different crack angles.

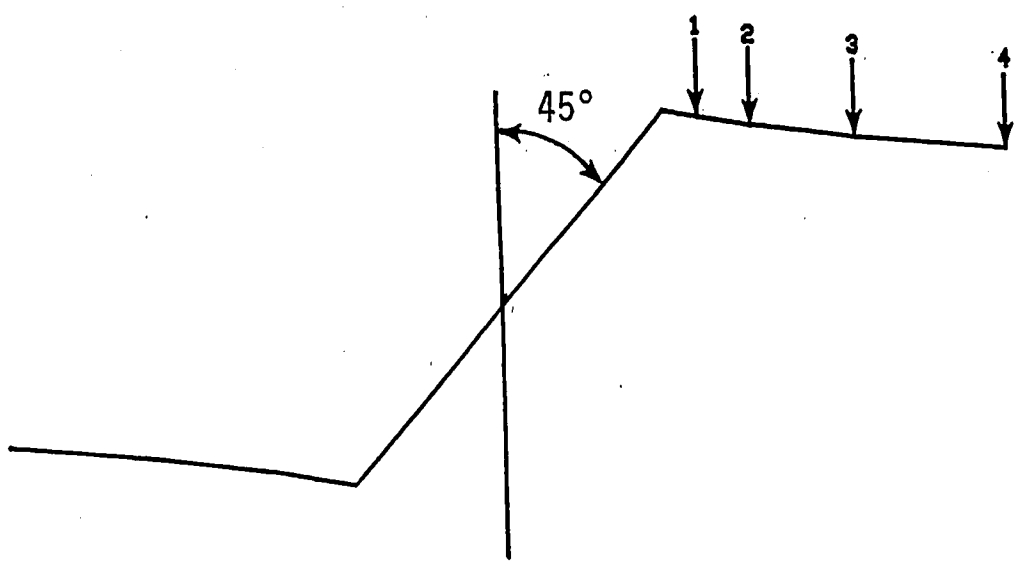

(c) Crack angle $\beta = 45°$

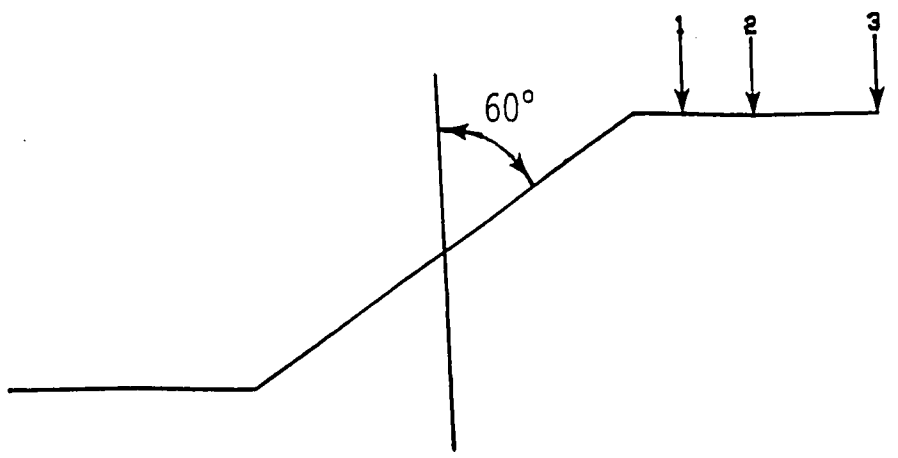

(d) Crack angle $\beta = 60°$

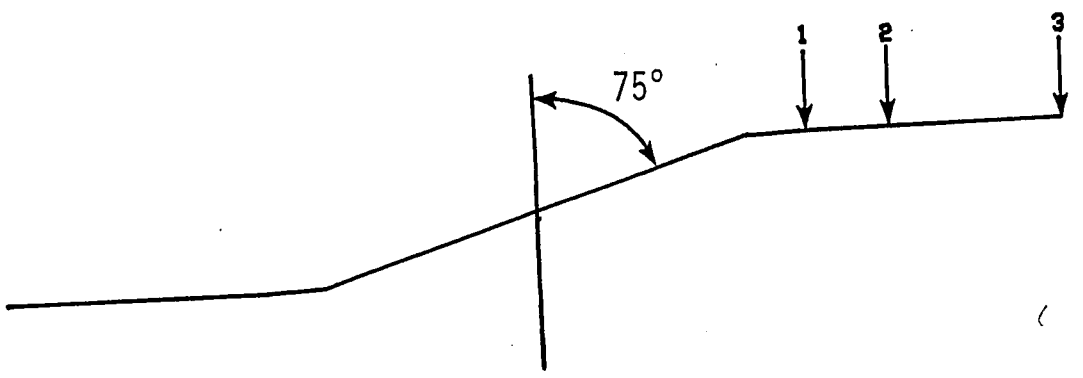

(e) Crack angle $\beta = 75°$

Figure 5.1. Crack trajectories following $(dW/dV)_{min}$ path for different crack angles (continue).

segments that could be taken in the computation before the plate fractures completely decreased with increasing crack angle β. Note the difference between eight (8) crack growth steps for $\beta = 15°$ as compared with three (3) crack growth steps for $\beta = 60°$ and 75°. This is to be expected because the stress level in the uncracked ligament is lower for small β because the ligament size would decrease as β is increased if the plate width is kept unchanged. In other words, as the ligament area supporting the load decreases, the stress in the ligament increases with the maximum stress corresponding to $\beta = 90°$.

Numerical values of the crack growth segments for each of the β in Figures 5.1(a) to 5.1(e) inclusive can be found in Table 5.1. Each segment of the crack growth contains three parts, namely r_o, r_j and r_j^o for j = 1,2, etc., as defined in Figure 4.6 while the sum of r_o+r_j and r_j^o is r_j^* as shown in equation (3.12).

To be kept in mind is that the numerical analysis contain approximations arising from the discretization of the continuum system into a finite number of nodal points. The results are affected by the ways with which the nodal points are arranged with reference to the angled crack. It is of interest to compare the present numerical results with those in [17] that are reproduced in the transparent overlay in Figure 5.2(a) and 5.2(b) for $\beta = 30°$ and 45°, respectively. The solid line on the overlay corresponds to the $(dW/dV)_{min}$ path computed analytically for an infinite plate with an angle crack. Next to it on the overlay is the fractured specimen made of glass as referenced in [17]. For the

Table 5.1. Crack growth segments with overshoot for five (5) different values of crack angle β with $r_o/a = 10^{-2}$.

Growth Step j = 1,2, etc.	r_o+r_j (cm)	r_j^o (cm)	r_j^* (cm)
$\beta = 15°$			
1	0.058	0.038	0.097
2	0.064	0.076	0.140
3	0.074	0.163	0.236
4	0.079	0.147	0.249
5	0.094	0.267	0.361
6	0.107	0.378	0.485
7	0.132	0.622	0.770
8	1.257	1.021	1.278
$\beta = 30°$			
1	0.086	0.170	0.257
2	0.097	0.295	0.391
3	0.117	0.439	0.556
4	0.168	0.709	0.876
5	0.274	1.173	1.448
$\beta = 45°$			
1	0.112	0.307	0.419
2	0.135	0.465	0.599
3	0.193	0.759	0.953
4	0.340	1.422	1.763
$\beta = 60°$			
1	0.132	0.419	0.551
2	0.175	0.660	0.836
3	0.277	1.161	1.438
$\beta = 75°$			
1	0.147	0.493	0.643
2	0.198	0.775	0.973
3	0.381	1.605	1.986

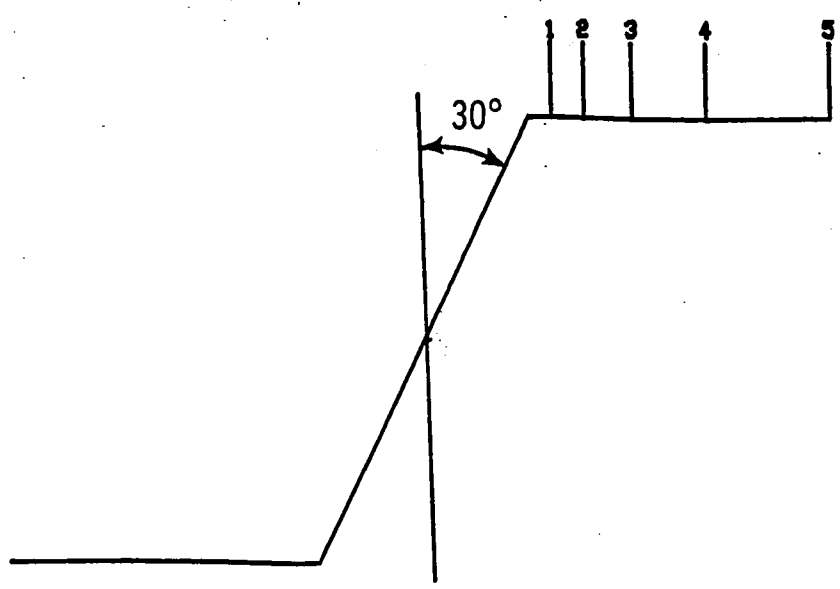

(a) Crack angle $\beta = 30°$

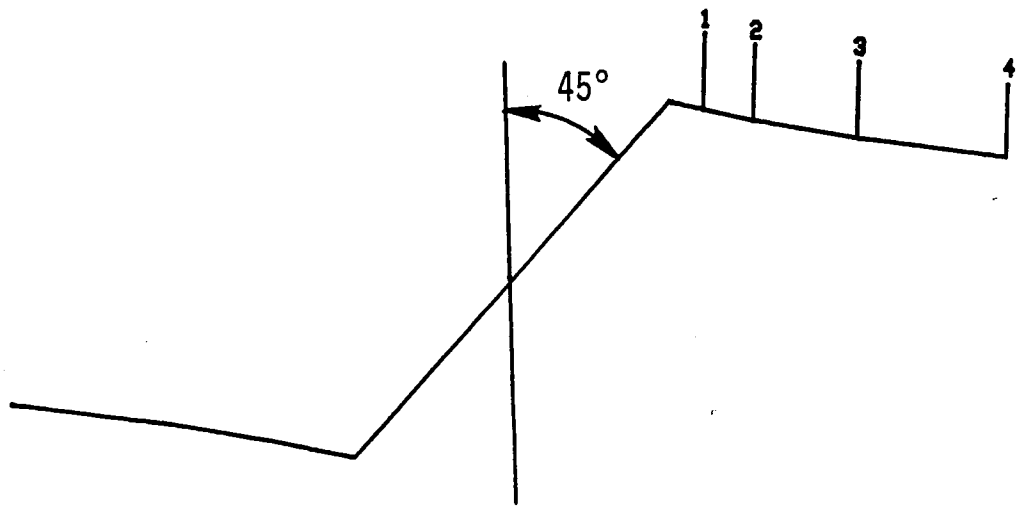

(b) Crack angle $\beta = 45°$

Figure 5.2. Comparison of crack trajectories obtained from finite element calculations with results in [17] and fractured specimen.

first two segments of crack growth, they are all nearly the same. The discrepancies become larger as the crack extends further and are to be expected because no plate edge effect is considered in [17] and the $(dW/dV)_{min}$ path corresponds to that for a straight line crack without considering the influence of a crack that extends as it turns. Approximations arising from the finite element calculations could not be delineated by examining the crack trajectories alone. Additional insights could be gained on the failure loads.

5.2 Change in Nominal Stress

Although for every crack growth segment, the remote stress applied to the plate is kept constant, the effective loading of the plate differs for each segment of crack growth. The load applied to the plate must be supported by the unfractured ligaments on each side of the crack. As the ligament size decreases, the load must be supported by a smaller area of material, thus the nominal stress in the plate increases. For a unit load, the nominal stress is simply the inverse of the unfractured ligament area. Table 5.2 contains values of ligament area and nominal stresses for each growth segment. Referring to Figure 5.3, the nominal stress for a unit load is defined as

$$\sigma_j = \frac{\text{unit load}}{A_j}, \quad j = 1,2, \text{ etc.} \tag{5.1}$$

where $A_j = b_j$ for a unit thickness plate.

Table 5.2. Nominal stress due to unit load on cracked specimen for different crack angles.

Growth Step * r_j	Ligament Area A_j (cm^2)	Nominal Stress σ_j (unit load/cm^2)
$\beta = 15°$		
1	11.384	0.0878
2	11.196	0.0894
3	10.917	0.0917
4	10.450	0.0957
5	9.997	0.100
6	9.281	0.108
7	8.321	0.120
8	6.787	0.147
$\beta = 30°$		
1	10.160	0.0984
2	9.647	0.104
3	8.865	0.113
4	7.757	0.129
5	6.005	0.167
$\beta = 45°$		
1	9.108	0.110
2	8.326	0.120
3	7.145	0.140
4	5.253	0.191
$\beta = 60°$		
1	8.301	0.120
2	7.201	0.139
3	5.530	0.181
$\beta = 75°$		
1	7.793	0.128
2	6.507	0.154
3	4.562	0.219

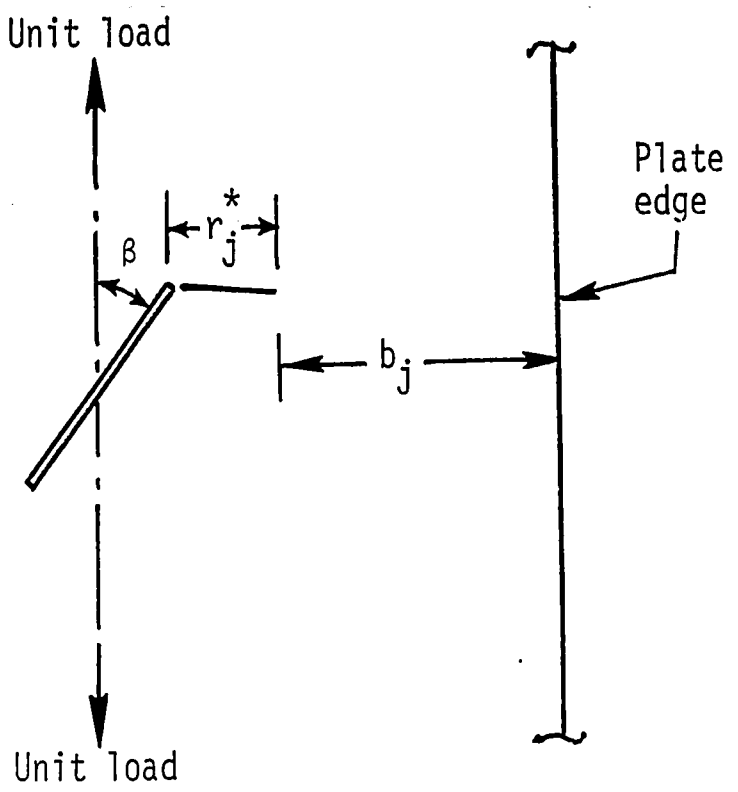

Figure 5.3. Cracked specimen subjected to a unit load.

The relation between nominal stress σ_j and crack growth segment r_j^* in Table 5.1 was the most obvious one to examine. Figure 5.4 shows nominal stress σ_j versus crack growth segment length for each initial crack angle $\beta = 15°, 30°, \ldots, 75°$. The curves for each β are nearly parallel to each other and are arranged in order of decreasing β. For a given σ_j, the total growth segment for a crack whose axis is nearly lined up with the direction of loading, i.e., small β, will be greater than that of a crack which is nearly perpendicular to the applied loading, i.e., large β. This finding may not be intuitive upon initial examination. What it implies is that for the same plate width more crack growth would take place for small β than the case of large β before reaching some critical effective crack length.

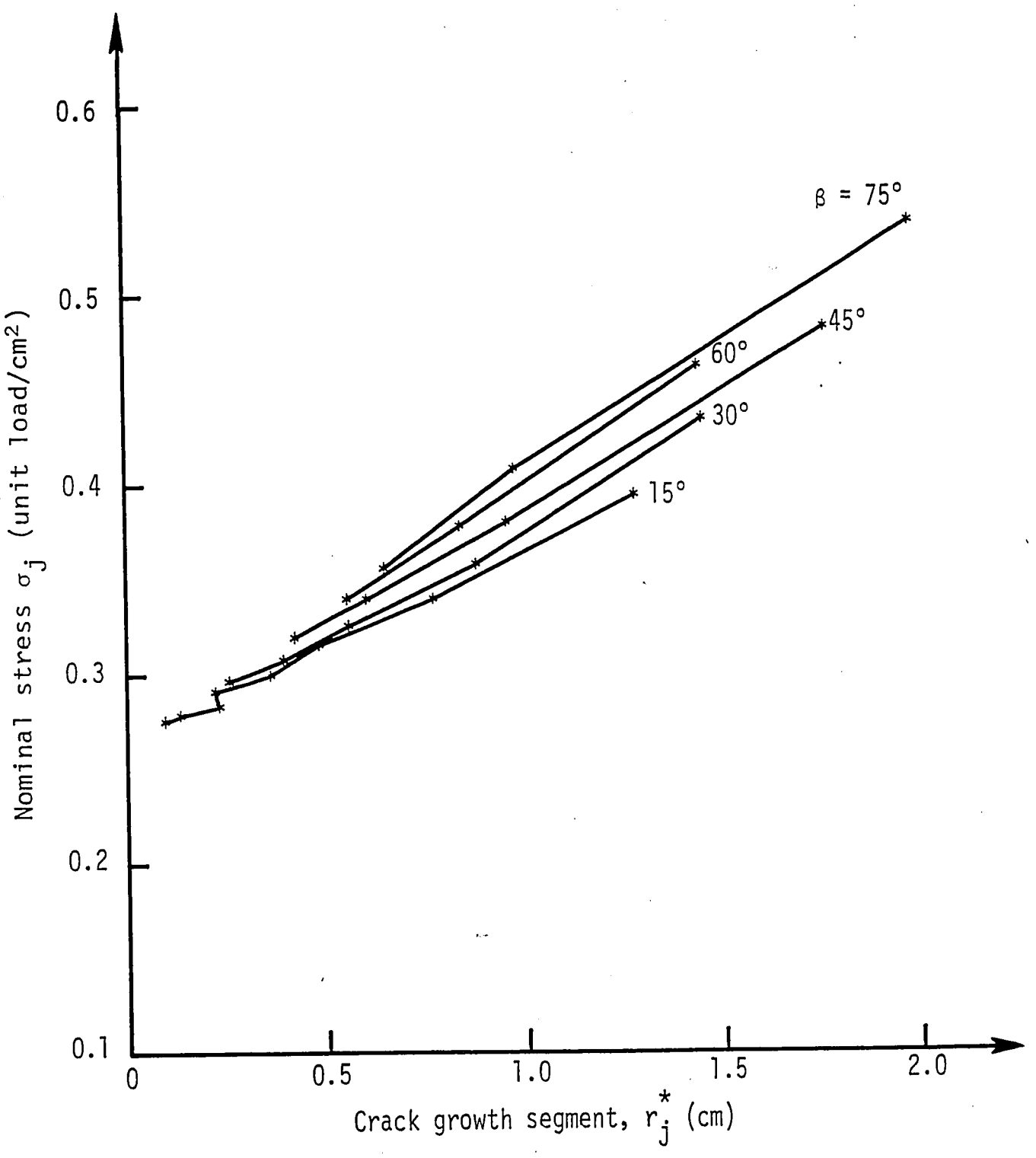

Figure 5.4. Nominal stress versus crack growth segment with overshoot.

5.3 Near Field Strain Energy Density

Another relation examined was the effect of the strain energy density at a radial distance of r = 0.1a from the crack tip in the direction of predicted fracture on the increment of crack growth. Figure 5.5 is a plot of dW/dV at r/a = 0.1 in the direction of proposed crack growth. It is apparent that the trend of the graph shows a common intersection at a value of dW/dV equal to approximately 2.00×10^6 N/m^2. This value corresponds to about 96 percent of the critical value $(dW/dV)_c$ in Table 4.1. A blow-up of this intersection region is shown in Figure 5.6. It becomes apparent that the data for $\beta = 15°$ does not intersect at the common intersection point of the other data, and there is some scatter in the intersection points. This is attributed to numerical inaccuracy of the finite element method.

5.4 Overload of Angled Crack Specimen

The concept of overload introduced in Section 3.2 for symmetric loading applies equally well to the angled crack configuration except that the equivalent strain ε in equation (3.1) or (3.2) should be modified to read as

$$\varepsilon = \frac{1-\nu^2}{E}\left[1 + \frac{2\pi a^2 f(\beta)}{A}\right]\sigma \qquad (5.2)$$

The function $f(\beta)$ accounts for the change in the plate stiffness depending on the crack angle β. An effective modulus of elasticity can thus be defined similar to that in equation (3.3) as

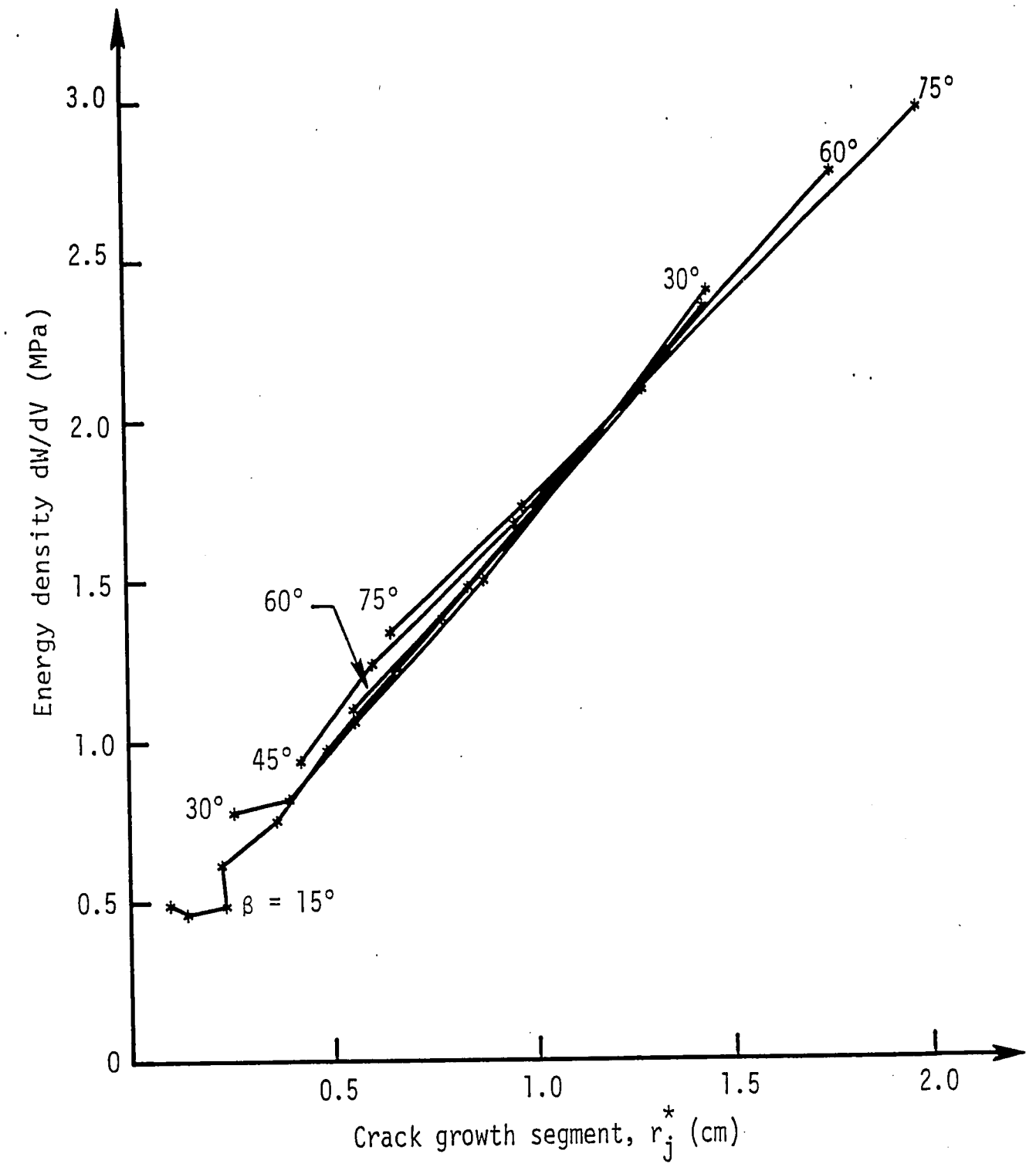

Figure 5.5. Variations of energy density at r/a = 0.1 with crack growth segments for different β.

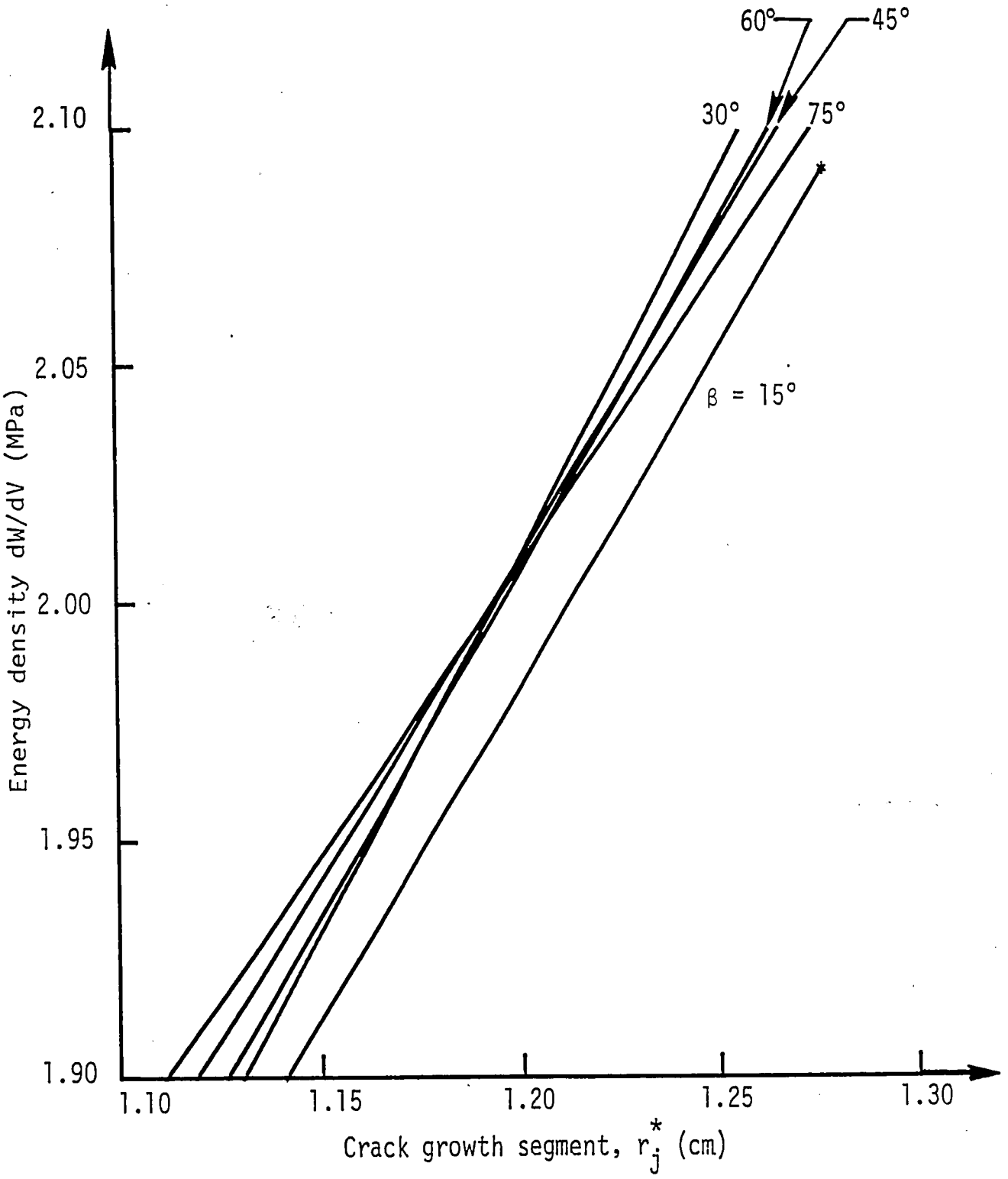

Figure 5.6. Enlarged view of intersection region in Figure 5.5 for r/a = 0.1 and different β.

$$E^* = \frac{E}{1 + \frac{2\pi a^2}{A} f(\beta)} \qquad (5.3)$$

such that $f(\beta) \to 1$ when $\beta = \pi/2$. Prior to discussing overload, E^* must be determined for the angled crack configuration.

Effective Modulus. There are three ways for estimating E^*; they will be referred to as the infinite plate result, total energy approach and critical stress/strain solution. For an infinite plate, equation (5.3) can be derived in closed form from equations (2.42) and (2.44) in [35]. This is accomplished by setting $\kappa = 3-4\nu$ for plane strain and shrinking the elliptical notch to a sharp crack of length 2a. The quantities p and q in [35] are related to σ and β in this work as follows:

$$2p = \sigma(1-\cos 2\beta), \quad 2(\varepsilon p) = \sigma(1+\cos 2\beta), \quad 2q = \sigma \sin 2\beta \qquad (5.4)$$

such that the total energy in an infinite plate with an angle crack reduces to

$$W = \frac{(1-\nu^2)\sigma^2 A}{2E} + \frac{\pi(1-\nu^2)\sigma^2 a^2}{2E}(1-\cos 2\beta) \qquad (5.5)$$

An effective modulus can thus be extracted from the above expression as

$$E^* = \frac{E}{1 + \frac{\pi a^2}{A}(1-\cos 2\beta)}, \quad \text{(Infinite plate)} \qquad (5.6)$$

Alternatively, E^* can be computed directly from the total energy in a finite plate given by

$$W = \frac{1+\nu}{2E} \iint_A [(1-\nu)(\sigma_x^2+\sigma_y^2) - 2\nu\sigma_x\sigma_y + 2\tau_{xy}^2]dxdy \qquad (5.7)$$

since the stresses σ_x, σ_y and τ_{xy} are known from the finite element analysis. That is, E^* can be computed from

$$E^* = \frac{1-\nu^2}{2}\left(\frac{\sigma^2 A}{W}\right), \quad \text{(Total energy)} \qquad (5.8)$$

once $(\sigma^2 A/W)$ is known. Knowing that $W \sim \sigma^2$, E^* in equation (5.8) would be independent of the applied stress level chosen for computing W. The third approach is to use the critical stress and strain relation for plane strain:

$$E^* = (1-\nu^2)\left(\frac{\sigma_c}{\varepsilon_c}\right), \quad \text{(Critical stress/strain)} \qquad (5.9)$$

where (σ_c,ε_c) is a point on the failure envelop. Equations (5.8) and (5.9) should yield approximately the same results because both methods involve stresses and strains obtained for the finite plate while equation (5.6) applies to the infinite plate.

Using the E and ν values given in Table 4.1, a = 2.54 cm and A = (25.4)(12.7) = 322.58 cm^2, WA/σ^2 and (σ_c,ε_c) are calculated and given in Table 5.3 from which E^* in equations (5.8) and (5.9) can be found. Variations of E^* with β are displayed graphically in Figure 5.7. To begin with, all the curves intersect at $\beta = 0°$, i.e., when $E^* = E$ = 2.363 GPa being the elastic modulus of PMMA. The crack would not influence the plate stiffness when it is collinear with the uniaxial ap-

Table 5.3. Effective modulus as a function of crack angle obtained from equations (5.6), (5.8) and (5.9).

Crack Angle β (deg.)	Normalized Total Energy $(WA/\sigma^2) \times 10^{-2}$ (cm^2/MPa)	Critical Stress σ_c (MPa)	Critical Strain $\varepsilon_c \times 10^{-3}$ (m/m)	Effective Modulus E^* (GPa)		
				Eq. (5.6)	Eq. (5.8)	Eq. (5.9)
15°	6.131	17.33	6.579	2.343	2.339	2.342
30°	6.299	10.13	3.933	2.291	2.277	2.290
45°	6.468	8.48	3.398	2.223	2.210	2.219
60°	6.720	7.49	3.102	2.159	2.134	2.147
75°	6.967	6.85	2.907	2.115	2.058	2.099

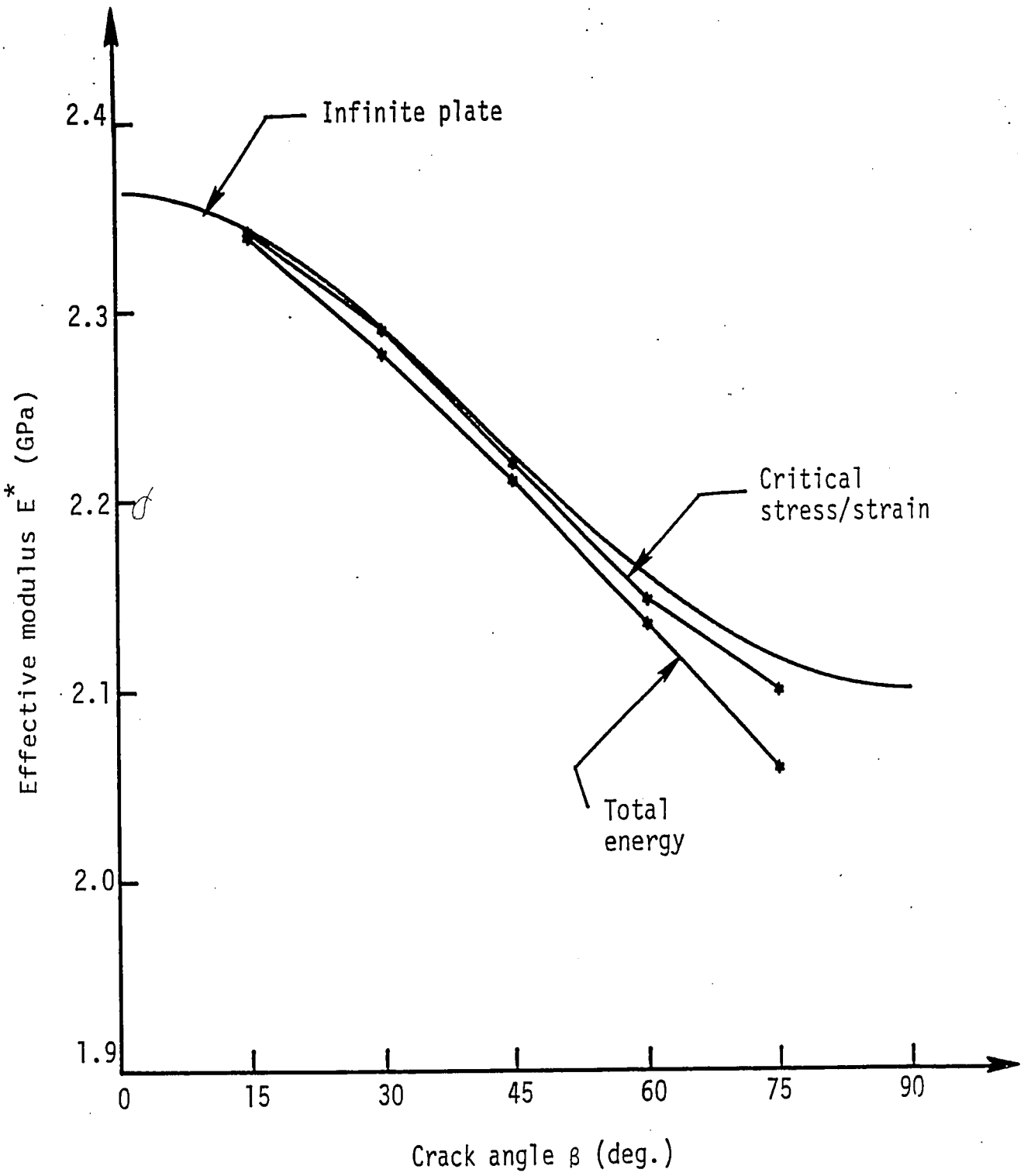

Figure 5.7. Change of effective modulus with crack angle for fixed crack length.

plied load. As β increases, the net section area reduces accordingly and hence E^* would decrease as shown in Figure 5.7. More reduction in E^* is seen for the finite plate as expected. The total energy curve accounts for weighing the finite plate edge effect regardless of the applied stress level while the curve obtained from critical stress/strain state accounts only for the critical stress. It is therefore reasonable to expect that equation (5.9) would yield the lowest E^* for a given β.

The function $f(\beta)$ in equation (5.3) being load independent may be regarded as a correction to the infinite plate solution once E/E^* are known for different β. For the present problem, $A/2a^2 \simeq 25$ and hence equation (5.3) may be applied to obtain

$$f(\beta) = \frac{25}{\pi}\left(\frac{E}{E^*} - 1\right), \quad E^* < E \tag{5.10}$$

Numerical values of $f(\beta)$ for the three cases discussed earlier can be found in Table 5.4. The influence of the plate edge is small for small β. This can be seen from the data in Tables 5.3 and 5.4.

Failure Envelop. There are two ways to develop the failure envelops that describe the critical stress/strain states for different crack size and crack angle. For a fixed β, the ratio $A/\pi a^2$ or m in equation (3.8) could be varied and $(\sigma_c, \varepsilon_c)$ could be computed at the point, say $r/a = 10^{-2}$, when $(dW/dV)_{min}$ local to the angled crack tip reaches the critical value $(dW/dV)_c = 2.084$ MPa in Table 4.1. This

Table 5.4. Stiffness function for angled crack.

Crack Angle β (deg.)	Stiffness Function f(β)		
		Finite Plate	
	Infinite Plate	Total Energy	Critical Stress
15°	0.067	0.081	0.071
30°	0.250	0.302	0.254
45°	0.500	0.523	0.516
60°	0.750	0.854	0.801
75°	0.933	1.178	1.001
90°	1.000	-	-

would yield a series of failure envelops similar to that in Figure 3.4 for $\beta = \pi/2$.

An easier way would be to develop an analytical expression for the failure envelop similar to that in equation (3.5). Knowing the functional form

$$\varepsilon = B_1\sigma + \frac{B_2}{\sigma^3} \tag{5.11}$$

with $B_1 = (1-\nu^2)/E$, the critical state evaluated in Table 5.3 may be used to evaluate B_2. This gives

$$B_2 = [\varepsilon_c - \frac{1-\nu^2}{E}\sigma_c]\sigma_c^3 \tag{5.12}$$

for each β. Equation (5.11) can thus be written as

$$\varepsilon = \frac{1-\nu^2}{E}\sigma + [\varepsilon_c - \frac{1-\nu^2}{E}\sigma_c]\sigma_c^3 \frac{1}{\sigma^3} \qquad (5.13)$$

Numerical values of σ and ε in equation (5.13) are calculated for $\beta = 15°, 30°, \ldots, 75°$ and they are plotted graphically in Figures 5.8 to 5.12 inclusive. The position of the failure envelop shifts for each β as the plate stiffness E^* changes. This is illustrated by the five curves in Figure 5.13. Intersection of the line $\Delta\sigma/\Delta\varepsilon$ = const. representing the plate stiffness yields the critical state $(\sigma_c, \varepsilon_c)$ of incipient fracture in Table 5.3. Figure 5.14 shows that the critical stress σ_c required to initiate fracture increases rapidly as β is decreased; it attains its minimum value at $\beta = \pi/2$. Such a trend has been observed in previous work [27].

Overload Stress. As it is to be expected, those crack configurations in which the crack is nearly aligned with the direction of loading had a higher effective stiffness, while those aligned nearly perpendicular to the direction of loading had a lower effective stiffness. Correspondingly, the angle at which the stiffness curve intersected the failure envelop was smaller for smaller crack orientation angles. The results obtained from Figures 5.8 to 5.12 inclusive are summarized in Table 5.5. Referring to Figure 5.15, the overload stress σ_o is defined as that above and beyond the critical stress σ_c on the failure envelop. It is proposed that the ratio of overload stress to critical stress is proportional to a function of the angle at which the failure envelop is intersected, α, with the expression referred to as the

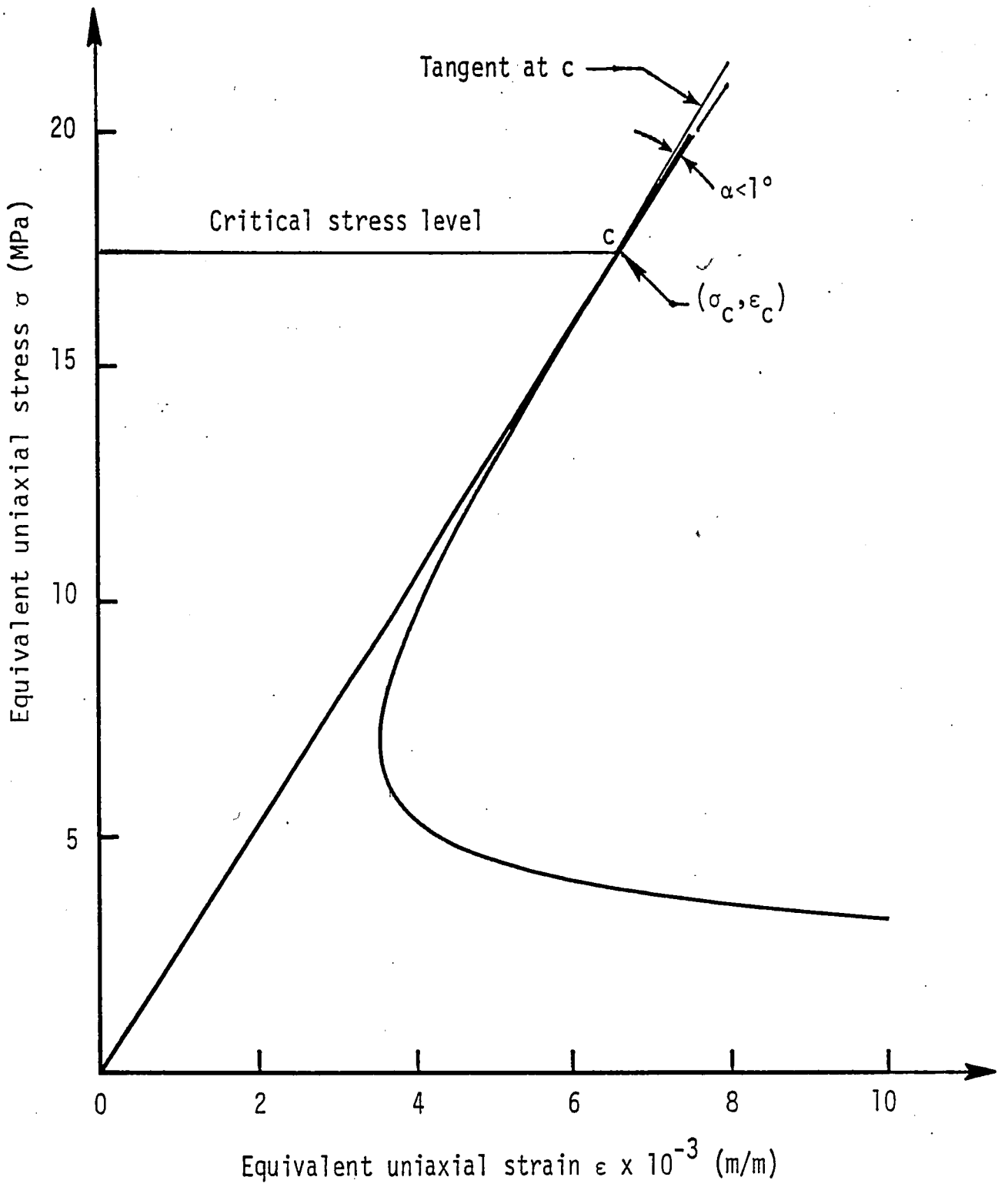

Figure 5.8. Failure envelop and critical stress/strain state for β = 15°.

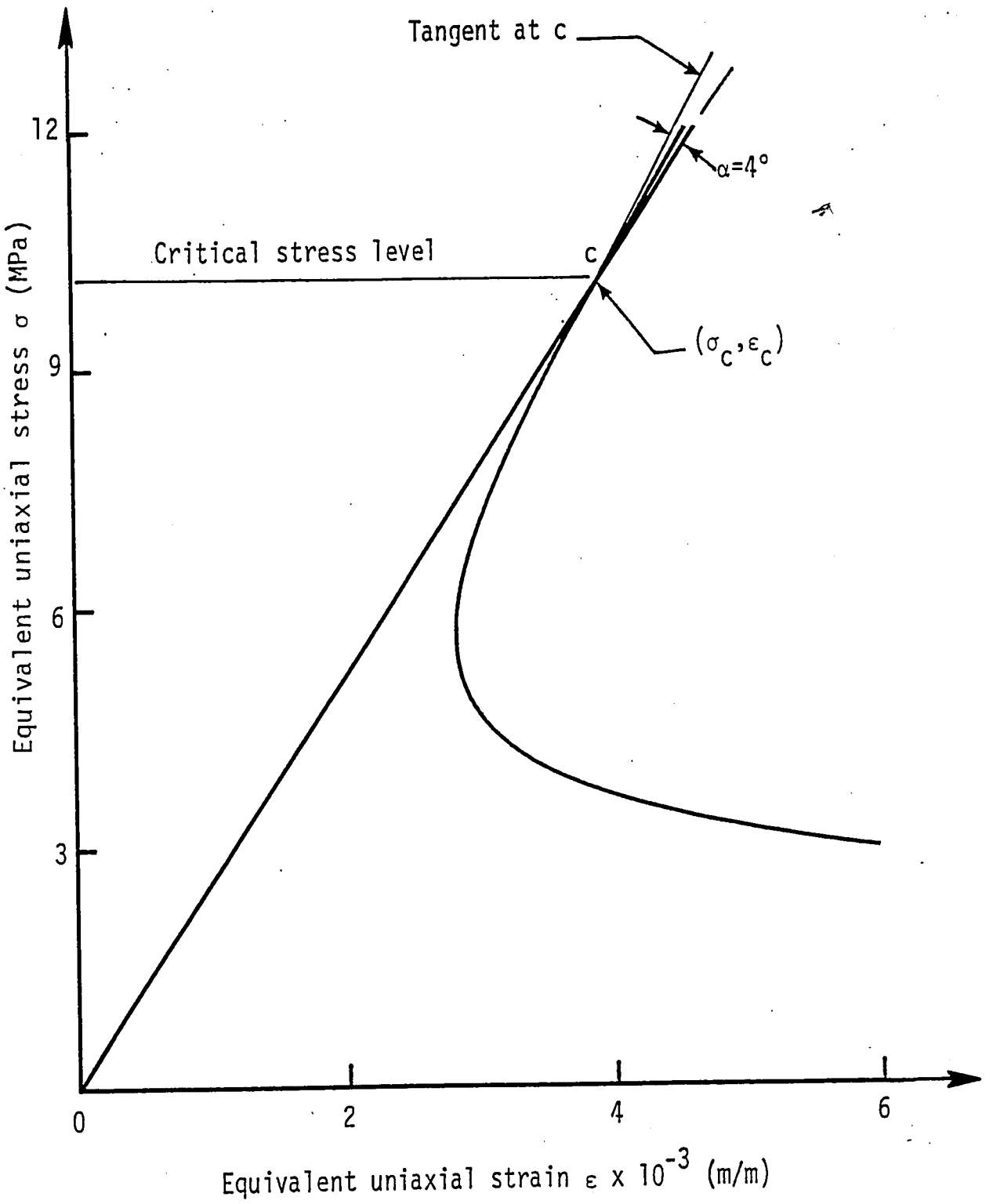

Figure 5.9. Failure envelop and critical stress/strain state for $\beta = 30°$.

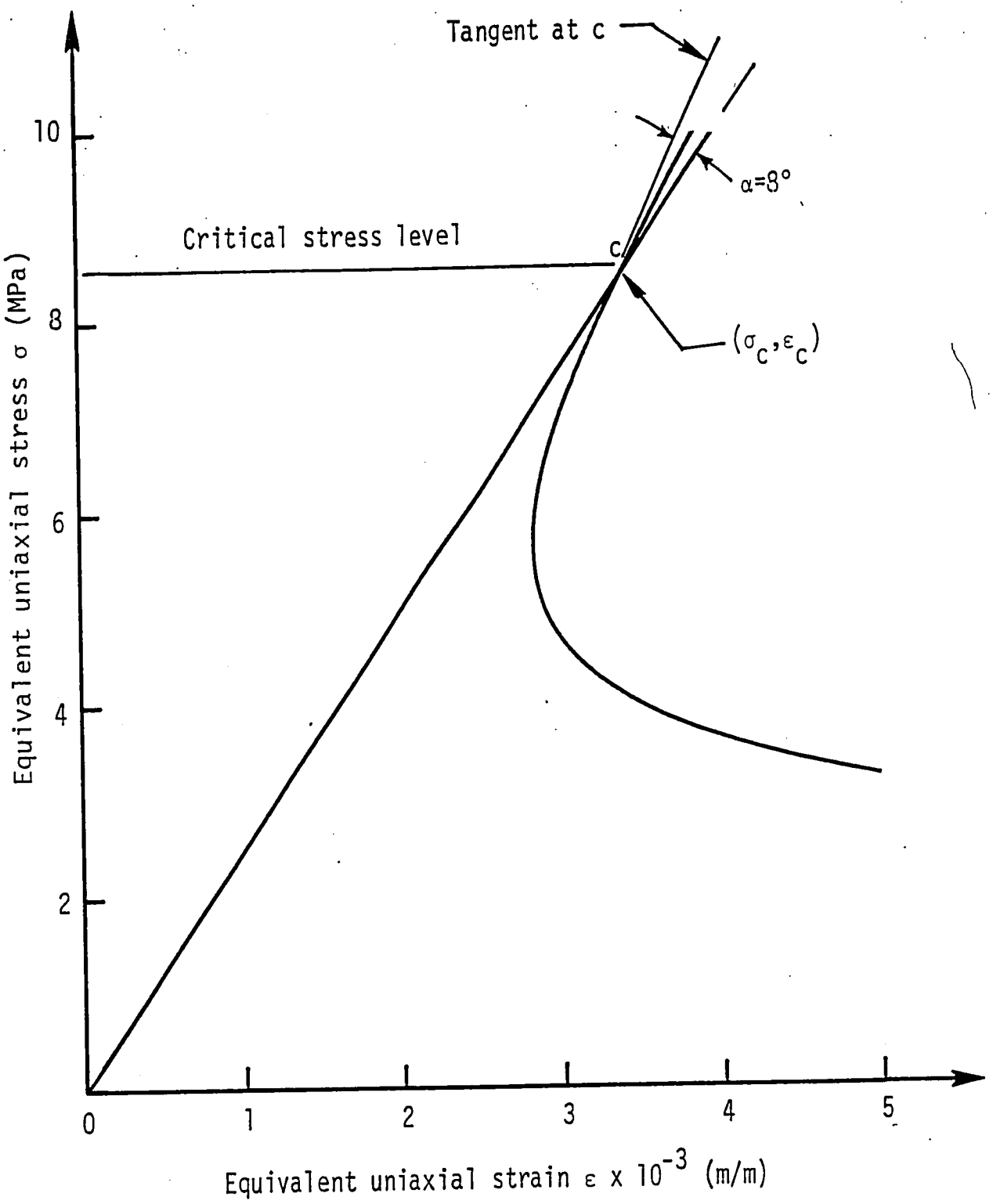

Figure 5.10. Failure envelop and critical stress/strain state for $\beta = 45°$.

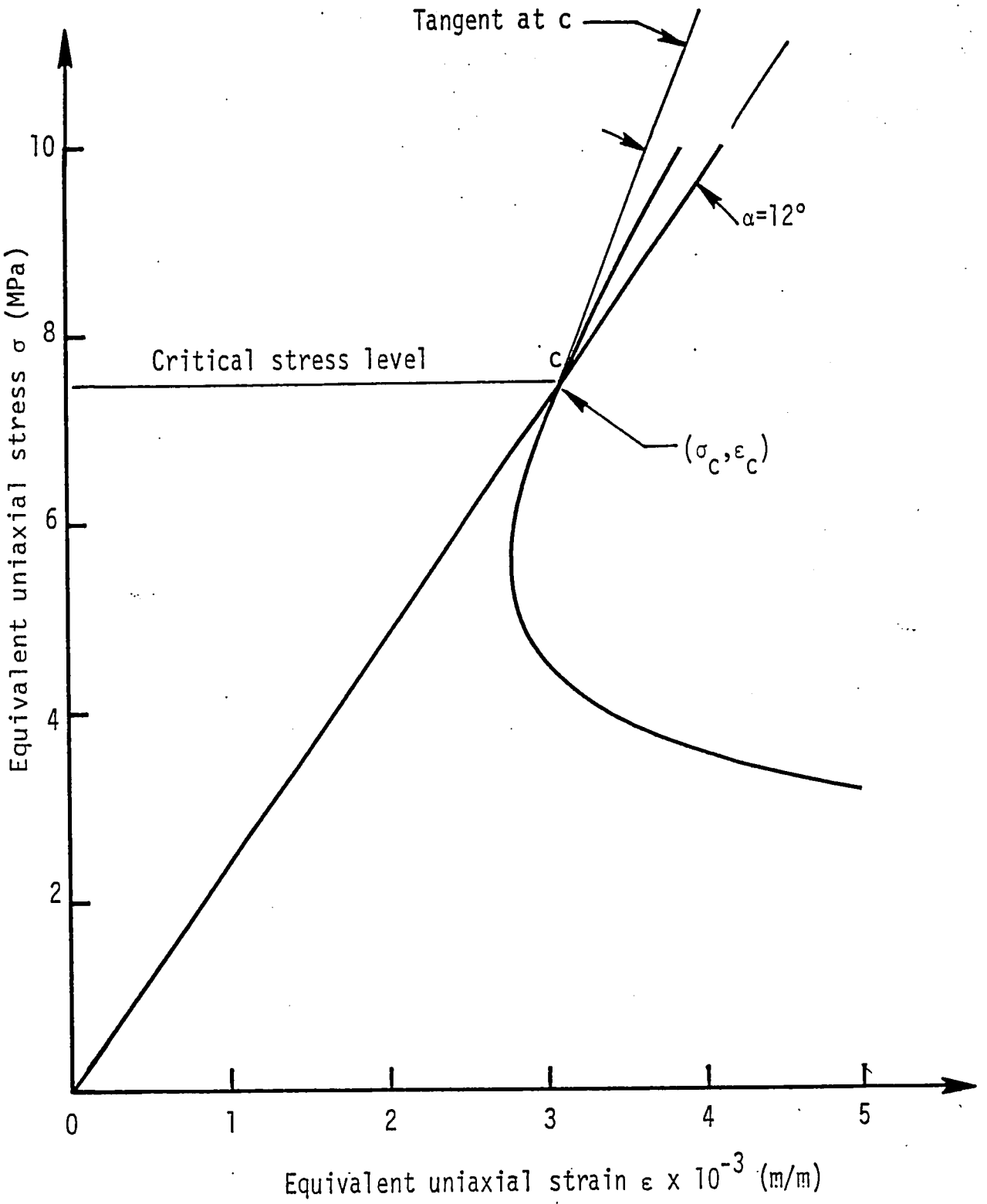

Figure 5.11. Failure envelop and critical stress/strain state for $\beta = 60°$.

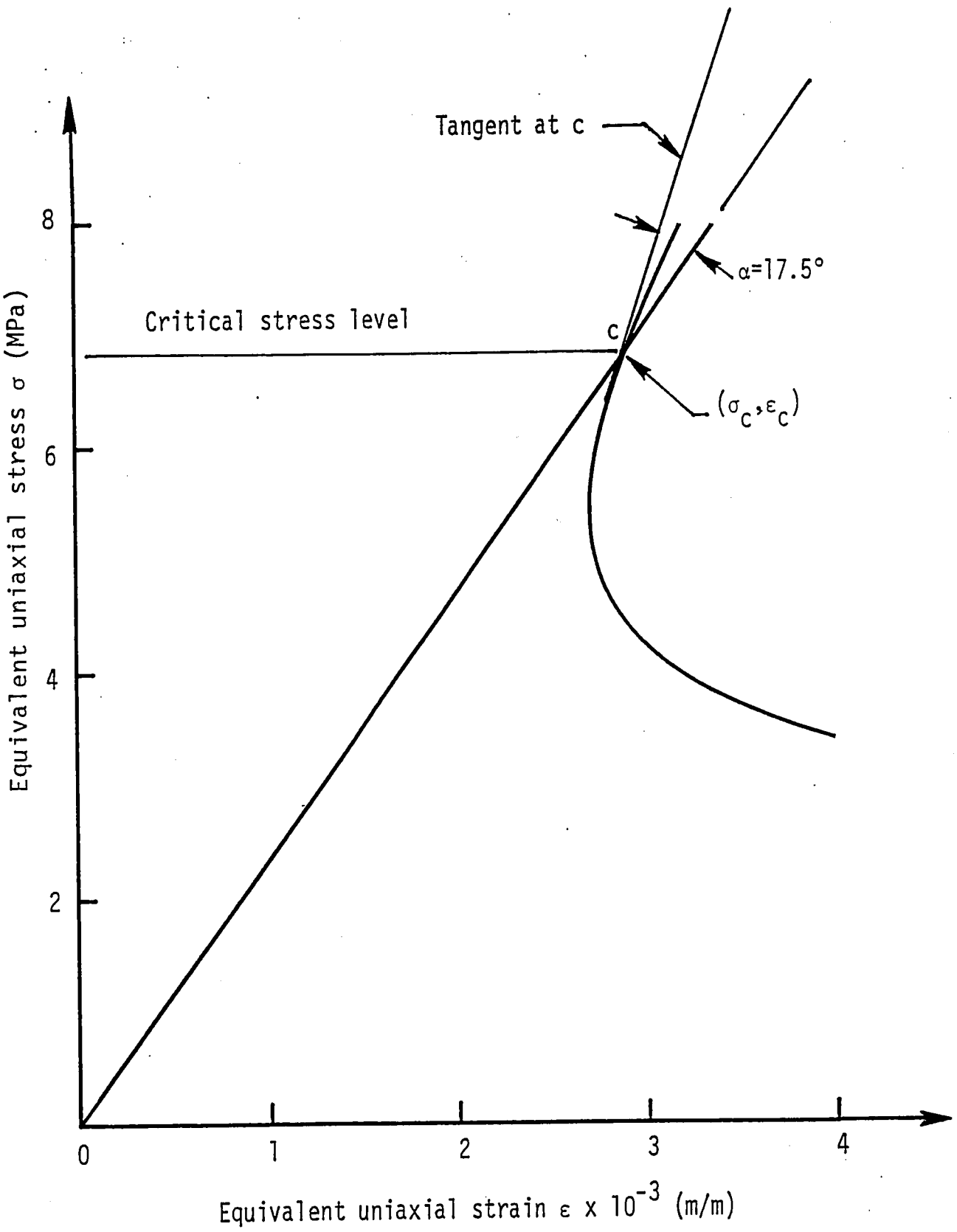

Figure 5.12. Failure envelop and critical stress/strain state for $\beta = 75°$.

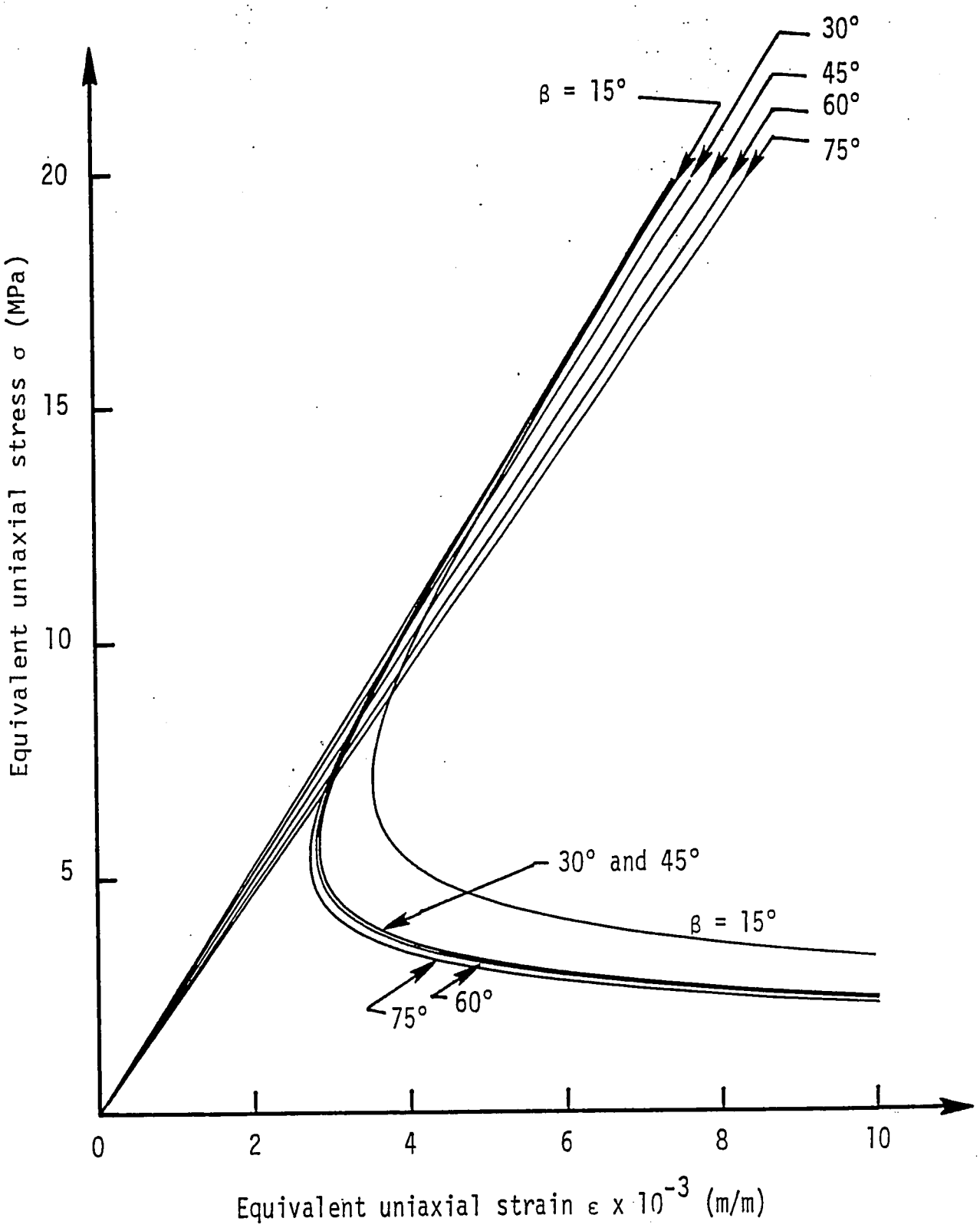

Figure 5.13. Comparison of failure envelops and specimen stiffness for different β.

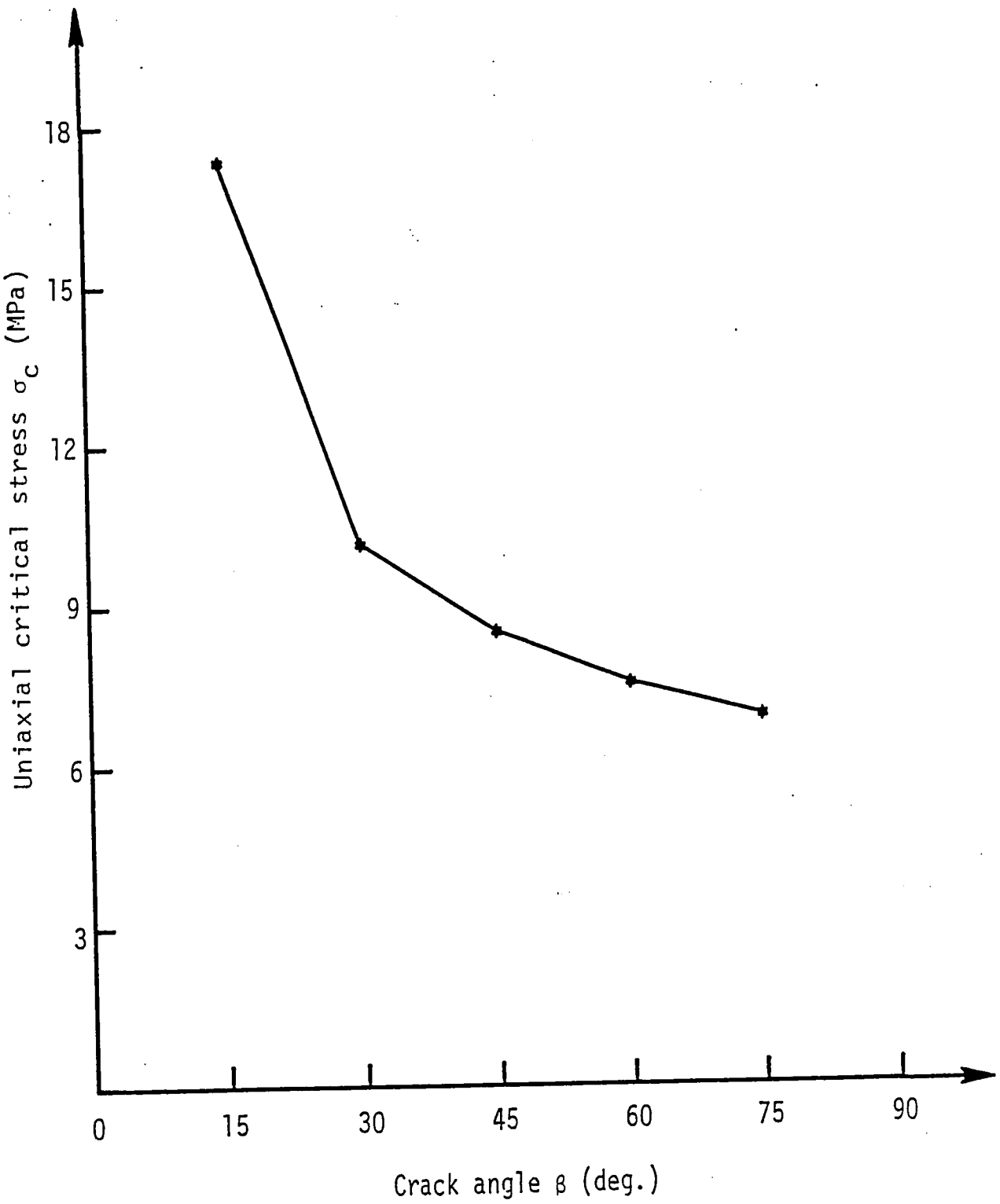

Figure 5.14. Variations of critical stress with crack angle corresponding to $(dW/dV)_c$ at $r/a = 10^{-2}$.

Table 5.5. Overload stress factor in percentage.

Crack Angle β (deg.)	Off Tangent Angle α (deg.)	Overload Stress Factor $\frac{90°-\alpha}{\alpha}$
15°	0.5	179
30°	4.0	21.5
45°	8.0	10.3
60°	12.0	6.5
75°	17.5	4.1

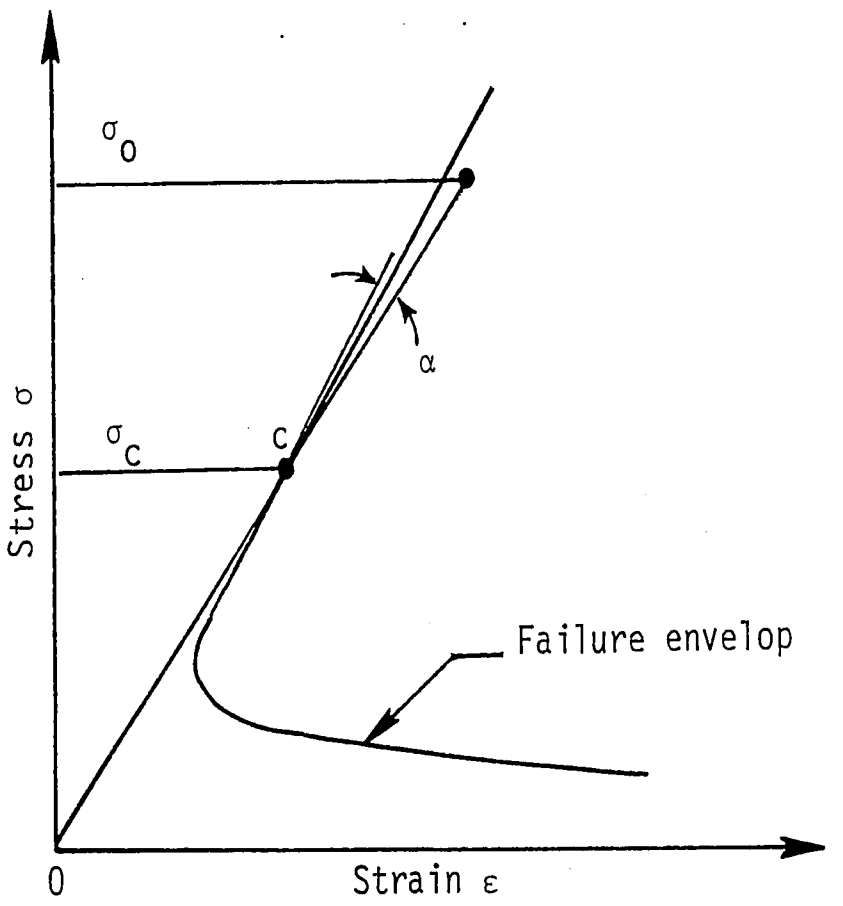

Figure 5.15. Overload stress for a specimen with linear response.

overload factor:

$$\frac{\sigma_o}{\sigma_c} = [n + (\frac{90°-\alpha}{\alpha})] \qquad (5.14)$$

For an angle of intersection approaching 0°, the corresponding overload factor would approach infinity while for an angle of intersection of 90°, the overload factor would be zero but not n because the actual load σ_0 must be slightly greater than σ_c in order for failure to take place.

As discussed in Section 3.2, an expected effect of overload would be an appreciable scatter in experimental data for large overload factors. Experimental work has been carried out which measures the failure load for the angled crack problem for different crack angles [16]. The results reported were gathered from two independent studies. For β greater than 45°, experimental data lies along a distinct path, while for β less than 45°, the scatter quickly becomes large. For β less than 10°, the scatter in critical stress becomes more than three times the critical stress for β = 90°.

VI. CONCLUSIONS AND FUTURE WORK

A methodology is presented for determining overshoot in crack growth because some of the elements along the prospective failure path would be stressed beyond the critical state. Such a condition is unavoidable when crack extension is simulated numerically as the sum of finite segments for step load increase. The data for generating these growth steps can be found in Section VII of the Appendix, both graphically and numerically. This consists of a total of 23 steps for the results in Figures 5.1(a) to 5.1(e) inclusive. The idealized model with overshoot would provide an upper bound solution. That is, for the same load, less crack growth would be predicted without overshoot which represents a lower bound solution. The experimental data should fall in between. Another previously unexplained phenomenon is data scatter caused by overload being the difference of the measured load at failure and that predicted by the assumed failure criterion. Demonstrated for the angled crack specimen is that the amount of overload tends to increase with increasing specimen stiffness. Having gained a better understanding of the problem of overshoot in crack growth and overload in crack initiation, several refinements on the proposed methodology can be made in the future.

6.1 Overshoot and Plastic Deformation

The crack trajectories in Figures 5.1(a) to 5.1(e) inclusive were derived by assuming that the material deforms elastically. Depending on the combination of load, crack geometry and material, significant

plastic deformation could take place such that less energy would be available to drive the crack.

Referring to Figure 6.1 for a typical element, the energy state,

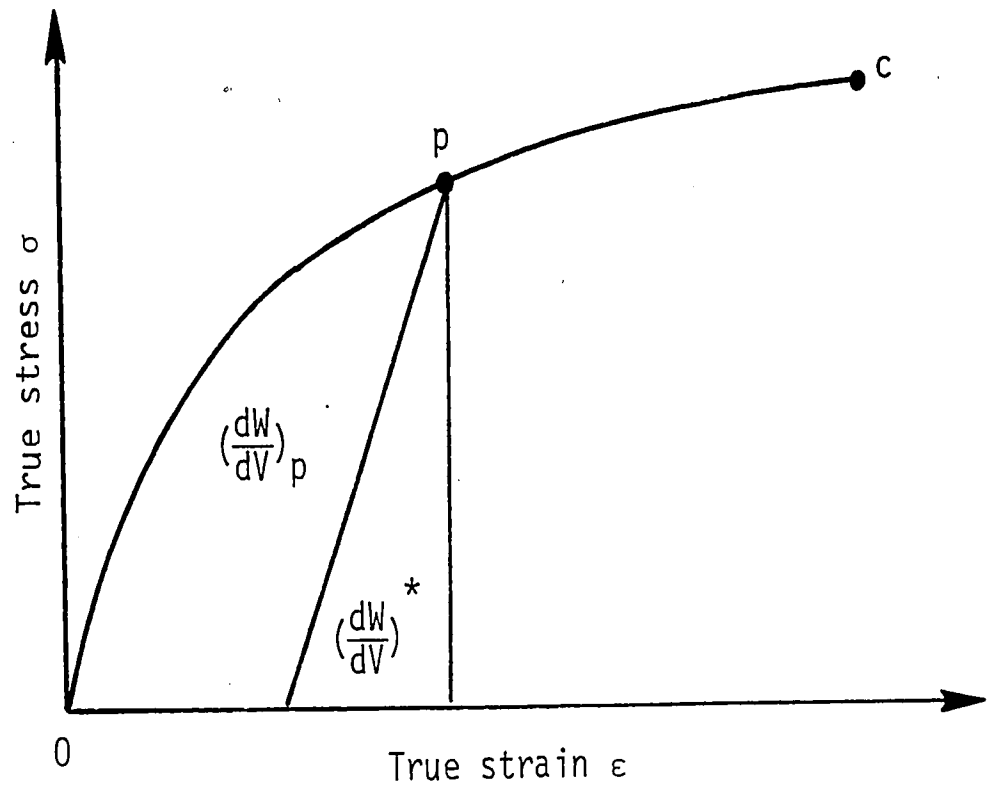

Figure 6.1. True stress and true strain curve.

say at p, could be regarded as

$$\frac{dW}{dV} = \left(\frac{dW}{dV}\right)_p + \left(\frac{dW}{dV}\right)^* \tag{6.1}$$

The portion used to deform the material plastically is $(dW/dV)_p$ while the remaining $(dW/dV)^*$ would be available to form new fracture surface. Since not all of the energy is available to create new crack surface, the point c in Figure 3.5 now becomes the intersection of the dW/dV curve obtained from an elastic-plastic stress analysis and the $(dW/dV)^*_c$ curve given in Figure 6.2. This differs from the elastic case in Fig-

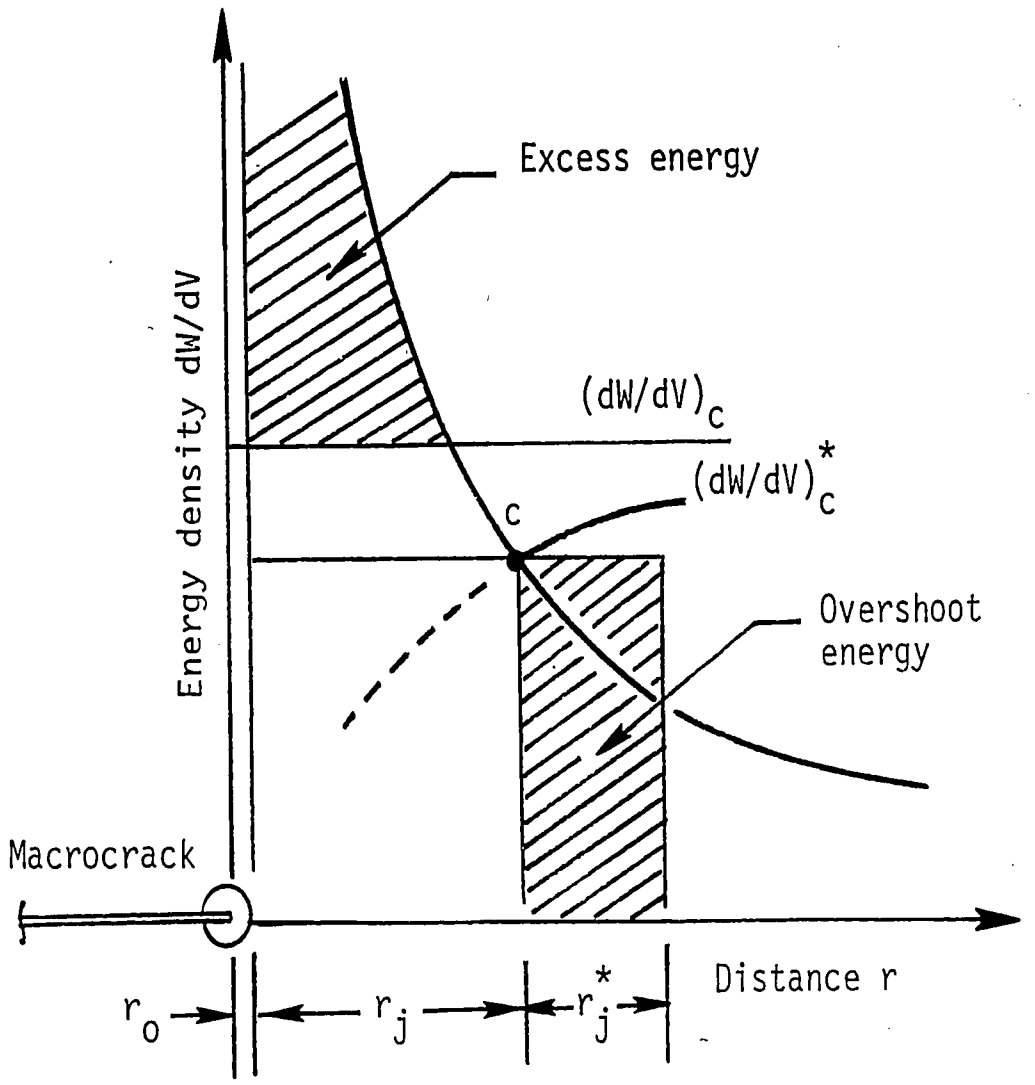

Figure 6.2. Crack growth and overshoot in the presence of plasticity.

ure 3.5 where c is the intersection of $(dW/dV)_c$ with the dW/dV curve. Because some of the available energy is dissipated in plastic deformation, there would be a corresponding decrease in the amount of overshoot. Consequently, crack growth rate with yielding is anticipated to be slower than the situation when all of the energy is available for driving the crack.

6.2 Overload with Plasticity

When plastic flow occurs ahead of the crack, the problem becomes nonlinear and the functional form of equation for the failure envelop

can no longer be derived analytically. Each critical state involving the relation of the equivalent uniaxial stress σ_c to the corresponding strain ε_c must be solved numerically using an elastic-plastic stress strain relation depending on the nonlinear behavior of the material under consideration.

For the angled crack configuration in Figure 4.1, the materials off to the side of the crack are extended beyond the elastic limit and they are known as the plastic enclaves, Figure 6.3. The direction of crack

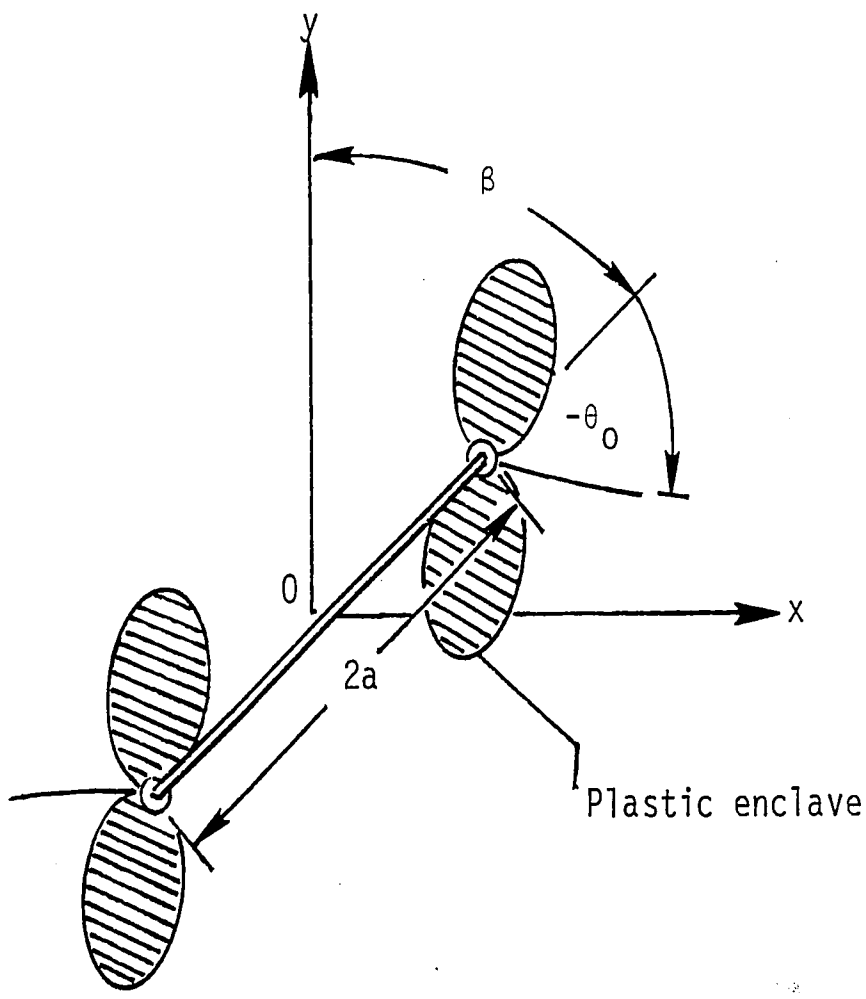

Figure 6.3. Plastic deformation around an angled crack.

initiation indicated by the angle $-\theta_o$ would now be affected not only by β but also by the extent of plastic deformation or the rate at which the applied load is increased in steps. For a fixed β, the ratio $A/\pi a^2$

could be varied to obtain the different critical states $(\sigma_c, \varepsilon_c)$ corresponding to dW/dV in a local element in the direction of $-\theta_o$ reaching $(dW/dV)_c$ being the area under the true stress and strain curve. Since plasticity would tend to reduce the specimen stiffness, the amount of overload would thus be reduced. This is illustrated in Figure 6.4

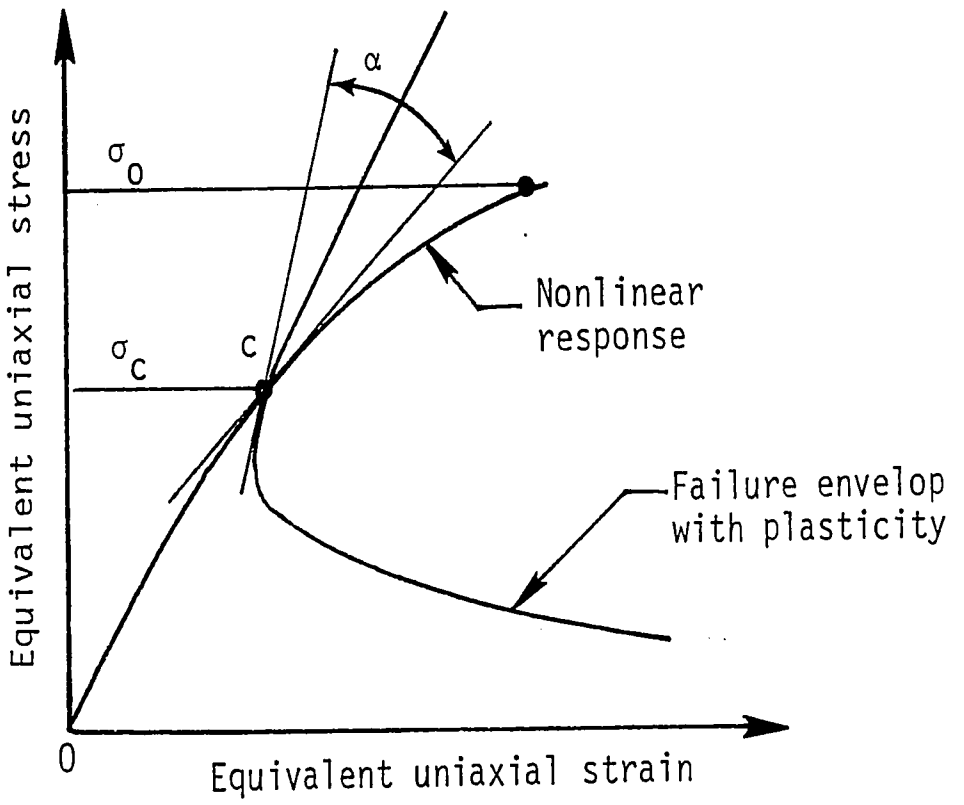

Figure 6.4. Overload stress for a specimen with nonlinear response.

where the nonlinear specimen response would intersect the failure envelop at c with a larger angle α as compared with the case of a linear response in Figure 5.15. The difference between σ_o and σ_c becomes smaller as it would be expected for specimen with ductile behavior. Such a study, however, is beyond the scope of this work.

VII. APPENDIX: FINITE ELEMENT METHOD

This approach allows for the analysis of a geometry for which the behavior of displacements, strains, etc., is not known to be determined by modelling it as a combination of many similar but irregularly divided elements. Mapping is used to transform these irregular subdivisions into unit elements, for which the behavior is well understood, in a mapped region. The theorem of minimum potential energy, based on the principle of virtual work, provides information on the displacement field and thus on strains and stresses. The displacements, strains, etc., can be mapped back into their original elements, thus providing a solution for a geometry not readily analyzed using analytical techniques. Since the procedure [39,40] is already well known, only a brief description of the numerical analysis will be given.

7.1 Interpolation Functions

For two dimensional geometries, it suffices to use the 12 nodes isoparametric element which is irregularly-shaped in the physical plane, Figure 7.1(a). The coordinates of the element in the mapped plane are $\xi = \pm 1$ and $\eta = \pm 1$ at the corner nodes. This is shown in Figure 7.1(b). The side nodes are evenly placed at 1/3 of the distance from the corners. A special feature of the transformation is that the same shape functions $N_i(\xi,\eta)$ $(i = 1,2,\ldots,12)$ can be used to relate the coordinates (x,y) and displacements (u_x,u_y) to their corresponding nodal values, say (x_i,y_i) and $[(u_x)_i,(u_y)_i]$. The following expressions, therefore, prevail:

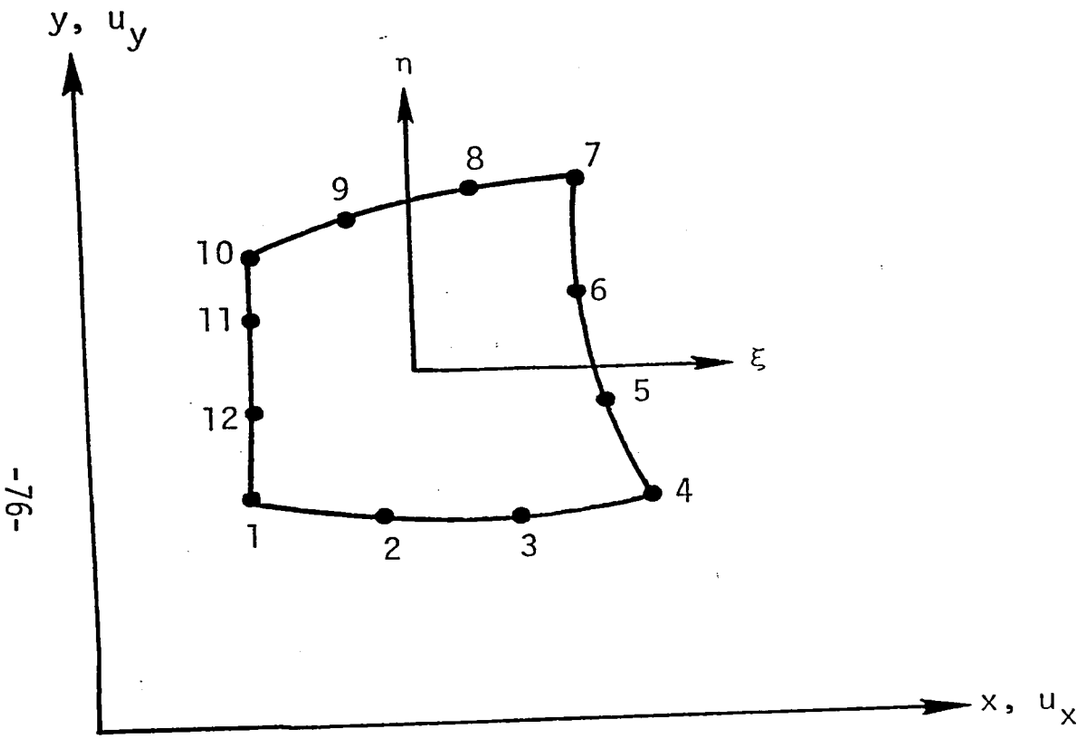

(a) Physical plane

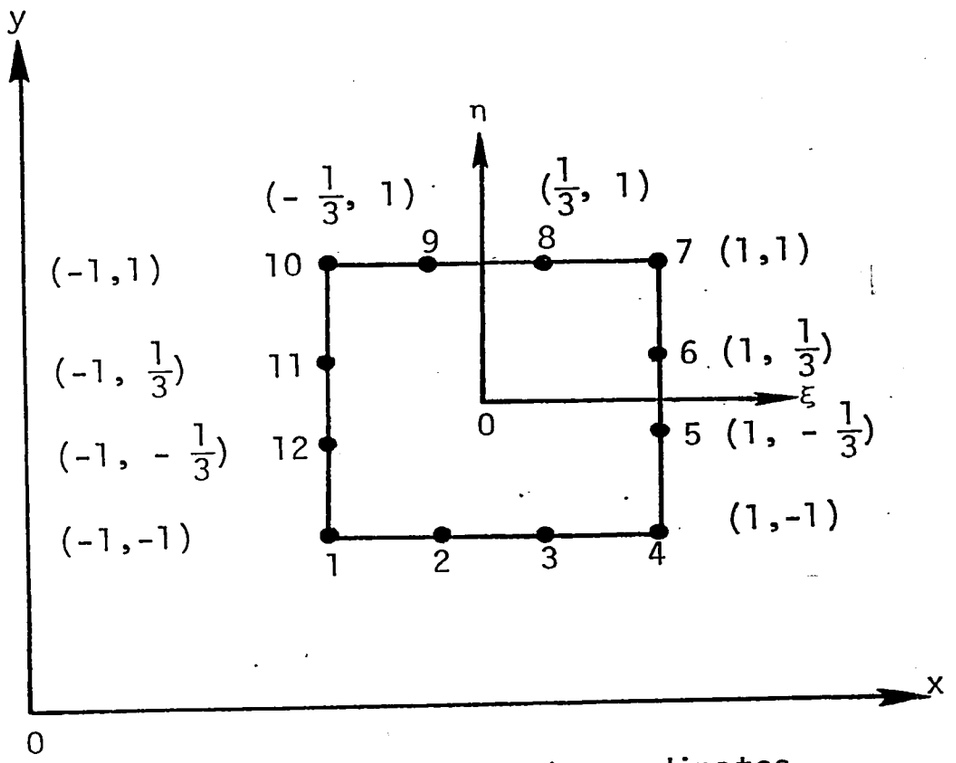

(b) Transformed coordinates

Figure 7.1. Coordinates of 12 node isoparametric element in physical and transformed plane.

$$x = \sum_{i=1}^{12} N_i(\xi,\eta)x_i, \qquad y = \sum_{i=1}^{12} N_i(\xi,\eta)y_i \tag{7.1}$$

The same applies to the displacements:

$$u_x = \sum_{i=1}^{12} N_i(\xi,\eta)(u_x)_i, \qquad u_y = \sum_{i=1}^{12} N_i(\xi,\eta)(u_y)_i \tag{7.2}$$

The shape functions $N_i(\xi,\eta)$ $(i = 1,2,\ldots,12)$ are given by

$$N_1 = \frac{1}{32}(1-\eta)(1-\xi)[9(\xi^2+\eta^2)-10]$$

$$N_2 = \frac{9}{32}(1-\eta)(1-\xi^2)(1-3\xi)$$

$$N_3 = \frac{9}{32}(1-\eta)(1-\xi^2)(1+3\xi)$$

$$N_4 = \frac{1}{32}(1-\eta)(1+\xi)[9(\xi^2+\eta^2)-10]$$

$$N_5 = \frac{9}{32}(1+\xi)(1-\eta^2)(1-3\eta)$$

$$N_6 = \frac{9}{32}(1+\xi)(1-\eta^2)(1+3\eta)$$

$$N_7 = \frac{1}{32}(1+\xi)(1+\eta)[9(\xi^2+\eta^2)-10]$$

$$N_8 = \frac{9}{32}(1+\eta)(1-\xi^2)(1+3\xi)$$

$$N_9 = \frac{9}{32}(1+\eta)(1-\xi^2)(1-3\xi)$$

$$N_{10} = \frac{1}{32}(1+\eta)(1-\xi)[9(\xi^2+\eta^2)-10]$$

$$N_{11} = \frac{9}{32}(1-\xi)(1-\eta^2)(1+3\eta)$$

$$N_{12} = \frac{9}{32}(1-\xi)(1-\eta^2)(1-3\eta) \tag{7.3}$$

7.2 Strains and Stresses

Once the displacements are known, the strain components may be obtained from the displacement gradients:

$$\underset{\sim}{\{\varepsilon\}} = \begin{bmatrix} \varepsilon_x \\ \varepsilon_y \\ \gamma_{xy} \end{bmatrix} = \begin{bmatrix} \dfrac{\partial u_x}{\partial x} \\ \dfrac{\partial u_y}{\partial y} \\ \dfrac{\partial u_x}{\partial y} + \dfrac{\partial u_y}{\partial x} \end{bmatrix} \tag{7.4}$$

Substituting equations (7.2) into equations (7.4) and writing the result in matrix form, it is found that

$$\underset{\sim}{\{\varepsilon\}} = [B]\underset{\sim}{\{u\}} \tag{7.5}$$

in which

$$[B_i] = \begin{bmatrix} \frac{\partial N_i}{\partial x}, & 0 \\ 0 & , \frac{\partial N_i}{\partial y} \\ \frac{\partial N_i}{\partial y}, & \frac{\partial N_i}{\partial x} \end{bmatrix} \tag{7.6}$$

In equation (7.5), $\{u\}$ is the displacement vector defined as

$$\{u\} = \begin{bmatrix} (u_x)_i \\ \\ (u_y)_i \end{bmatrix} \tag{7.7}$$

For a linear elastic, isotropic and homogeneous solid under plane strain, the material matrix

$$[D] = \frac{E}{(1+\nu)(1-2\nu)} \begin{bmatrix} 1-\nu, & \nu & , 0 \\ \nu & , 1-\nu, & 0 \\ 0 & , 0 & , \frac{1-2\nu}{2} \end{bmatrix} \tag{7.8}$$

can be used to relate the stress $\{\sigma\}$ and strain $\{\varepsilon\}$ as follows:

$$\{\sigma\} = [D]\{\varepsilon\} \tag{7.9}$$

7.3 Equation of Motion

The finite element method relies on application of the theorem of minimum potential energy that is based on the principle of virtual

work. It provides a good approximation for the displacement field at the expense of the stresses as in contrast to the theorem of minimum complimentary energy that places emphasis on the variation of the stresses. This difference in variational calculus should be kept in mind when interpreting the end results obtained from finite element in addition to the other approximations mentioned earlier.

Application of the standard finite element procedure [39,40], the governing equation of motion can be written in the form

$$[M]\{\ddot{\underset{\sim}{u}}\} + [K]\{\underset{\sim}{u}\} = \{\underset{\sim}{F}\} \tag{7.10}$$

with [M] being the mass matrix. The equivalent load matrix $\{\underset{\sim}{F}\}$ is

$$\{\underset{\sim}{F}\} = \int_{\Lambda} [N_i]^T \{\underset{\sim}{F}^b\} dV + \int_{\Sigma} [N_i]^T \{\underset{\sim}{F}^s\} dA \tag{7.11}$$

Here, $\underset{\sim}{F}^b$ and $\underset{\sim}{F}^s$ are, respectively, the body and surface force vector. The stiffness matrix [K] in equation (7.10) is given by

$$[K] = \iint [B]^T [D][B] h dx dy \tag{7.12}$$

where h is the thickness dimension of the plane body. Computation of [K] is carried out in terms of the variables ξ and η such that equation (7.12) is expressed as

$$[K] = \int_{-1}^{1} \int_{-1}^{1} Q(\xi,\eta) d\xi d\eta \tag{7.13}$$

in which

$$Q(\xi,\eta) = [B]^T[D][B]h \det [J] \tag{7.14}$$

Use is made of the Jacobian

$$[J] = \begin{bmatrix} \frac{\partial x}{\partial \xi}, & \frac{\partial y}{\partial \xi} \\ \\ \frac{\partial x}{\partial \eta} & \frac{\partial y}{\partial \eta} \end{bmatrix} \tag{7.15}$$

whose inverse is

$$[J]^{-1} = \frac{1}{\frac{\partial x}{\partial \xi}\frac{\partial y}{\partial \eta} - \frac{\partial x}{\partial \eta}\frac{\partial y}{\partial \xi}} \begin{bmatrix} \frac{\partial y}{\partial \eta}, & -\frac{\partial y}{\partial \xi} \\ \\ -\frac{\partial x}{\partial \eta}, & \frac{\partial x}{\partial \xi} \end{bmatrix} \tag{7.16}$$

for transforming dA in terms (x,y) to (ξ,η) as

$$dxdy = \det [J] d\xi d\eta \tag{7.17}$$

In view of equations (7.1) and (7.2), equation (7.15) may also be written as

$$[J] = \begin{bmatrix} \sum_{i=1}^{12} \frac{\partial N_i}{\partial \xi} x_i, & \sum_{i=1}^{12} \frac{\partial N_i}{\partial \xi} y_i \\ \\ \sum_{i=1}^{12} \frac{\partial N_i}{\partial \eta} x_i, & \sum_{i=1}^{12} \frac{\partial N_i}{\partial \eta} y_i \end{bmatrix} \tag{7.18}$$

Change of independent variables can be made by means of

$$\begin{bmatrix} \frac{\partial N_i}{\partial \xi} \\ \\ \frac{\partial N_i}{\partial \eta} \end{bmatrix} = [J] \begin{bmatrix} \frac{\partial N_i}{\partial x} \\ \\ \frac{\partial N_i}{\partial y} \end{bmatrix} \tag{7.19}$$

The inverse of equation (7.19) is

$$\begin{bmatrix} \frac{\partial N_i}{\partial x} \\ \\ \frac{\partial N_i}{\partial y} \end{bmatrix} = [J]^{-1} \begin{bmatrix} \frac{\partial N_i}{\partial \xi} \\ \\ \frac{\partial N_i}{\partial \eta} \end{bmatrix} \tag{7.20}$$

The Gauss-Legendre quadrature scheme is applied to compute [K] numerically. This procedure assumes that

$$\int_{-1}^{1} \int_{-1}^{1} Q(\xi,\eta)d\xi d\eta = \sum_{i=1}^{4} \sum_{i=1}^{4} H_i H_j Q(\xi_j,n_j) \tag{7.21}$$

Sixteen (16) Gaussian points can thus be embedded in each of the twelve (12) node isoparametric element such that

$$\xi_2 = -\xi_3 = 0.339981043584856$$

$$\xi_1 = -\xi_4 = 0.861136311594053$$

$$\eta_2 = -\eta_3 = 0.339981043584856 \qquad (7.22)$$

$$\eta_1 = -\eta_4 = 0.861136311594053$$

The values H_j (j = 1,2,...,4) in equation (7.21) are

$$H_1 = H_4 = 0.347854845137454 \qquad (7.23)$$

$$H_2 = H_3 = 0.652145154862546$$

As the numerical values of $\{u\}$ are obtained from equation (7.10), the quantities of interest such as $\{\varepsilon\}$ follows from equation (7.5) while $\{\sigma\}$ follows subsequently from equation (7.9).

7.4 Shifting of Side Nodes

The way with which the displacement gradients behave in the vicinity of a crack tip can be altered by adjusting the spacing of the neighboring side nodes. For the case of the eight (8) node isoparametric finite element, the midside nodes may be shifted to the quarter point nearest the crack tip to yield the $1/\sqrt{r}$ singular behavior of the

displacement gradient [28]. The same can be achieved for the twelve (12) node isoparametric element by shifting the intermediate nodes to the 1/9 and 4/9 positions nearest the crack tip [29] as discussed in relation to Figure 2.3 in Section 2.1.

VIII. APPENDIX: ENERGY DENSITY CONTOURS AND VARIATIONS FOR DIFFERENT CRACK GROWTH SEGMENTS

Enclosed in this section are the energy density contours around the crack tip region for each crack growth step as β is increased in 15° increments from 15° to 75°. The corresponding variations of dW/dV with the distance along the prospective path of crack growth are also given. These data are sufficient for determining r_j and r_j^o and r_j^* since r_o is fixed. Their values can be found in Table 5.1.

8.1 Crack Angle β = 15°

For an originally straight crack of length 2a tilted at β = 15° with the applied stress, eight (8) steps were taken to establish the crack profile in Figure 5.1(a). With reference to Table 5.1 and Figure 8.1, the first step crack growth is r_1^* = 0.097 cm. The second growth step, r_2^* = 0.140 cm, can be obtained from the results in Figure 8.2 where the predicted crack segment coincide with the element boundary. Deviating slightly away from the element boundary is the third crack segment r_3^* = 0.236 cm in Figure 8.3. That is, the crack did not extend straight ahead. From the fourth to the sixth step corresponding to the data in Figures 8.4 to 8.6 inclusive, the crack grew nearly straight ahead where its path and the element boundary cannot be easily distinguished. The specimen boundary effect comes into play at the seventh and eighth crack growth steps with r_7^* = 0.770 cm and r_8^* = 1.278 cm, respectively, where the crack again starts to deviate from growing in a straight line. Refer to the data in Figures 8.7 and 8.8.

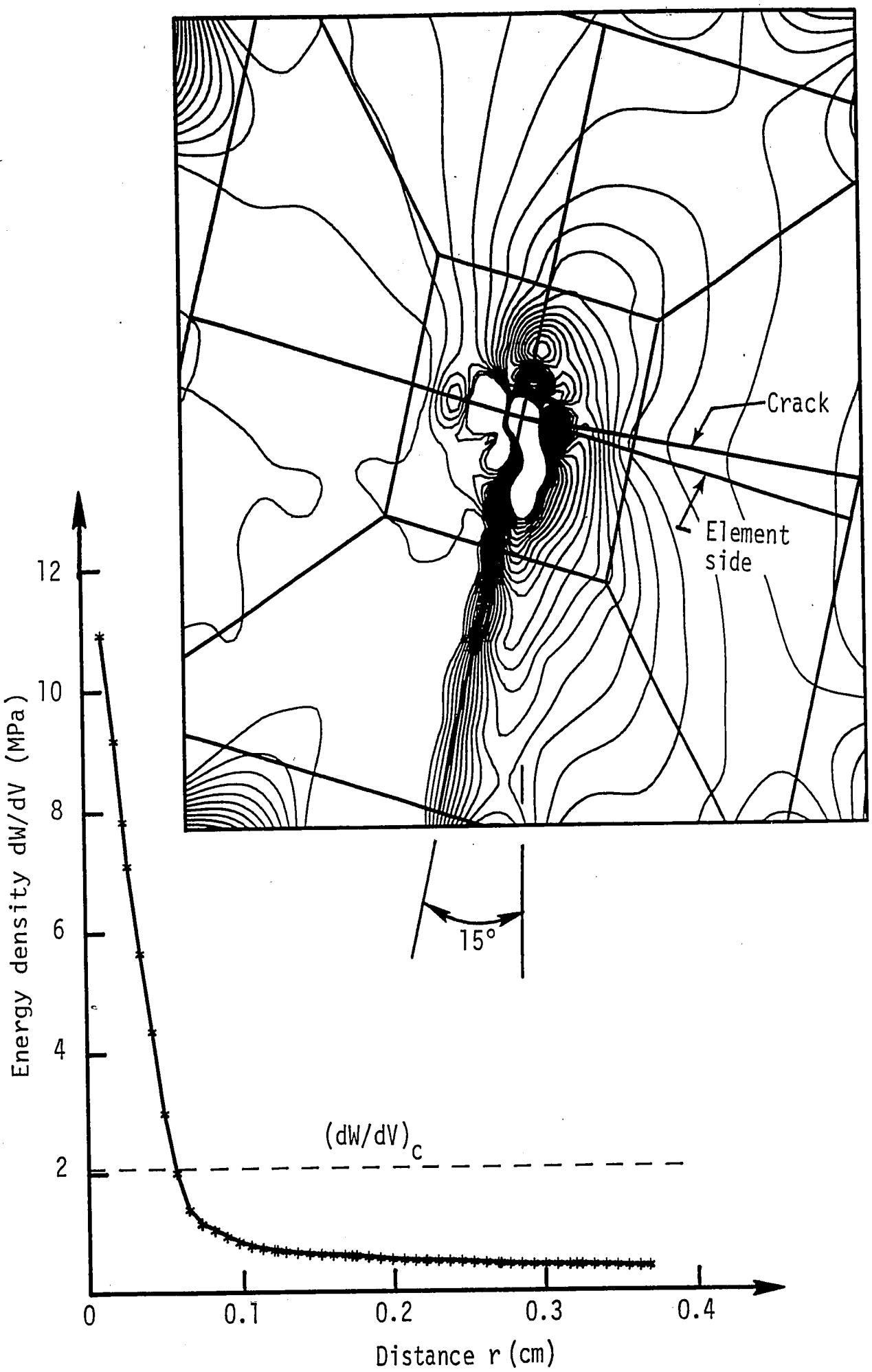

Figure 8.1. Variations of energy density with distance for first step crack growth with $\beta = 15°$.

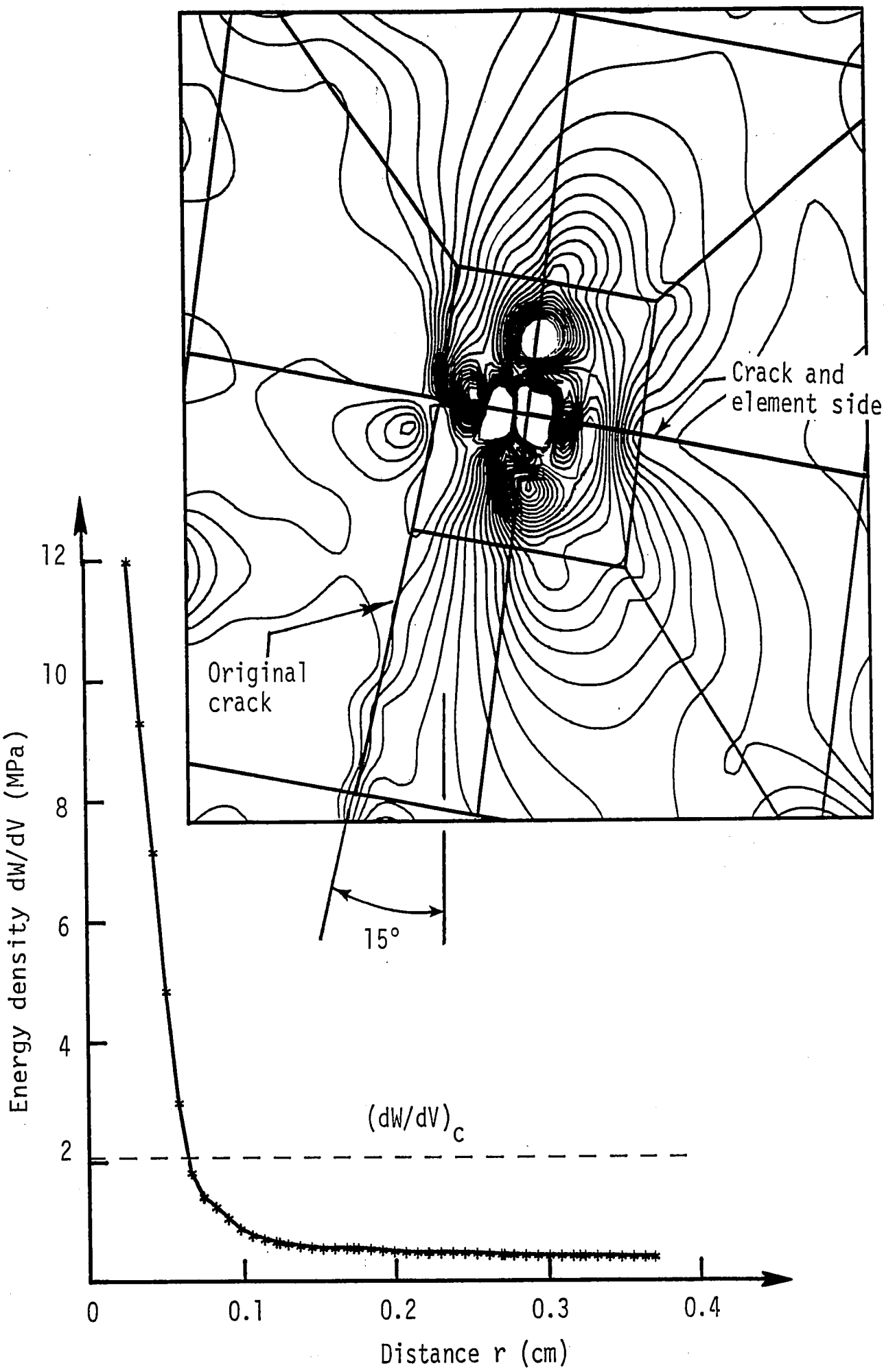

Figure 8.2. Variations of energy density with distance for second step crack growth with $\beta = 15°$.

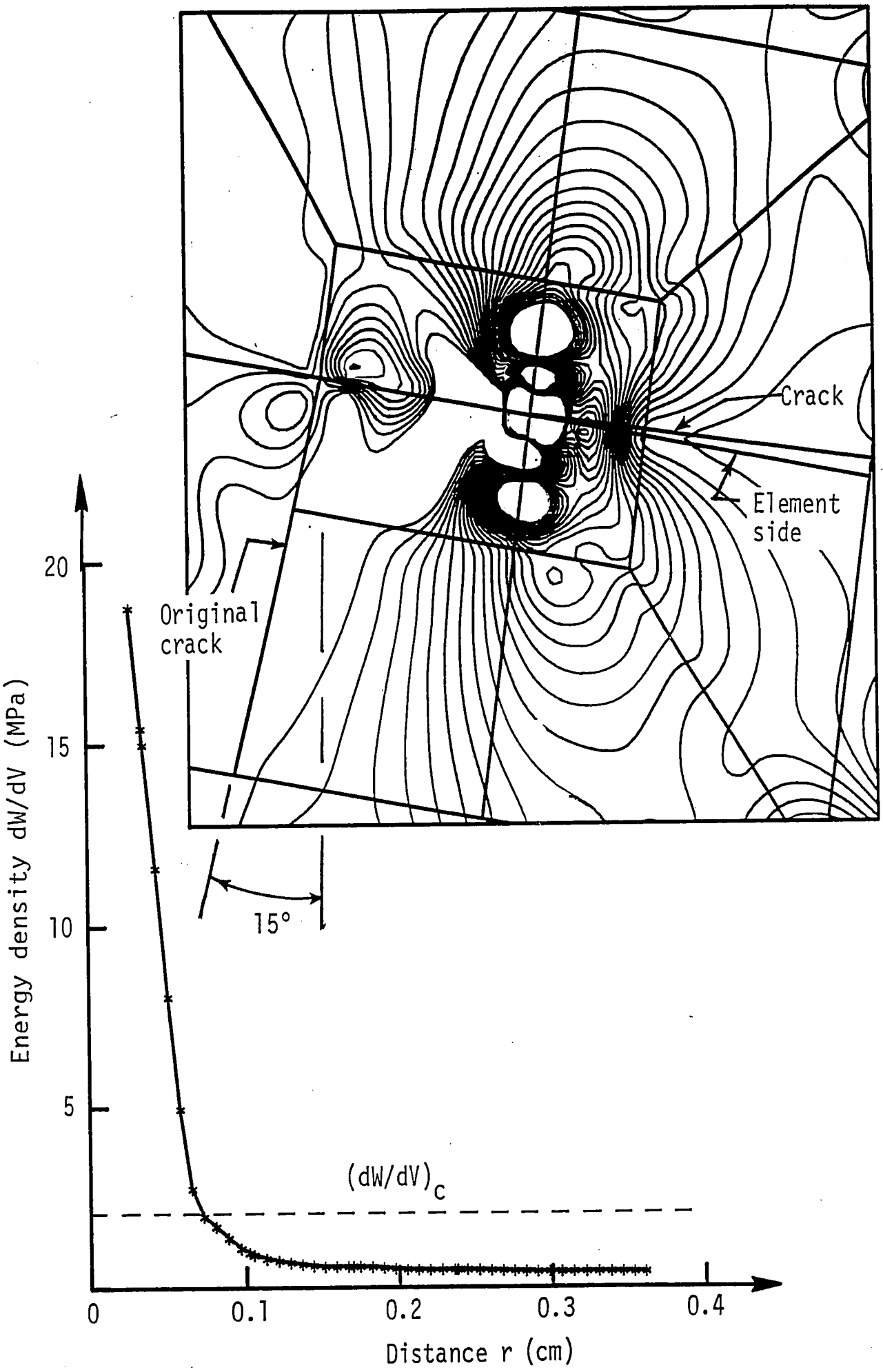

Figure 8.3. Variations of energy density with distance for third step crack growth with $\beta = 15°$.

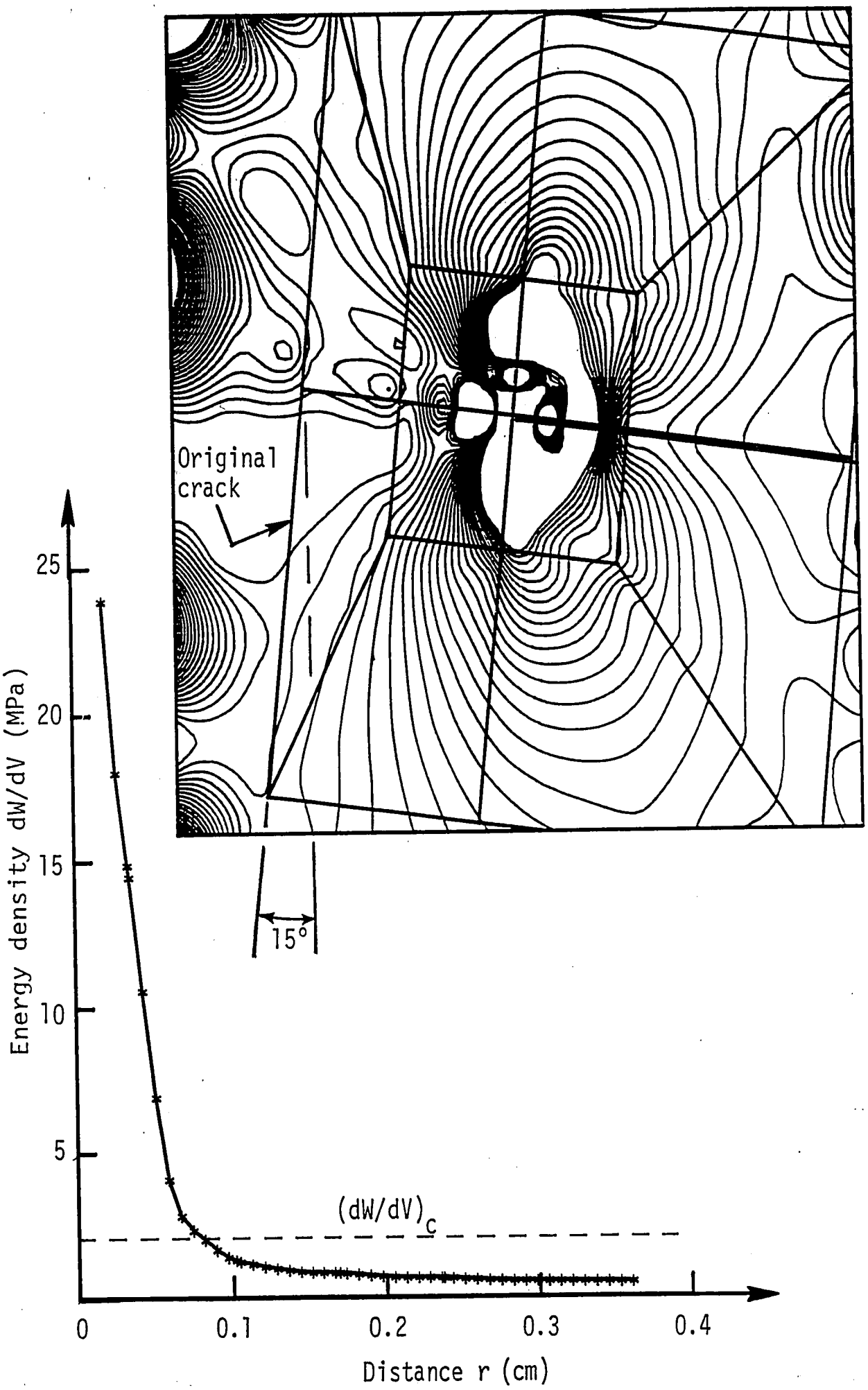

Figure 8.4. Variations of energy density with distance for fourth step crack growth with $\beta = 15°$.

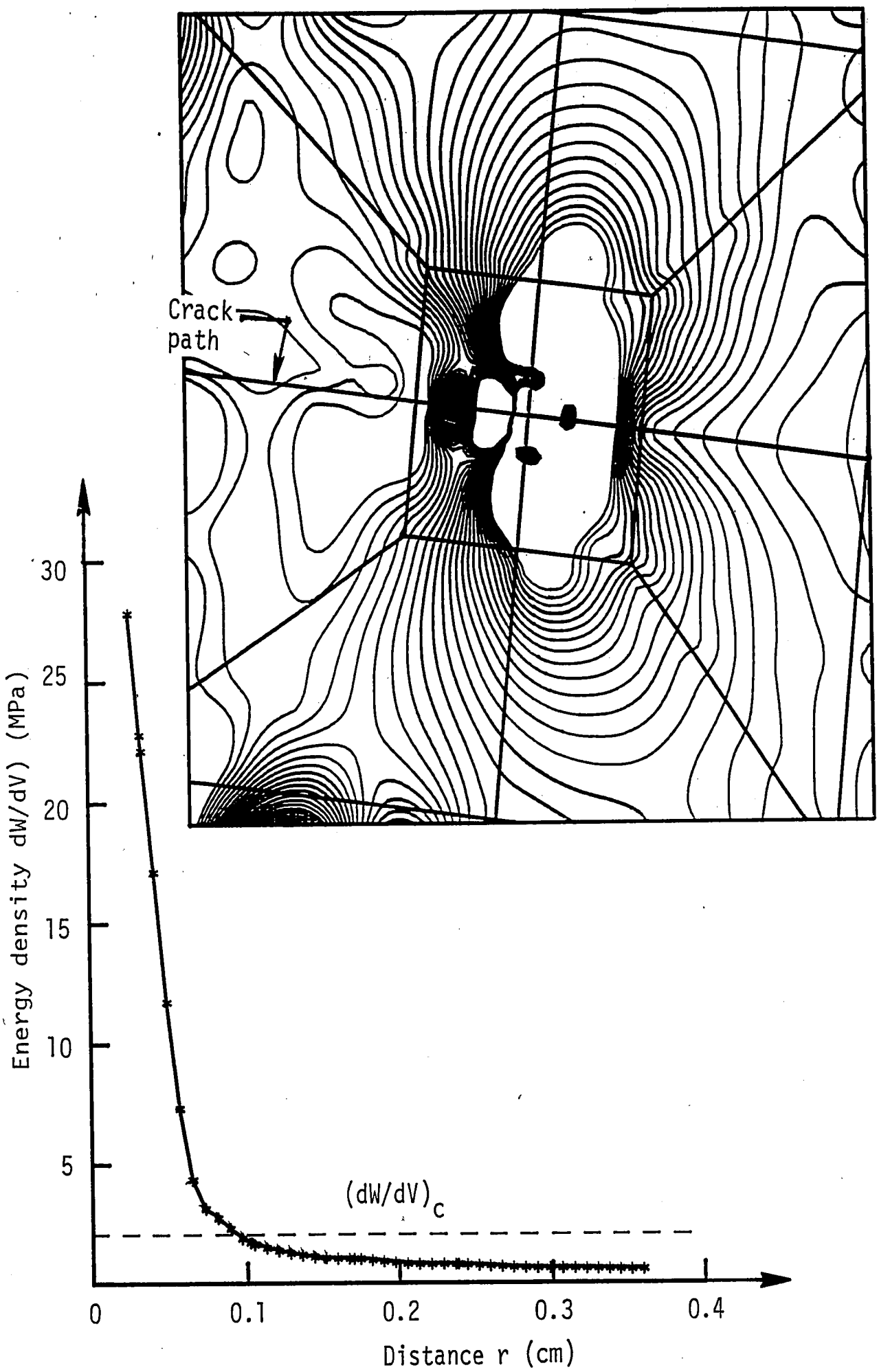

Figure 8.5. Variations of energy density with distance for fifth step crack growth with $\beta = 15°$.

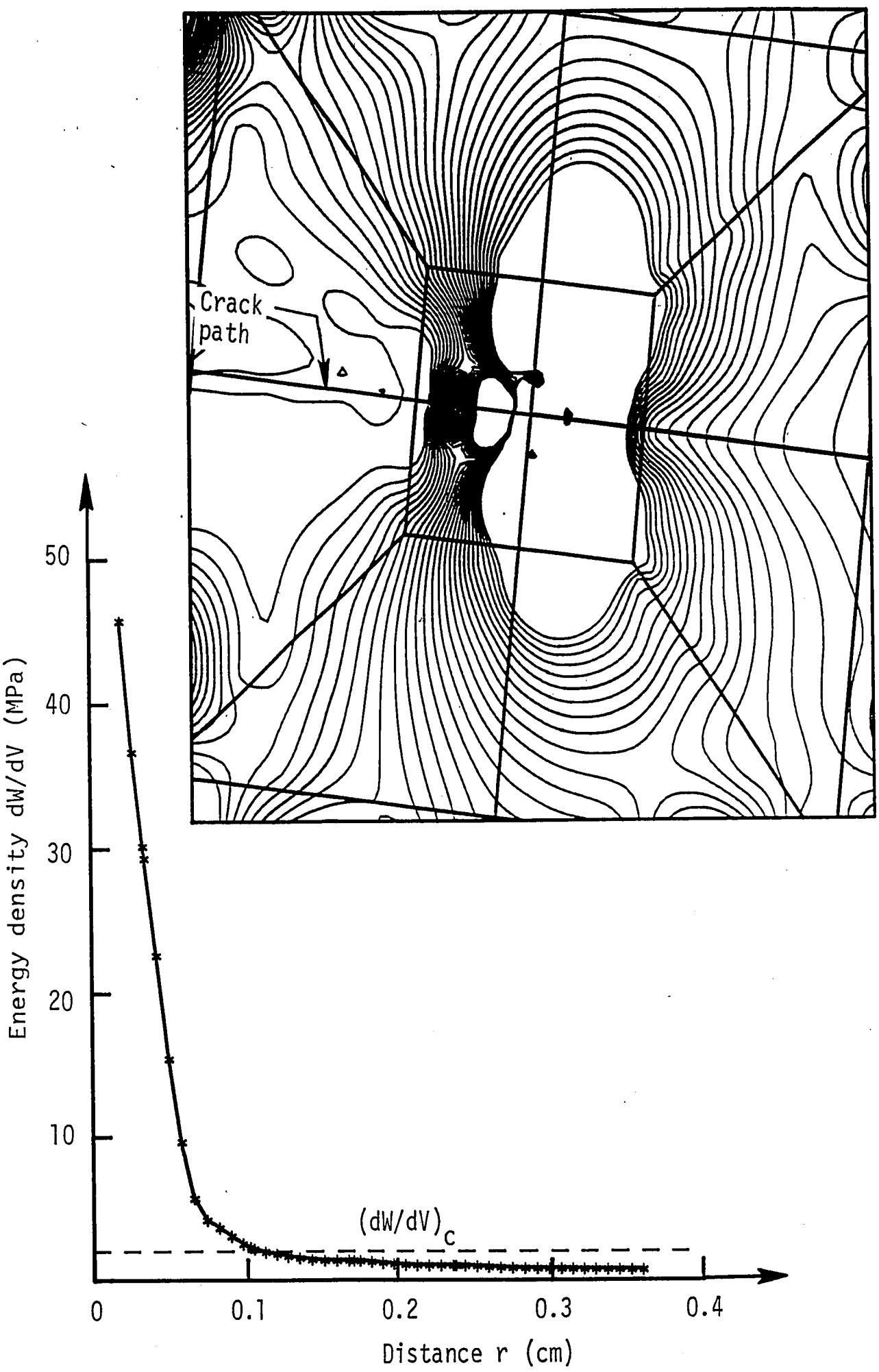

Figure 8.6. Variations of energy density with distance for sixth step crack growth with $\beta = 15°$.

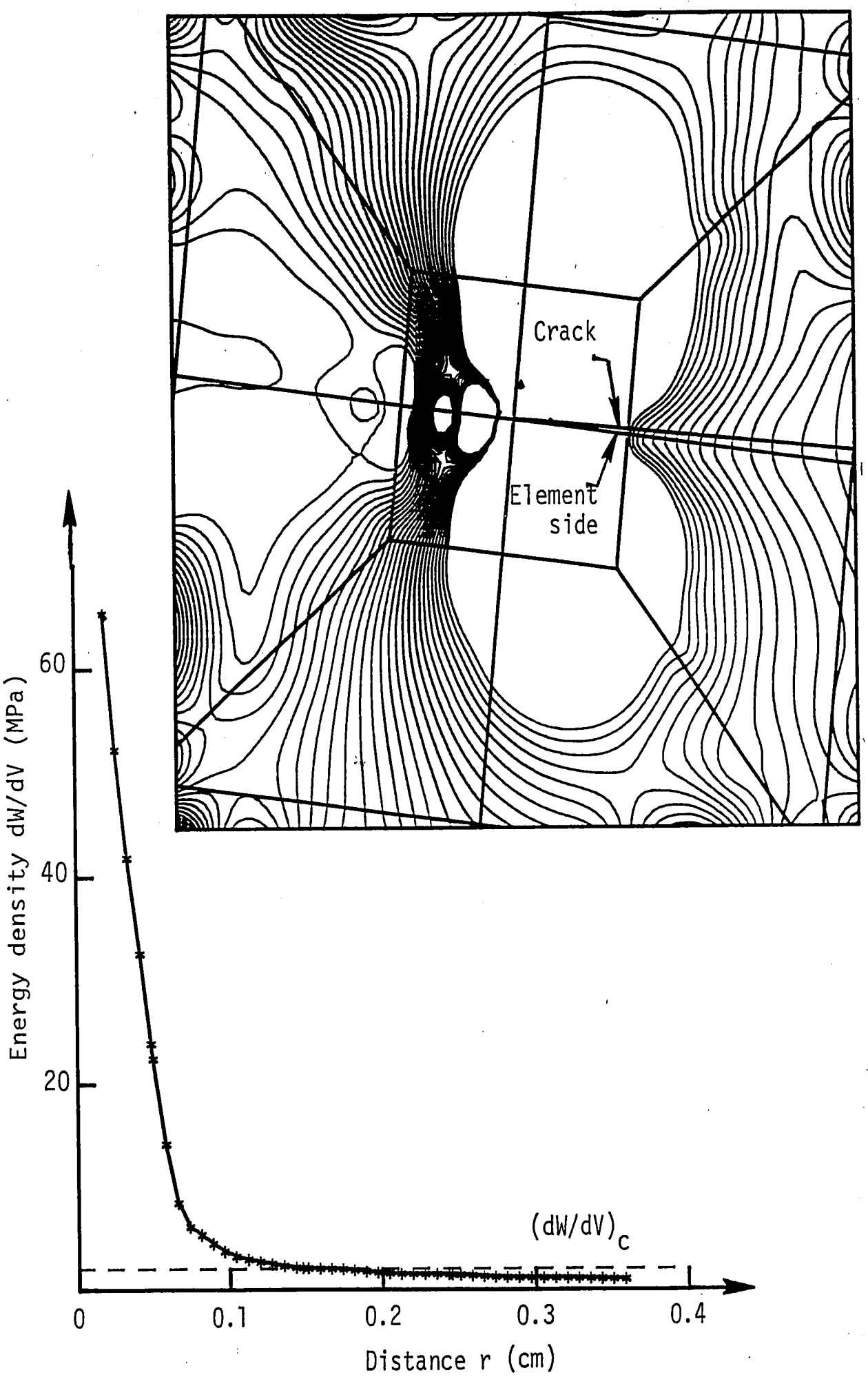

Figure 8.7. Variations of energy density with distance for seventh step crack growth with $\beta = 15°$.

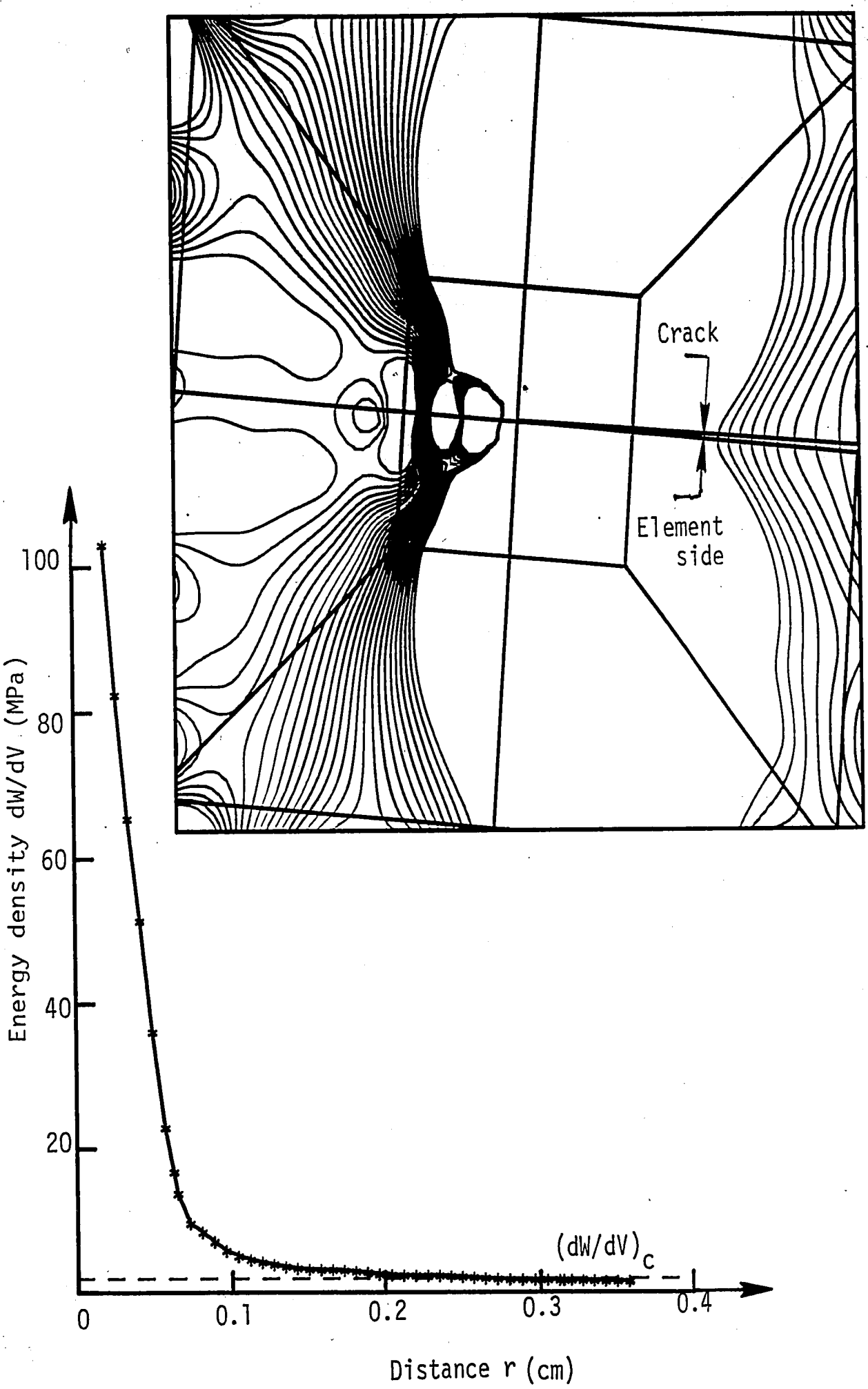

Figure 8.8. Variations of energy density with distance for eighth step crack growth with $\beta = 15°$.

8.2 Crack Angle $\beta = 30°$

Let the crack angle β be increased 30° as shown in Figure 5.1(b). The finite element grid pattern is thus remeshed accordingly. A plot of dW/dV versus r is made from which r_j and r_j^o can be found as before. Concentration of the dW/dV contours around the crack tip is shown in Figure 8.9. The first step of crack growth $r_1^* = 0.257$ cm is assumed to coincide with the path of $(dW/dV)_{min}$ and it deviated significantly from the element side. This difference is much smaller for the second crack growth increment $r_2^* = 0.397$ cm and can be seen from Figure 8.10. Following the same method of solution, r_j^* for the third, fourth and fifth crack growth segments are found, respectively, from the data in Figures 8.11, 8.12 and 8.13. The entire crack trajectory can be found in Figure 5.1(b).

8.3 Crack Angle $\beta = 45°$

Figure 8.14 gives the dW/dV contours for a crack tilted at $\beta = 45°$ with the load axis. The path of $(dW/dV)_{min}$ is located and the variations of dW/dV in this direction is plotted to determine the crack growth segment with overshoot. This leads to $r_1^* = 0.419$ cm as shown in Table 5.1 for $\beta = 45°$. The same procedure is repeated for the second, third and fourth crack growth steps from the information in Figures 8.15, 8.16 and 8.17, respectively. Refer to Figure 5.1(c) for a schematic of the entire crack profile.

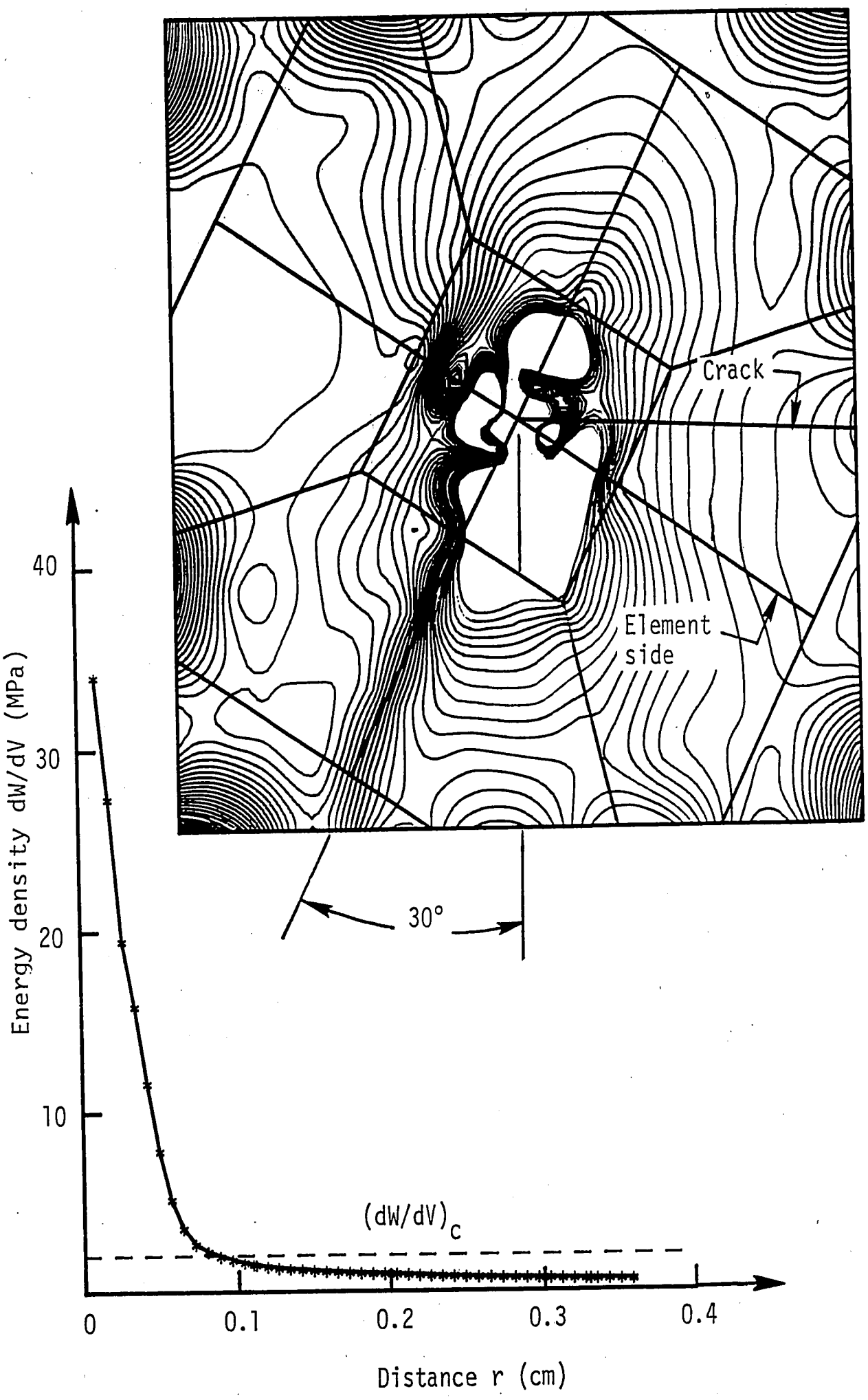

Figure 8.9. Variations of energy density with distance for first step crack growth with $\beta = 30°$.

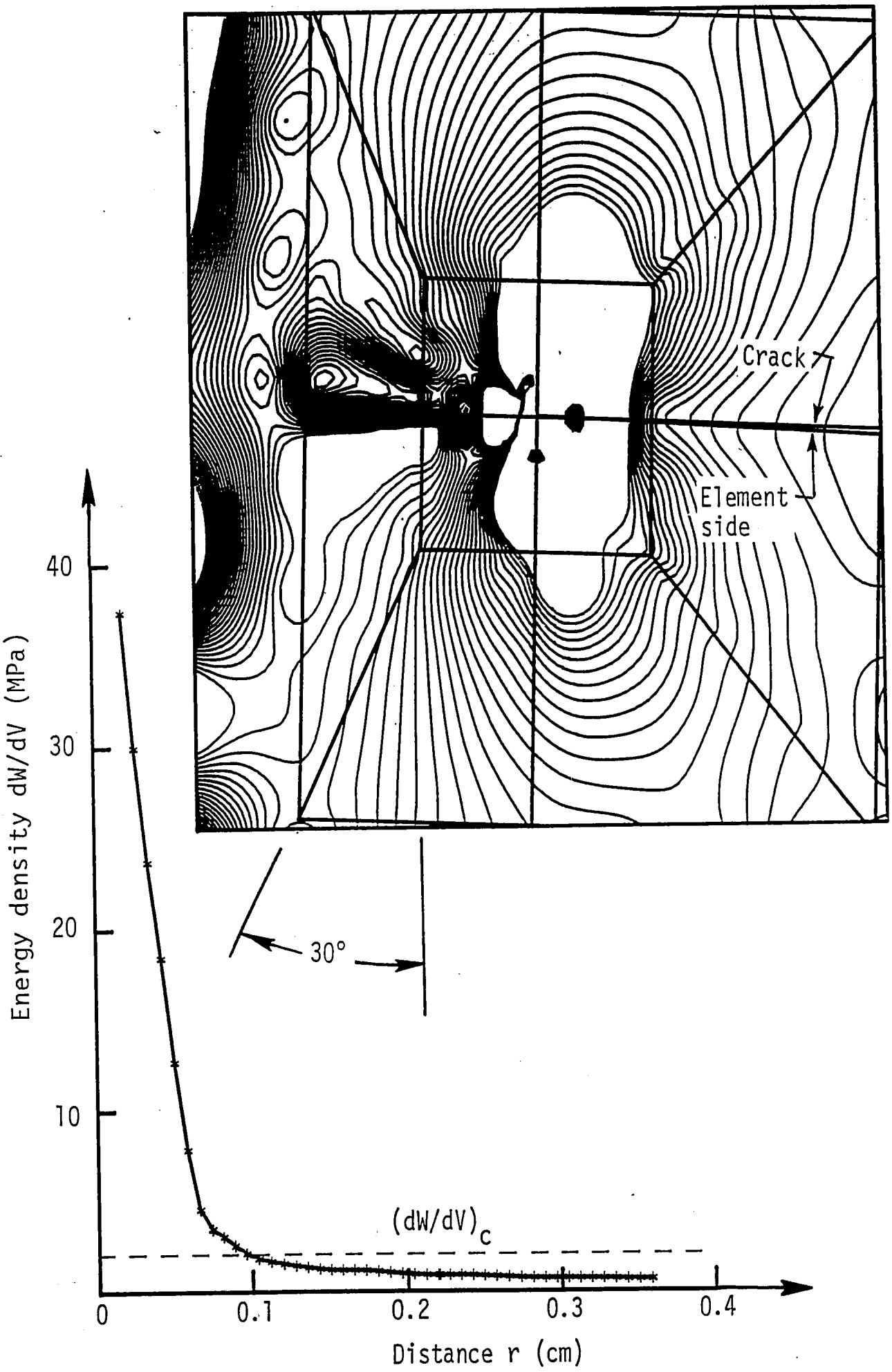

Figure 8.10. Variations of energy density with distance for second step crack growth with $\beta = 30°$.

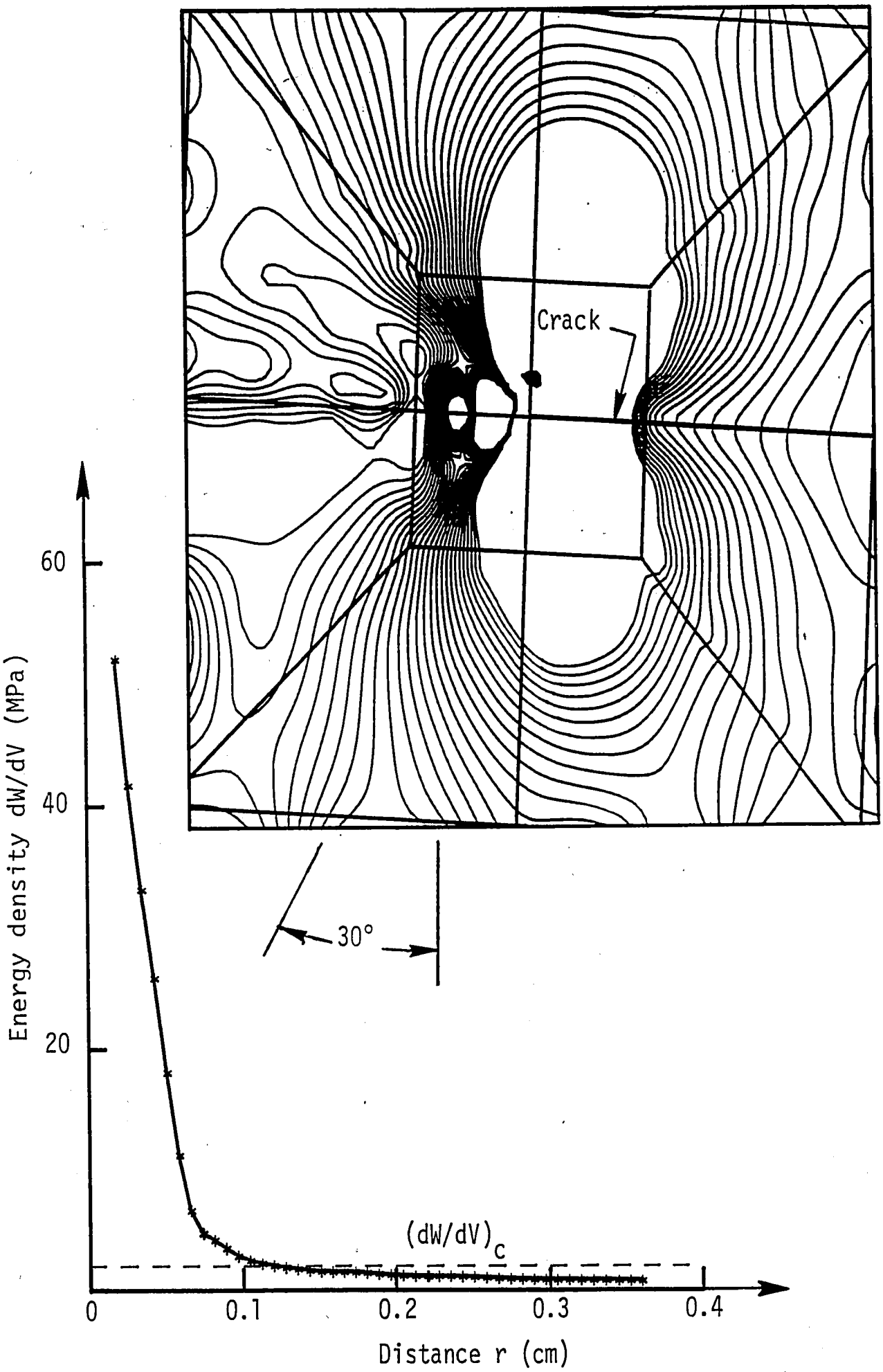

Figure 8.11. Variations of energy density with distance for third step crack growth with $\beta = 30°$.

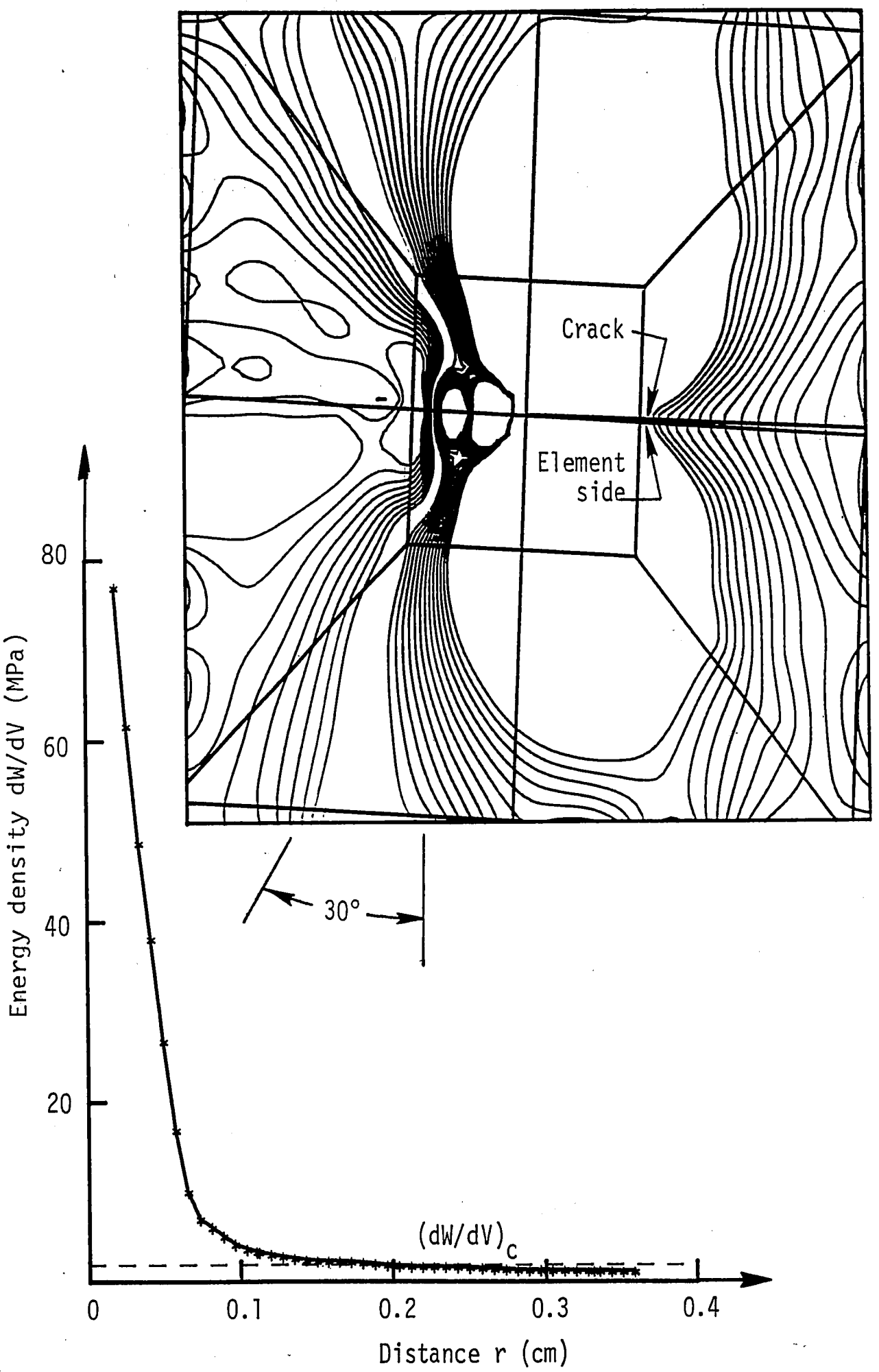

Figure 8.12. Variations of energy density with distance for fourth step crack growth with $\beta = 30°$.

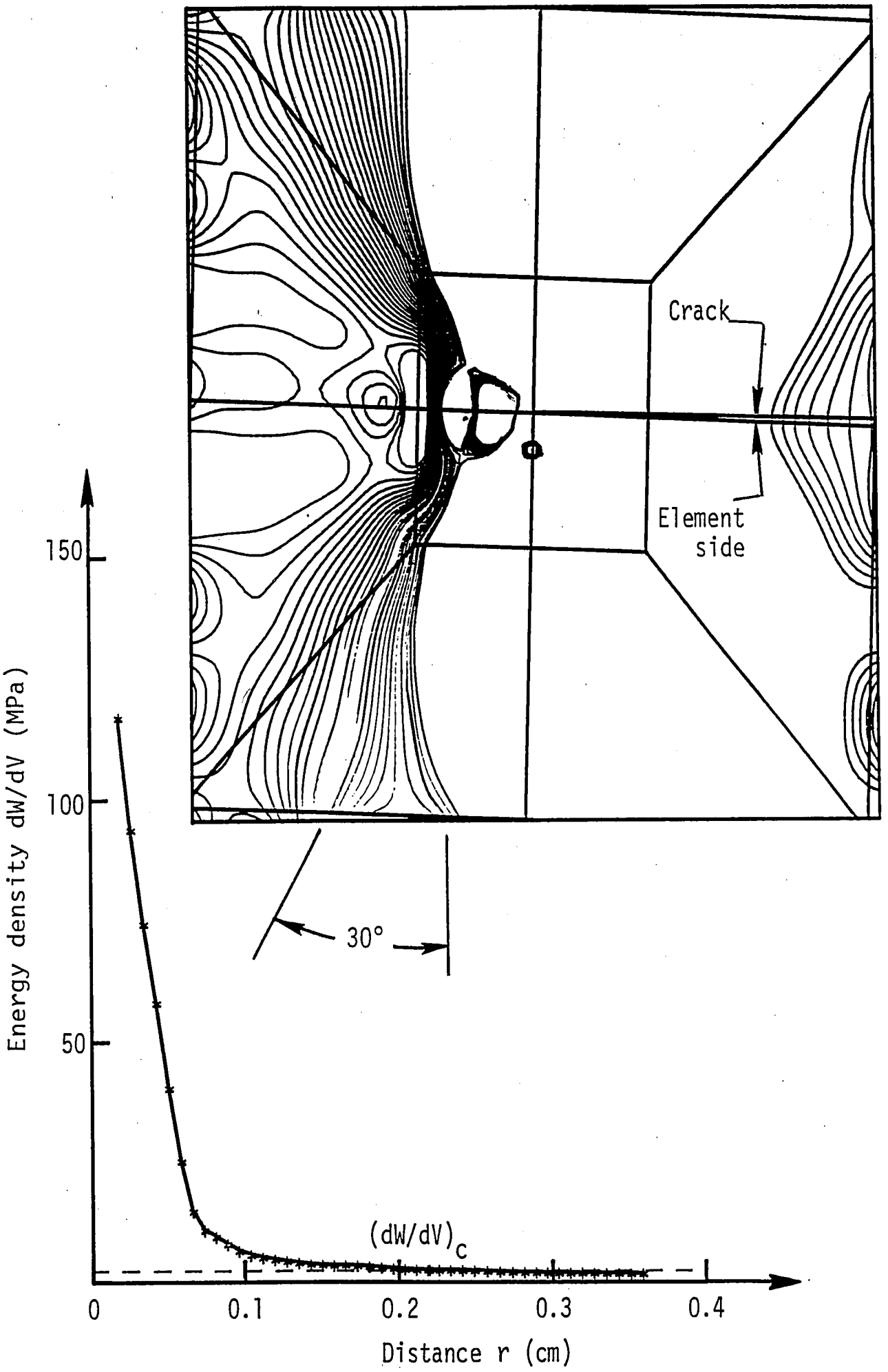

Figure 8.13. Variations of energy density with distance for fifth step crack growth with $\beta = 30°$.

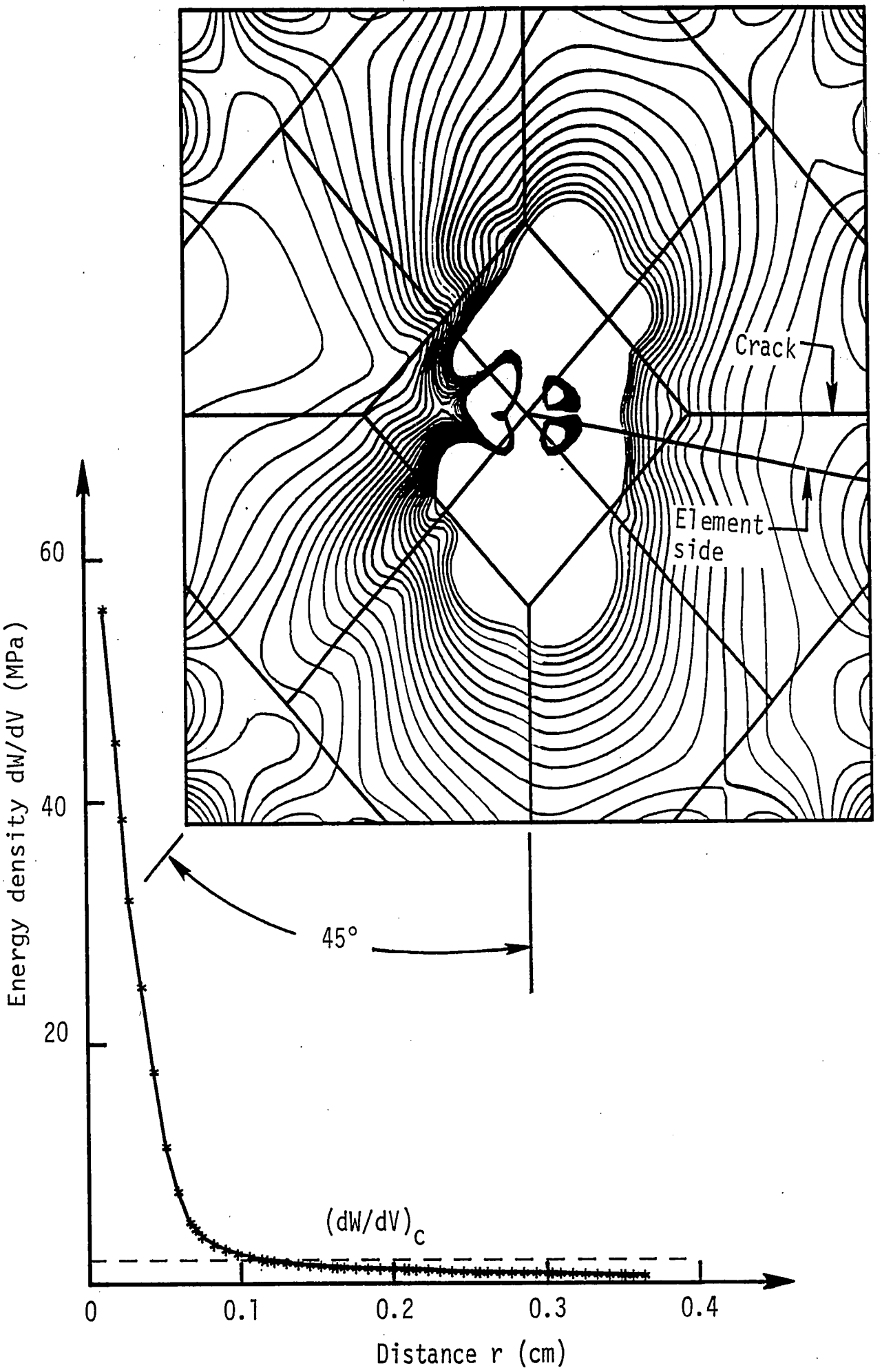

Figure 8.14. Variations of energy density with distance for first step crack growth with $\beta = 45°$.

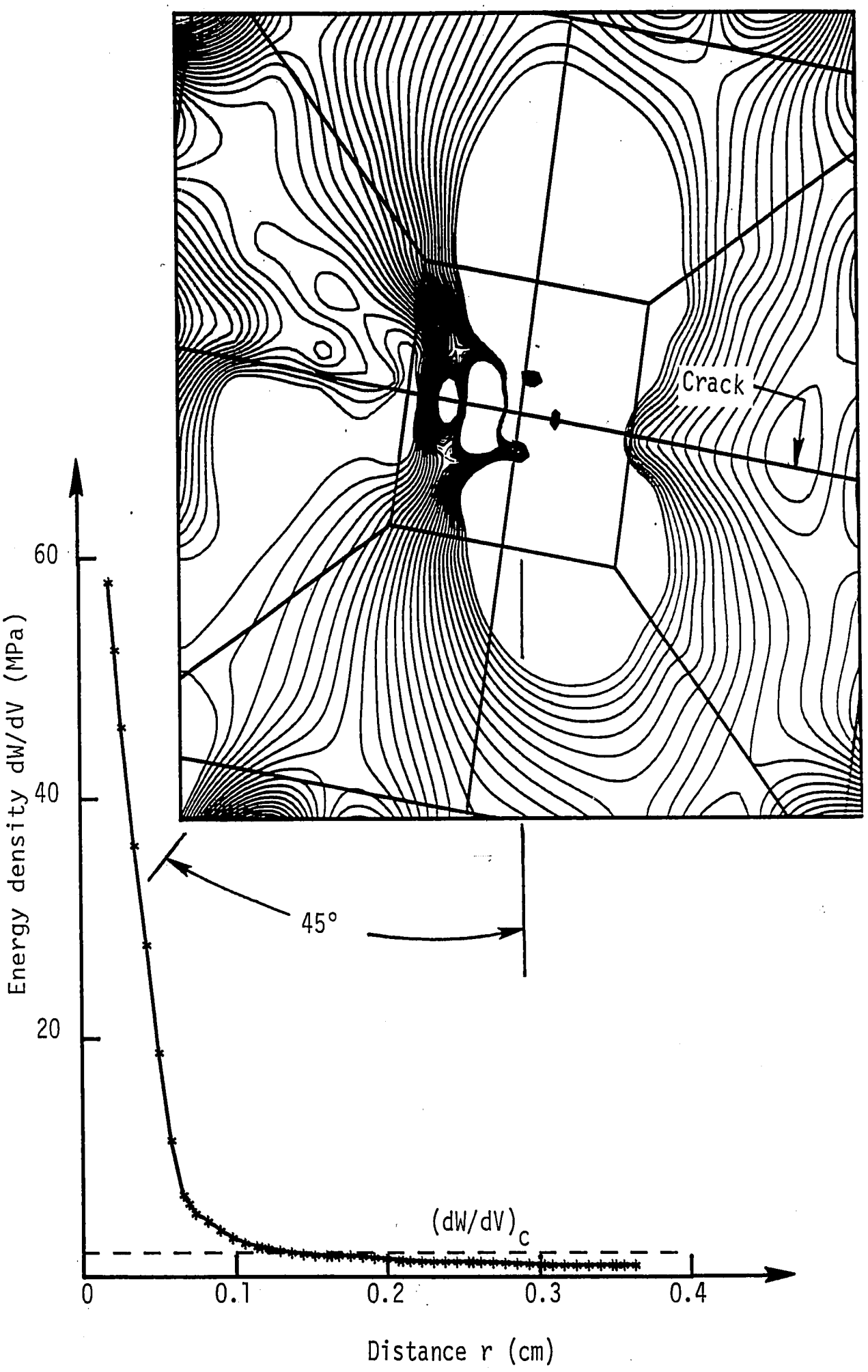

Figure 8.15. Variations of energy density with distance for second step crack growth with $\beta = 45°$.

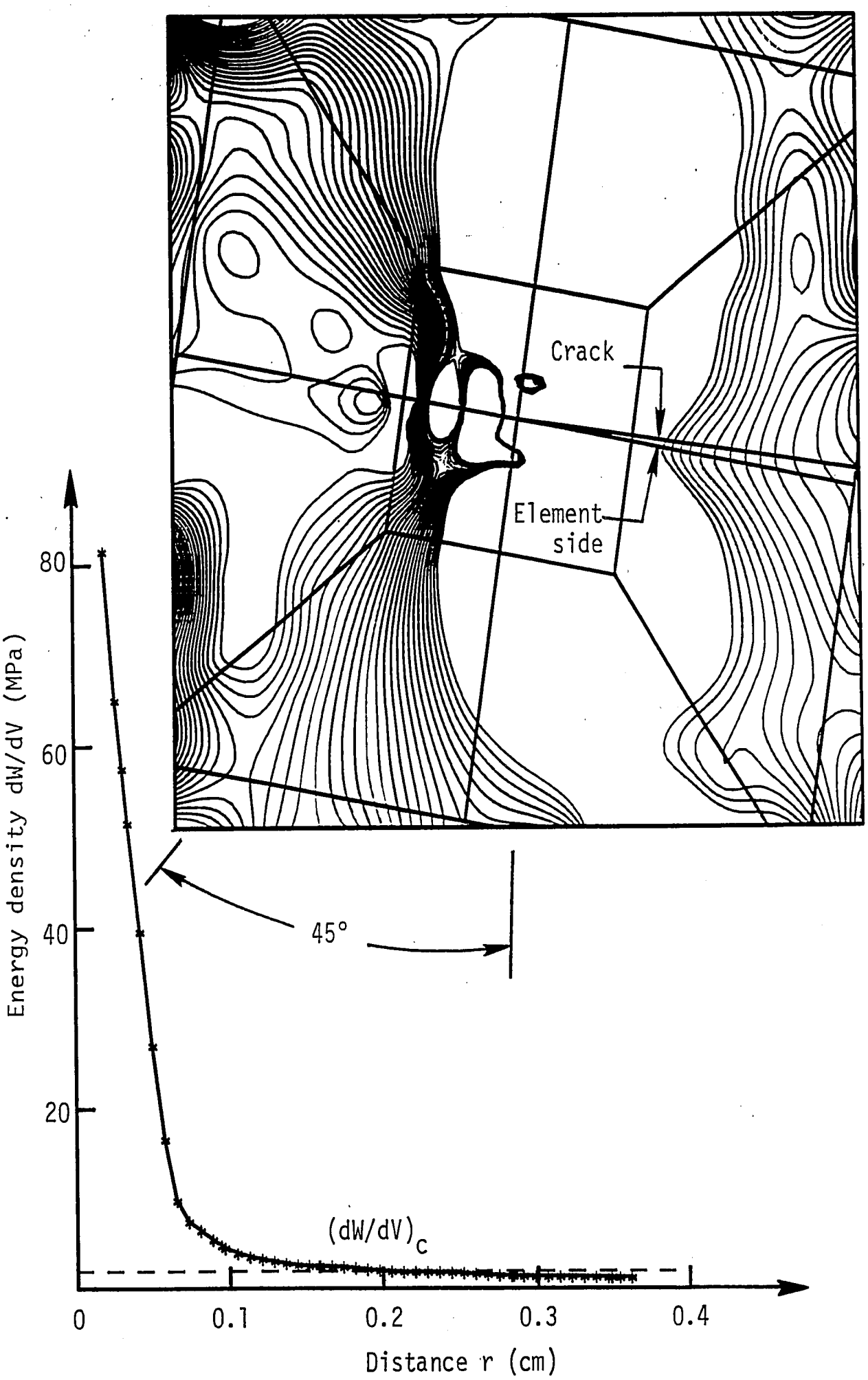

Figure 8.16. Variations of energy density with distance for third step crack growth with $\beta = 45°$.

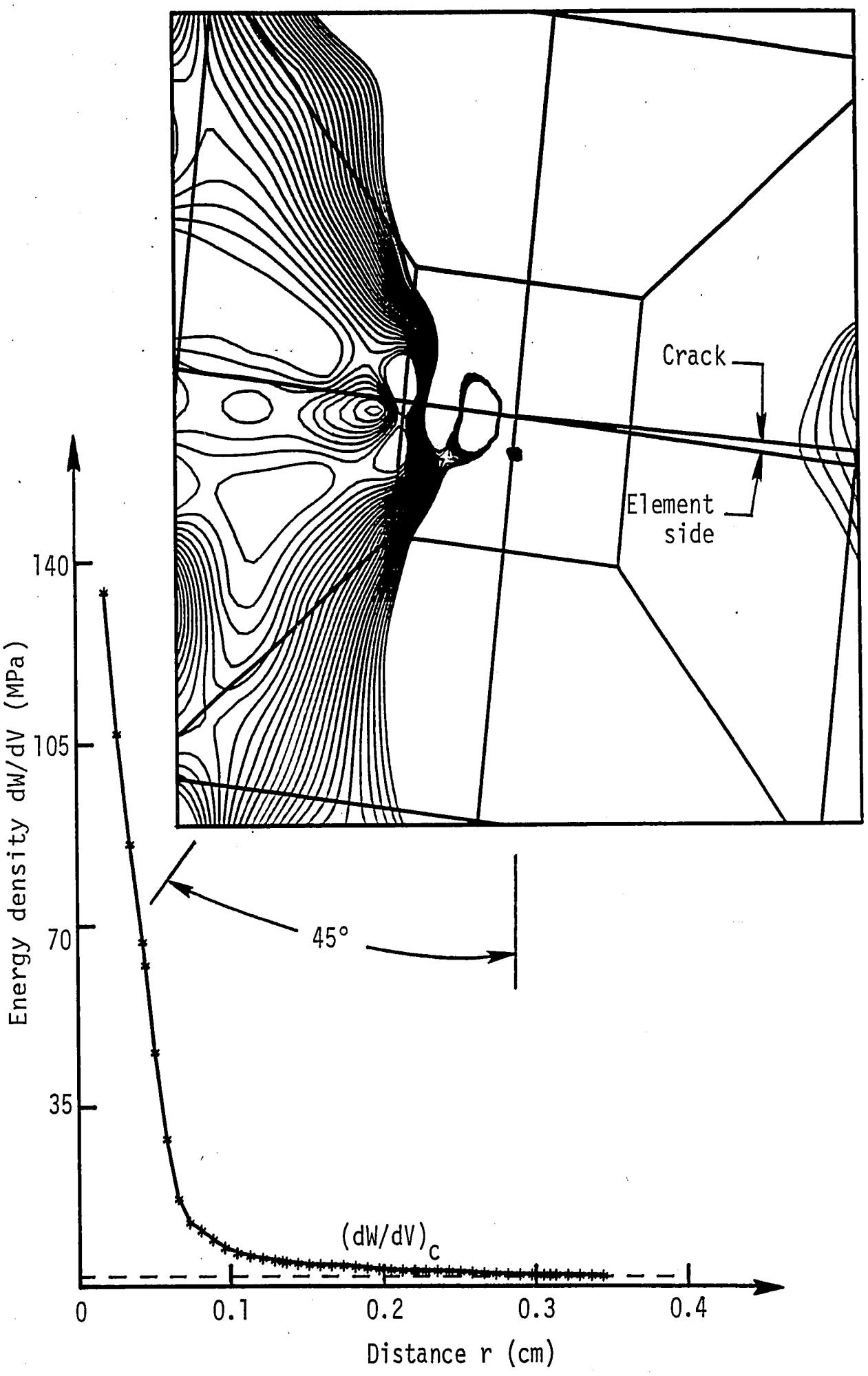

Figure 8.17. Variations of energy density with distance for fourth step crack growth with $\beta = 45°$.

8.4 Crack Angle $\beta = 60°$

As the crack angle β increases, the unbroken ligament size decreases accordingly. This increases the nominal stress as discussed earlier and each crack growth step. Only three steps are required to extend the crack to approximately the same distance from the plate edge, Figure 5.1(d). The contours of dW/dV and its variations with r along the prospective site of crack extension can be found in Figure 8.18. For $\beta = 60°$, it is found that $r_1^* = 0.551$ cm. Presented in Figures 8.19 and 8.20 are, respectively, the values of dW/dV for $r_2^* = 0.836$ cm and $r_3^* = 1.438$ cm.

8.5 Crack Angle $\beta = 75°$

Shown in Figure 8.21 are the constant dW/dV contours for $\beta = 75°$. The intersection of $(dW/dV)_c$ line with the dW/dV curve along the direction of $(dW/dV)_{min}$ gives the $r_1^* = 0.643$ cm. Remeshing of the finite element grid pattern to accommodate for the new crack tip position, a new set of data is obtained to find the second crack growth, $r_2^* = 0.973$ cm by using the values of dW/dV in Figure 8.22. The same applies to Figure 8.23 that yields $r_3^* = 1.986$ cm. The entire crack profile is given in Figure 5.1(e).

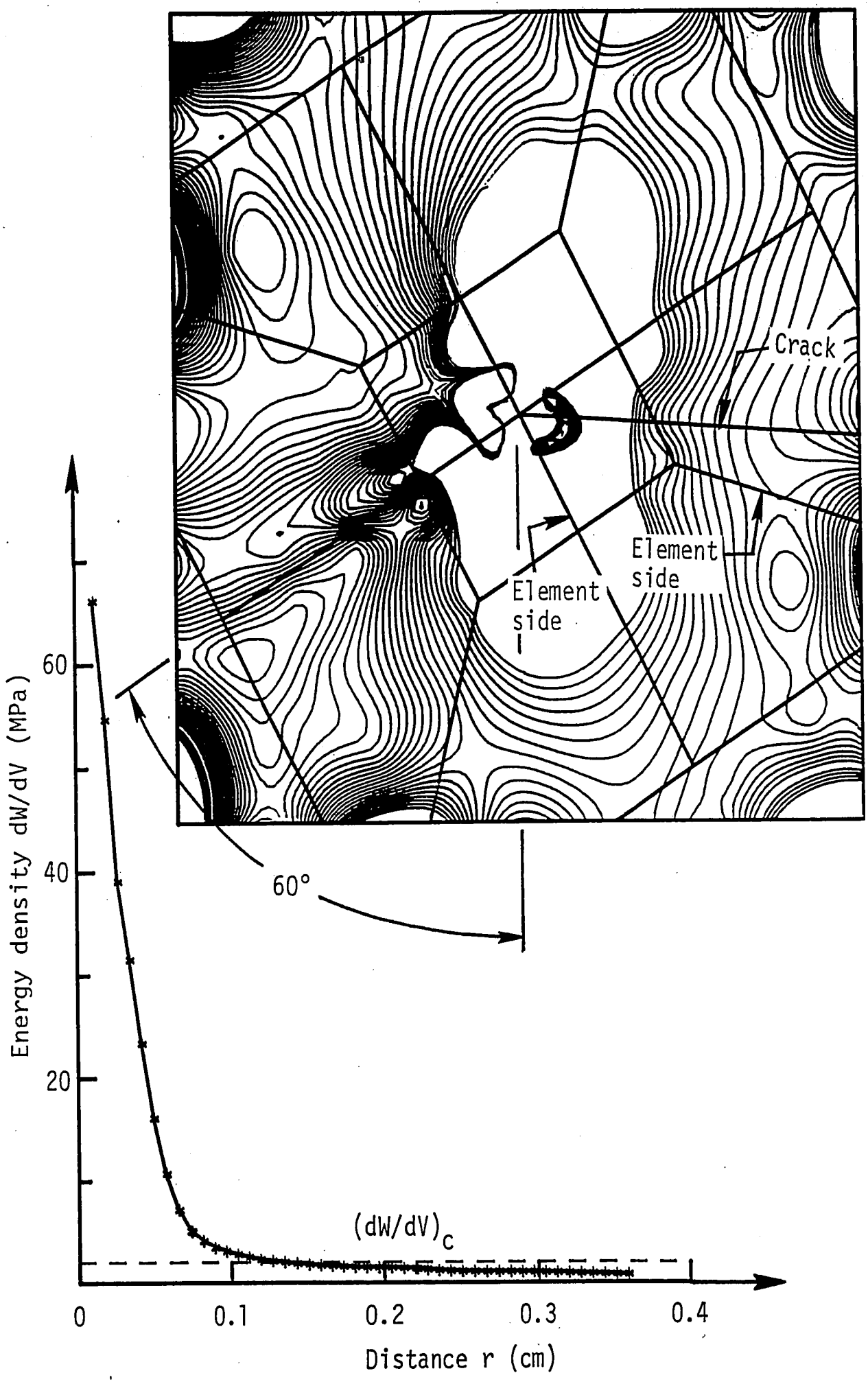

Figure 8.18. Variations of energy density with distance for first step crack growth with $\beta = 60°$.

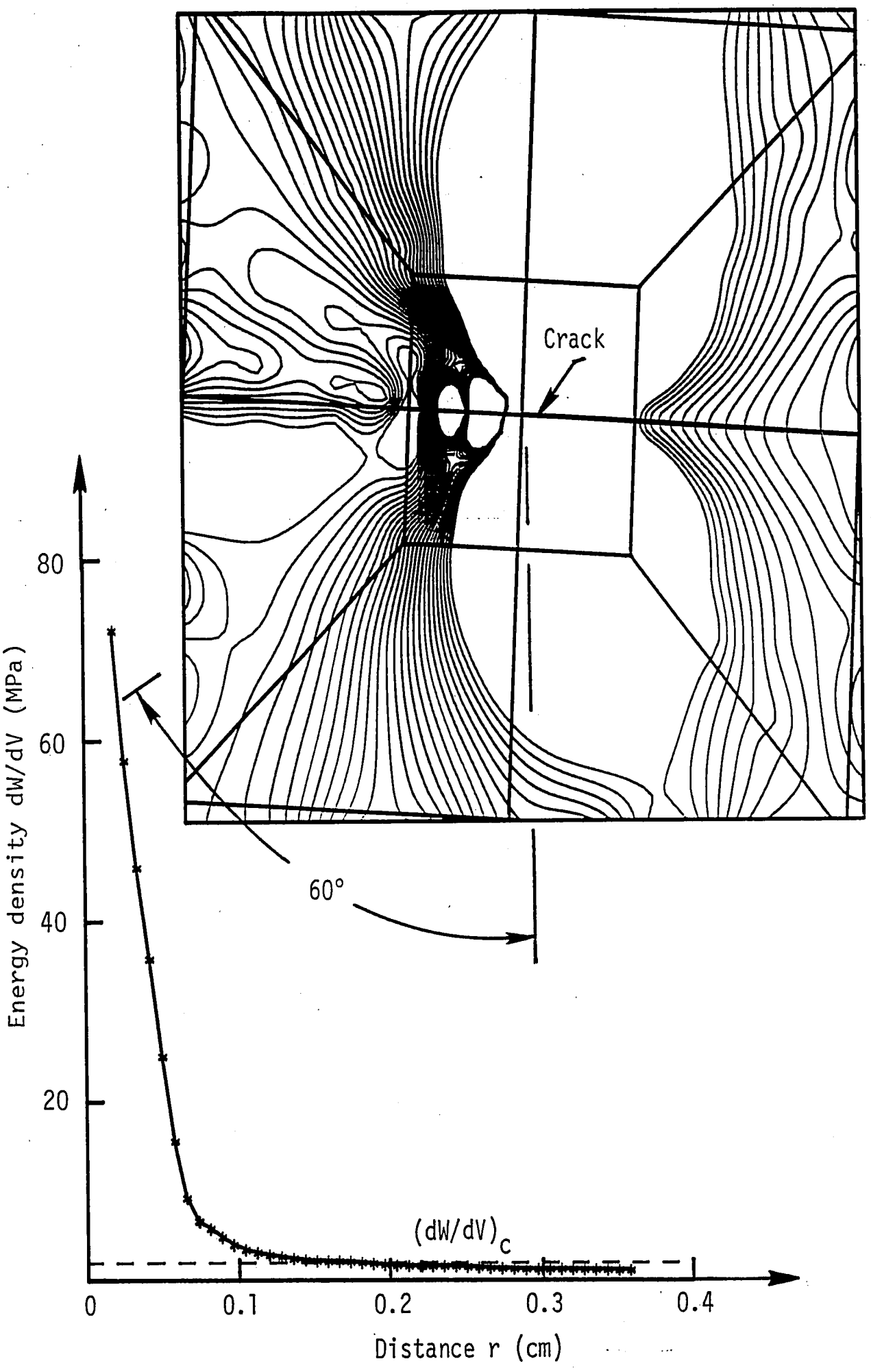

Figure 8.19. Variations of energy density with distance for second step crack growth with $\beta = 60°$.

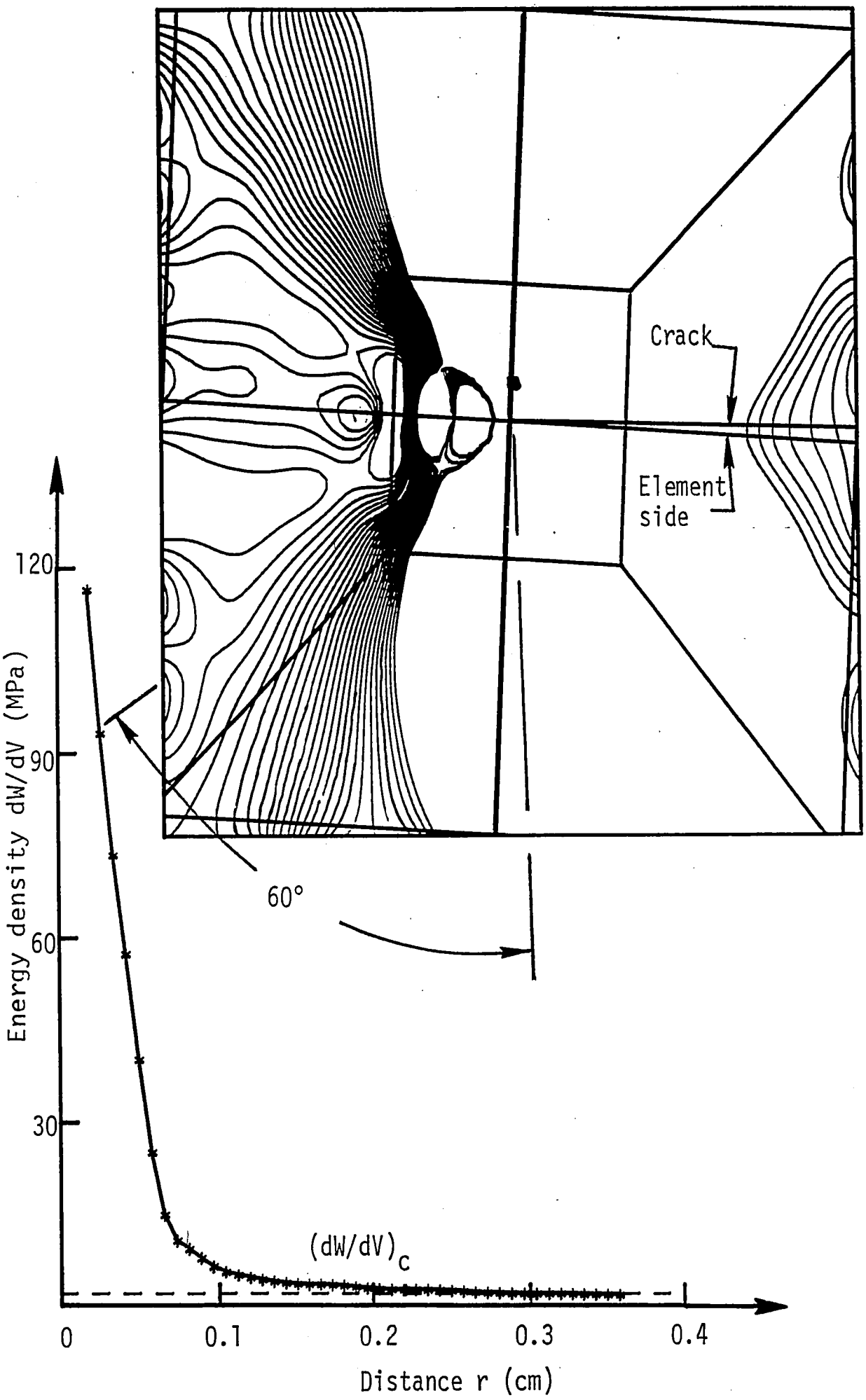

Figure 8.20. Variations of energy density with distance for third step crack growth with $\beta = 60°$.

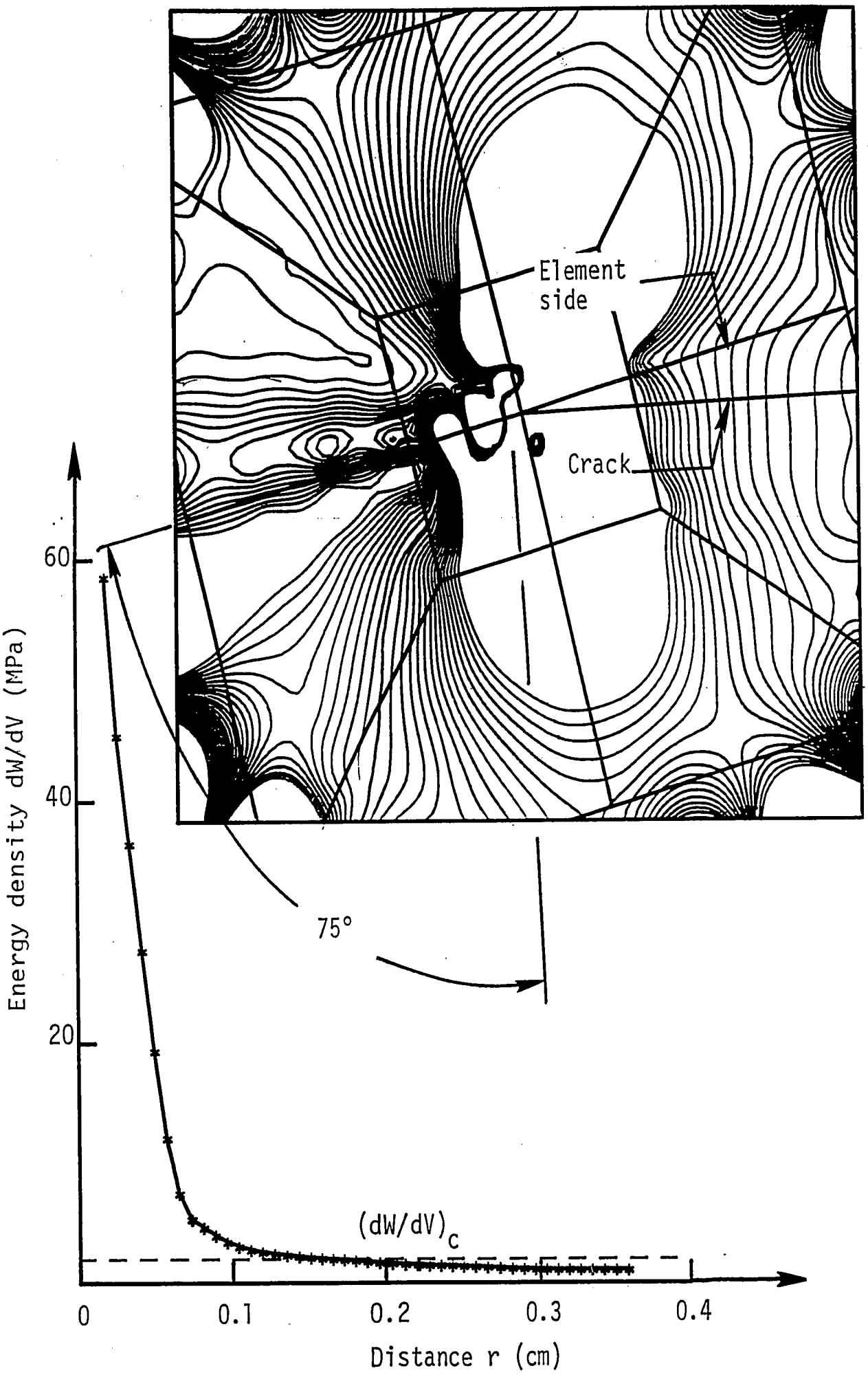

Figure 8.21. Variations of energy density with distance for first step crack growth with $\beta = 75°$.

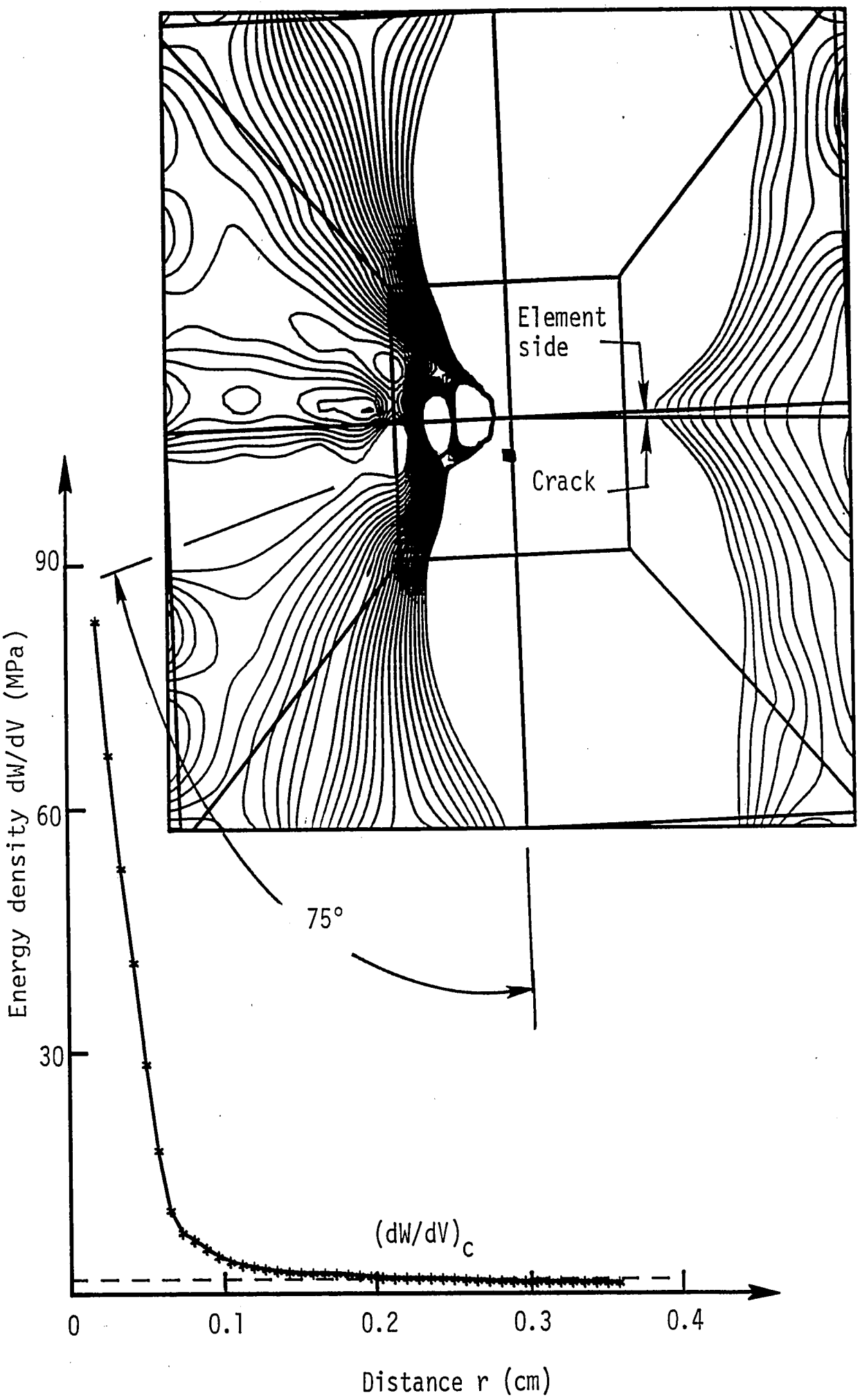

Figure 8.22. Variations of energy density with distance for second step crack growth with $\beta = 75°$.

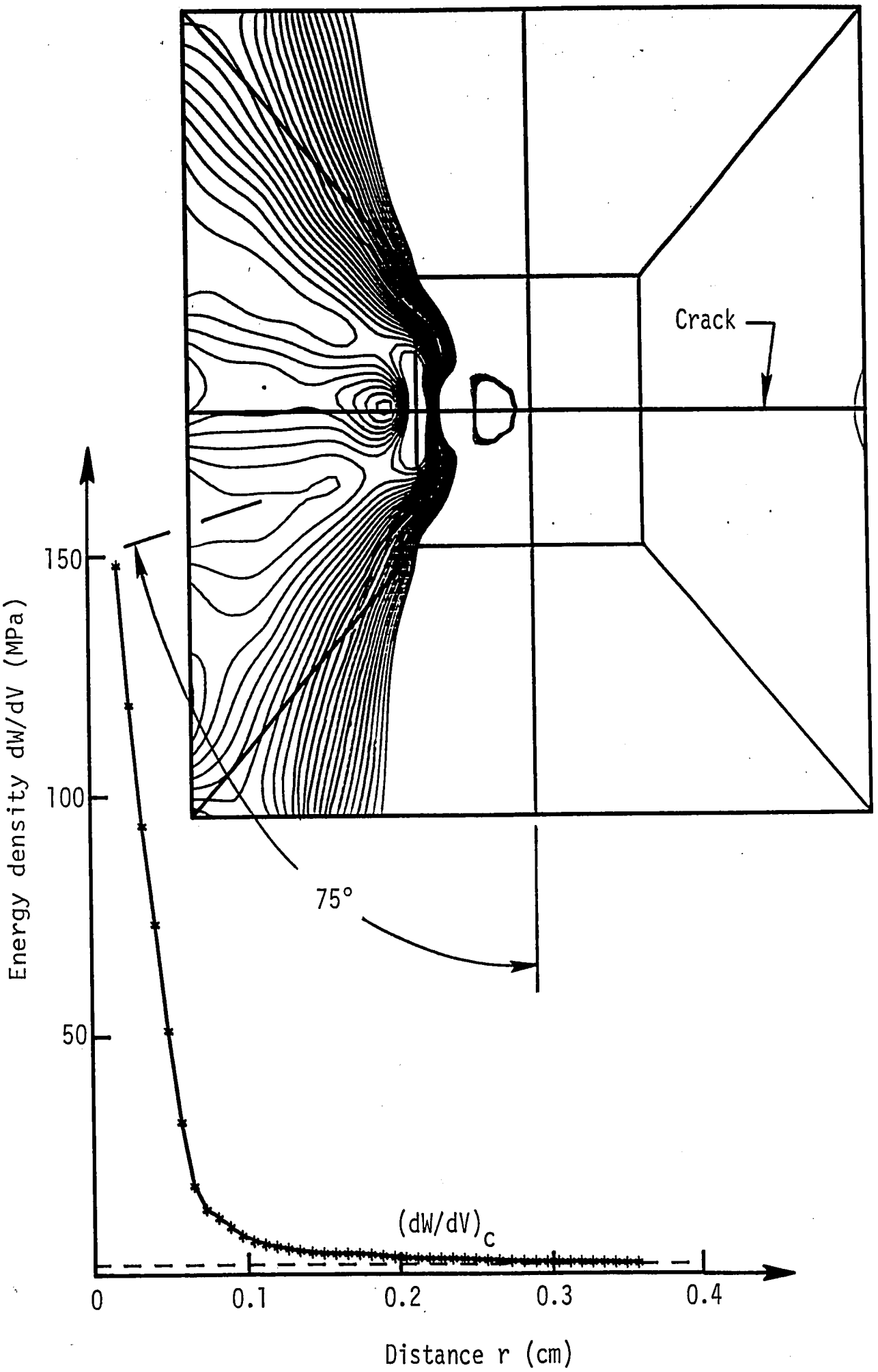

Figure 8.23. Variations of energy density with distance for third step crack growth with $\beta = 75°$.

IX. REFERENCES

[1] A. A. Griffith, "The Theory of Rupture", First Int. Congress for Appl. Mech., Delft, pp. 55-63, 1924.

[2] F. Erdogan and G. C. Sih, "On the Crack Extension in Plates under Plane Loading and Transverse Shear", Trans. ASME, J. Basic Engng., 85, pp. 519-527, 1963.

[3] K. J. Chang, "A Further Examination on the Application of the Strain Energy Density Theory to the Angled Crack Problem", Trans. ASME, J. Appl. Mech., 49, pp. 377-382, 1982.

[4] K. J. Chang and H.-C. Wu, "Angled Elliptic Notch Problem under Bi-axial Loading", Trans. ASME, J. Appl. Mech., 47, pp. 57-63, 1980.

[5] K. J. Chang, "On the Maximum Strain Criterion - A New Approach to the Angled Crack Problem", Engng. Fracture Mech., 14, pp. 107-124, 1981.

[6] K. J. Chang, "Further Studies of the Maximum Stress Criterion on the Angled Crack Problem", Engng. Fracture Mech., 14, pp. 125-142, 1981.

[7] S. K. Maiti and R. A. Smith, "Criteria for Brittle Fracture in Bi-axial Tension", Engng. Fracture Mech., 19, pp. 793-804, 1984.

[8] S. K. Maiti and R. A. Smith, "Criteria for Mixed Mode Brittle Fracture Based on the Preinstability Stress-Strain Field - I and II", Int. J. Fracture, 23, pp. 281-295, 1983.

[9] S. K. Maiti and R. A. Smith, "Theoretical and Experimental Studies on the Extension of Cracks Subjected to Concentrated Loading Near their Faces to Compare the Criteria for Mixed Mode Brittle Fracture", J. Mech. Phys. Solids, 31, pp. 389-403, 1983.

[10] S. K. Maiti, "Prediction of the Path of Unstable Extension of Internal and Edge Cracks", J. Strain Anal., 15, pp. 183-194, 1980.

[11] S. K. Maiti and K. S. R. K. Prasad, "A Study on the Theories of Unstable Crack Extensions for the Prediction of Crack Trajectories", Int. J. Solids Structures, 16, pp. 563-574, 1980.

[12] S. K. Maiti and R. A. Smith, "Prediction of Direction of Initial Crack Extension in a DCB Specimen", Int. J. Fracture, 23, pp. R41-R44, 1983.

[13] G. C. Sih, "Strain Energy Density Factor Applied to Mixed Mode Crack Problems", Institute of Fracture and Solid Mechanics, Technical Report, Lehigh University, 1972.

[14] J. L. Swedlow, "Criteria for Growth of the Angled Crack", in Cracks and Fracture, ASTM STP 601, pp. 506-521, 1976.

[15] I. Finnie and H. O. Weiss, "Some Observations on Sih's Strain Energy Density Approach for Fracture Prediction", Int. J. Fracture, 10, pp. 136-138, 1974.

[16] S. K. Maiti and R. A. Smith, "Criteria for Brittle Fracture in Biaxial Tension", Engng. Fracture Mech., 21, pp. 793-804, 1984.

[17] M. E. Kipp and G. C. Sih, "The Strain Energy Density Failure Criterion Applied to Notched Elastic Solids", Int. J. Solids Structures, 11, pp. 153-173, 1975.

[18] G. C. Sih, "Reply to Discussion on some Observations on Sih's Strain Energy Density Approach for Fracture Prediction by I. Finnie and H. O. Weiss", Int. J. Fracture, 10, pp. 279-283, 1974.

[19] G. C. Sih and D. Y. Tzou, "Discussion on Criterion for Brittle Fracture in Biaxial Tension by S. K. Maiti and R. A. Smith", Engng. Fracture Mech., 21, pp. 977-981, 1985.

[20] S. K. Maiti and R. A. Smith, "Closure on the Discussion by G. C. Sih and D. Y. Tzou on Criterion for Brittle Fracture in Biaxial Tension", Engng. Fracture Mech., 30, pp. 729-731, 1988.

[21] P. S. Theocaris and N. P. Andrianopoulos, "A Modified Strain Energy Density Criterion Applied to Crack Propagation", J. Appl. Mech., 49, pp. 678-679, 1982.

[22] P. S. Theocaris and N. P. Andrianopoulos, "The Mises Elastic-Plastic Boundary as the Core Region in Fracture Criteria", Engng. Fracture Mech., 16, pp. 425-432, 1982.

[23] G. C. Sih and E. E. Gdoutos, "Discussion on a Modified Strain-Energy Density Criterion Applied to Crack Propagation by P. S. Theocaris and N. P. Andrianopoulos", J. Appl. Mech., 49, pp. 678-679, 1982.

[24] G. C. Sih, E. T. Moyer, Jr. and E. E. Gdoutos, "Discussion on the Mises Elastic-Plastic Boundary as the Core Region in Fracture Criteria by P. S. Theocaris and N. P. Andrianopoulos", Engng. Fracture Mech., 18, pp. 731-734, 1983.

[25] C. P. Spyropoulos, "Some Remarks on the Det.-Criterion and Caustics", Engng. Fracture Mech., (forthcoming), 1992.

[26] G. C. Sih, "Thermomechanics of Solids: Nonequilibrium and Irreversibility", J. of Theoretical and Applied Fracture Mechanics, 9, 3, pp. 175-198, 1988.

[27] G. C. Sih, Mechanics of Fracture Initiation and Propagation, Kluwer Academic Publishers, The Netherlands, 1991.

[28] R. S. Barsoum, "On the Use of Isoparametric Finite Elements in Linear Fracture Mechanics", Int. J. for Numerical Methods in Engineering, 10, pp. 25-37, 1976.

[29] S. L. Pu, M. A. Hussain and W. E. Lorenson, "The Collapsed Cubic Isoparametric Element as a Singular Element for Crack Problems", Int. J. for Numerical Methods in Engineering, 12, pp. 1727-1742, 1978.

[30] G. C. Sih and R. C. Chu, "Characterization of Material Inhomogeneity by Stationary Values of Strain Energy Density", J. of Theoretical and Applied Fracture Mechanics, 5, 3, pp. 151-161, 1986.

[31] G. C. Sih and C. H. Chue, "Stability and Integrity of Mechanical Joints in Flight Vehicles", J. of Theoretical and Applied Fracture Mechanics, 10, 2, pp. 135-149, 1988.

[32] A. Carpinteri and G. C. Sih, "Damage Accumulation and Crack Growth in Bi-Linear Materials with Softening: Application of Strain Energy Density Theory", J. of Theoretical and Applied Fracture Mechanics, 1, 2, pp. 145-159, 1984.

[33] G. C. Sih, "Fracture Mechanics of Engineering Structural Components", Fracture Mechanics Technology, edited by G. C. Sih and L. Faria, Martinus Nijhoff Publishers, The Netherlands, pp. 35-101, 1984.

[34] G. C. Sih and B. Macdonald, "Fracture Mechanics Applied to Engineering Problems, Strain Energy Density Fracture Criterion", Engng. Fracture Mech., 6, pp. 361-386, 1974.

[35] G. C. Sih and H. Liebowitz, "Mathematical Theories of Brittle Fracture", Vol. 2 Fracture, edited by H. Liebowitz, Academic Press, Inc., New York, pp. 67-190, 1968.

[36] Engineered Materials Handbook Vol. 2, Engineering Plastics, ASM International, 1982.

[37] L. N. Gifford, Jr., "APES-Second Generation Two-Dimensional Fracture Mechanics and Stress Analysis by Finite Elements", David W. Taylor Naval Ship Research and Development Center, Bethesda, Maryland, December 1975.

[38] Surfer and Grapher Reference Manuals, Golden Software, Inc., Golden, Colorado, 1989.

[39] E. Hinton and D. R. J. Owen, Finite Element Programming, Academic Press, London, 1977.

[40] O. C. Zienkiewicz, The Finite Element Method, McGraw-Hill, London, 1977.

VITA

Eric Baisch was born on January 15, 1968 in Corning, New York to Eugene and Judy Baisch. He moved to Millville, New Jersey in the Spring of 1977 where he graduated from Millville Senior High School in June of 1986. In the Fall of 1986, Eric attended Lehigh University where he received his Bachelor of Science Degree in Mechanical Engineering in June of 1990. Supported by a Baldwin Graduate Fellowship, he began work on his Master of Science Degree at Lehigh. In the 1991 Fall Semester, he is completing his degree requirements while being supported by a Teaching Assistantship.